

University of Liège
Department of Aerospace & Mechanical Engineering
Computational & Multiscale Mechanics of Materials



Stochastic multiscale modeling of MEMS stiction failure

by

Truong Vinh HOANG

Submitted in fulfillment of the requirements for the degree of
Doctor in Engineering Sciences

June 2017

Members of the Examination Committee

Prof. Jean-Claude GOLINVAL (President of the Committee)
University of Liège (Liège, Belgium)
Email: jc.golINVAL@ulg.ac.be

Prof. Ludovic NOELS (Advisor)
University of Liège (Liège, Belgium)
Email: l.noels@ulg.ac.be

Prof. Alberto Corigliano
Politecnico di Milano (Milano, Italy)

Dr. Véronique Rochus
IMEC (Leuven, Belgium)

Prof. Maarten ARNST
University of Liège (Liège, Belgium)

Dr. Ling WU (guest Professor at Vrije Universiteit Brussel (VUB), Brussels,
Belgium)
University of Liège (Liège, Belgium)

Acknowledgments

First, I would like to thank Professors Jean-Claude Golinval, Alberto Corigliano, Véronique Rochus, Maarten Arnst, Ling Wu, and Ludovic Noels, who accepted to participate in the examination committee of this doctoral thesis.

I would like to thank the “Fond de la Recherche Scientifique de Belgique” (FRS-FNRS) for providing the funding for this work. The research has been partial funded by the Walloon Region under the agreement no 1117477 (CT-INT 2011-11-14) in the context of the ERA-NET MNT framework. Computational resources have been provided by the supercomputing facilities of the Consortium des “Équipements de Calcul Intensif en Fédération Wallonie Bruxelles” (CÉCI) funded by the Fond de la Recherche Scientifique de Belgique (FRS-FNRS).

I want to thank all the members of the 3SMVIB project, in particular, Professors Marius Pustan and Corina Barleanu, for their warm welcome during my visit.

I would like to thank Professors Maarten Arnst, Ling Wu, and Jean-Claude Golinval, for their appreciated advice. I also would like to thank Dr. Vincent Lucas and Professor Maarten Arnst for the encouragement they gave me in sports. A special thank goes to my advisor, Professor Ludovic Noels, for all the guidance, encouragement, and advice he has provided throughout the development of this thesis. He has been always available and patient with all my questions and troubles.

I wish also to thank my friends for their help. Finally, my thoughts go to my parents and my sister who supported me all these years. I must express my gratitude to Thien-Anh, my wife, who patiently encouraged me to keep moving forward.

Contents

Acknowledgments	3
Abstract	7
Abbreviations	9
1 Introduction	11
1.1 Motivation	11
1.2 State of the art	12
1.3 The developed methodology	18
1.4 Thesis structure	22
1.5 Contributions	23
2 Randomness in contacting surfaces	25
2.1 Introduction	25
2.2 Characterization of contacting surfaces randomness	27
2.3 Surface generators	32
2.4 Applications	35
2.5 Conclusion	49
3 Semi-analytical contact model for rough surfaces interactions	51
3.1 Introduction	51
3.2 Physics of adhesive forces	54
3.3 Evaluation of the asperity adhesive contact forces	57
3.4 Semi-analytical model for rough surfaces contact	61
3.5 Applications	64
3.6 Conclusion	67
4 Probabilistic representation of the random apparent adhesive contact forces	73
4.1 Introduction	73
4.2 Parametrization of the apparent adhesive contact forces	74
4.3 Stochastic model of the random apparent adhesive contact forces based on the gPCE	76

4.4	Applications	82
4.5	Conclusion	86
5	Uncertainty quantification of microstructures subjected to adhesive contact	91
5.1	Introduction	91
5.2	Stochastic multiscale scheme for adhesive contact problems	93
5.3	Verification of the stochastic model-based multiscale method	98
5.4	Validation with experimental results and discussion of physical aspects	105
5.5	Conclusion	113
6	General conclusions and perspectives	115
A	Appendices to Chapter 2	119
A.1	Probability measure space and random variable	119
A.2	Dealing with the different sizes of generated and measured surfaces	119
B	Appendices to Chapter 3	123
B.1	Analytical asperity contact models	123
B.2	Identification and spherical fitting of the contacting asperities	126
B.3	Verification of the negligibility of plastic deformation	129
C	Appendices to Chapter 4	133
C.1	Legendre polynomials	133
C.2	Multivariate kernel density estimation	134
D	Appendices to Chapter 5	137
D.1	Euler-Bernoulli beam theory and its 1D FE model	137
D.2	Deterministic analysis of adhered cantilever beam	139
	Bibliography	143

Abstract

In the context of microelectromechanical systems, due to their reduced size, the surface phenomena, e.g. adhesion contact, play an important role in the reliability of the devices. Indeed, the adhesive forces, e.g. capillary and van der Waal forces, can lead to the stiction failure for which the two contacting surfaces can accidentally be stuck together permanently. This is a common failure of MEMS. Because of the comparability between the roughness of the contacting surfaces and the ranges of adhesive stress, the interaction area can be much smaller than the apparent one. Since the contact zone is reduced and becomes comparable with the characteristic length scale of the surface roughness, the behaviors of micro structures subjected to adhesion suffer from a scatter, i.e. while some devices are unstuck, the others with an identical design are stuck. The objective of this work is to predict in a probabilistic way the adhesion behaviors of MEMS by accounting for the randomness of the contacting surfaces.

The straightforward solution toward this end consists in constructing a numerical model, e.g. using finite element method, and in performing a Monte-Carlo simulation (MCS) directly on that model. Because the problem spans multiple scales, including the nanometers range of adhesive stress and the micrometers length scale of MEMS, that method demands a huge computational cost and becomes unpractical. In this work, a stochastic model-based multiscale method is developed to fulfill the predefined objective while remaining efficient in terms of computational cost. In this model, MCS is also performed, however, in a scale-by-scale way. With this method, the model is executed with acceptable computational cost. To verify the proposed model, a comparison in terms of the numerical predictions obtained from two approaches, direct MCS and stochastic model-based method, is performed. Furthermore, the model is applied to simulate the stiction tests reported in the literature, and also on the experimental surfaces fabricated by our partner at IMT-Bucharest lab ¹ (without stiction test). By comparing the numerical predictions with the experimental results, the model is then validated.

The model is used to broaden our knowledge in stiction phenomenon by considering the effects of the following aspects on the adhesion energies: the roughness of surfaces, the non-Gaussianity in the probability distribution of surface heights, and the humidity of the environment conditions. Furthermore, the comparison between different sources of uncertainty, e.g. due to the surfaces roughness and in the geometry dimensions of the devices, is performed.

¹Visit IMT lab at <http://www.imt.ro/>

Abbreviations

ACF	autocovariance function
AFM	atomic-force microscopy
BGT	Bush-Gibson-Thomas
CDF	cumulative distribution function
DMT	Derjaguin-Muller-Toporov
FFT	fast Fourier transform
FE	finite element
(g)PCE	(generalized) polynomial chaos expansion
GW	Greenwood-Williamson
JKR	Johnson-Kendall-Roberts
LPCVD	low pressure chemical vapor deposition
MCS	Monte-Carlo simulation
MD	molecular dynamics
ME	maximum entropy
MEMS	microelectromechanical systems
MKDE	multivariate kernel density estimation
PCA	principal component analysis
PDF	probability density function
PSD	power spectral density
UQ	uncertainty quantification
vdW	van der Waals

Chapter 1

Introduction

1.1 Motivation

Nowadays, microelectromechanical systems (MEMS) are parts of a flourishing technology [36, 18, 81, 59, 137]. Due to their reduced size, on the one hand, MEMS devices hold appreciated advantages, such as low power requirement, and reduced manufacturing cost. MEMS devices, such as accelerometers, digital mirrors, pressure sensors, gyroscopes, resonators, and DNA chips, are successfully integrated in many domains ranging from industry to life sciences. In spite of those advantages, on the other hand, the technology is hampered by reliability issues. For example, due to their small size, MEMS devices are characterized by a large surface to volume ratio which combined to the relative smoothness of the surfaces, the small interracial gaps, and the small restoring forces, makes them vulnerable to surface forces. As a result, when two parts of a micro device contact each others, they can permanently adhere together because of the adhesive forces, such as van der Waals (vdW) and capillary forces. That phenomenon is called stiction – a common failure of MEMS, see Fig. 1.1 [135, 133, 136, 126, 14, 15, 87, 78, 65, 129]. To improve the reliability when developing a new MEMS device, the stiction phenomenon should be investigated during the design process.

As it was stated in [138], “*All surfaces are rough.*”. It turns out that the surface roughness plays an important role in tribology problems, particularly in the context of MEMS stiction. Indeed, because of the roughness of the contacting surfaces, see Fig. 1.2, and the relative short range of adhesive stress, the interaction between rough surfaces follows the multiple asperity contact theory, and the interacting area is usually much smaller than the apparent one [42, 138, 6, 102, 101, 79]. In addition, due to the short range of the adhesive interaction, the contact zone governing the phenomenon is limited in comparison with the size of the micro-structure, and consequently its size might not be fully separated, in the sense of the order of magnitude, with the characteristic length of the contacting rough surfaces, e.g. the distance between two contacting asperities. As a result, the behavior of micro-structures subjected to adhesion contact suffer from a scatter, as it was stated in [134] “... *why one MEMS device sticks and another ‘identical’*”

one does not.” Toward the end of predicting the stiction risk during the MEMS design, the uncertainties of adhesion behaviors should be quantified. Although there exist other sources of uncertainties in addition to the randomness of the contacting rough surfaces, e.g. material properties uncertainty, this work focuses on the surface roughness due to its importance on the stiction phenomenon.

To predict, in a probabilistic way, the stiction behavior, the brute force solution consists in using the probabilistic theory to characterize the sources of uncertainty, i.e. the randomness of rough surfaces, and in using Monte-Carlo simulation (MCS) to propagate the randomness through a model of the considered structure. Due to the multiple scales involved, i.e. the range of adhesive stress is $\mathcal{O}(1 \text{ nm})$ while the size of MEMS structures is $\mathcal{O}(100 \text{ }\mu\text{m})$, this method is characterized by an expensive computational cost which certainly limits its applicability.

The aim of this work is to breakthrough this limitation. A probabilistic multiscale model of the phenomenon is constructed. The randomness of the contacting rough surfaces is propagated through this model, however, in a scale-by-scale way instead of a direct one, which makes the stiction phenomenon predictable, in a probabilistic way, with acceptable computational cost.

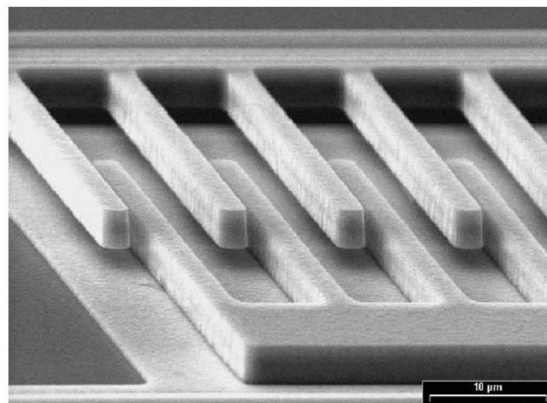


Figure 1.1: Scanning electron microscope picture of the stiction failure of a comb drive reported in [133].

1.2 State of the art

In this section, the aspects related to the objective of this work including stiction experiments, contact mechanics, and uncertainty quantification of multiscale problems are put in the context of the state of the art.

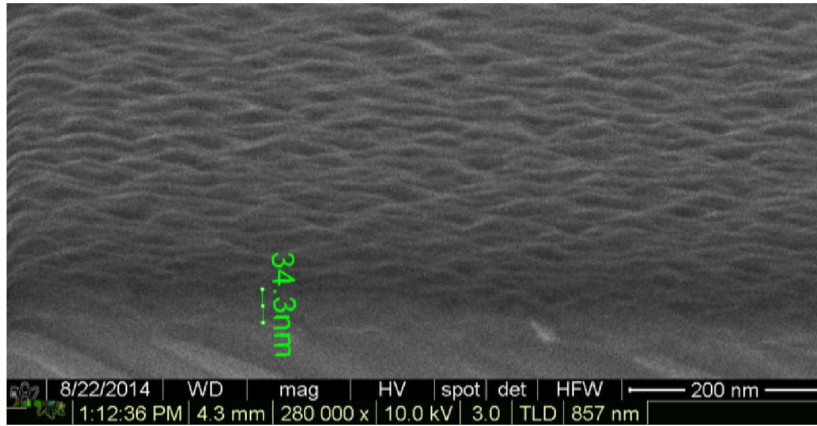


Figure 1.2: Scanning electro microscope picture of a polysilicon surface fabricated at IMT-Bucharest lab.

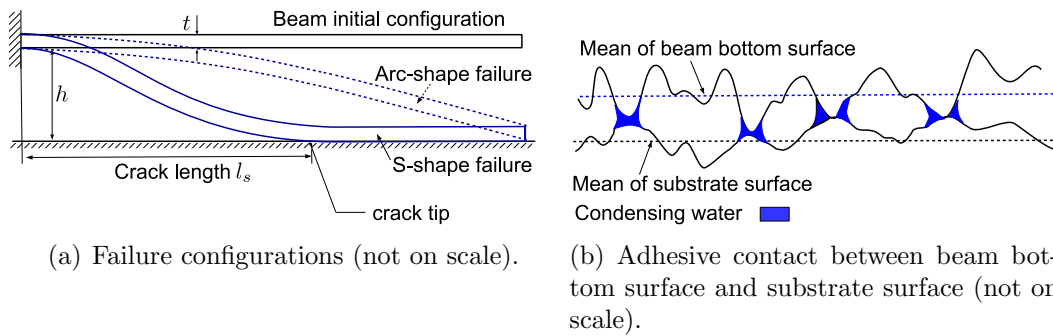


Figure 1.3: The stiction failure of a cantilever beam structure under humid condition: (a) released configuration and two possible failure configurations, S-shape and arc-shape, with crack length l_s identified for the case of S-shape failure, (b) zoom into a part of the contact zone, which spreads from the crack tip to the beam free end, with illustration of the condensing water area on the surface topology.

1.2.1 Stiction experiments

Many experiments were conducted to investigate the stiction phenomenon. For instance, in [151, 29, 109, 32, 31, 120, 121, 65], the stiction tests were implemented using micro cantilever beam structures. The beams were first artificially forced to enter into contact with the substrates. The external factors were then released and the stiction configurations were obtained, see Fig. 1.3(a). Using the interferometer, the crack lengths – the length of non-contact zone, see Fig. 1.3(a) – were measured and used to evaluate the apparent adhesion energies. The experimental results showed that the apparent adhesion energies between rough surfaces are smaller than the theoretical ones by ratios in the range $10^{-6} - 1$. This range is also an approximation of the ratio between the interacting area – the area on which the adhesive stress is applied, e.g. the condensing water area

in case of capillary interactions – and the apparent one, see Fig. 1.3(b). These experimental results confirm the multiple asperity contact theory, i.e. due to the roughness of the contacting surfaces the contact interaction involves only the highest asperities of the surface topology and the real interacting area is much smaller than the apparent one as illustrated in Fig. 1.3(b) [47]. Considering the rough surface as an ergodic random field for which a probability density function of surface heights is derived, the multiple asperity contact theory implies that the shape of the probability density function affects the contact interaction. When dealing with adhesive contact problems, a Gaussian probability distribution of surface heights is usually assumed. However, since the Gaussian distribution is based on only two parameters, the mean and the variance, it cannot approximate accurately the probability distribution of surface heights especially when getting further from the mean value [24,156]. Moreover, the effective contact zone governing the phenomenon is limited in size compared to the size of the involved micro-structures. For example, in the case of the S-shape failure of the micro beams illustrated in Fig. 1.3(a), although the apparent contact zone is large and spreads from the crack tip – defined as the separation point between non-contact and contact zones – to the beam end, the effective contact zone on which the adhesive forces act to induce the S-shape is only located around the crack tip [29]. As a result, the contacting length scale might not be fully separated, in the sense of the order of magnitude, with the correlation length of the contacting surfaces – the distance at which the value of autocovariance function (ACF) of surface heights is negligible compared to the surface height variance. Since the ratio between the interacting area and the apparent one is generally much smaller than the unit, the behavior of micro-structures subjected to adhesive contact can suffer from scatters. In [151,32], the uncertainties of the apparent adhesion energies were experimentally observed confirming the existence of this phenomenon. Indeed, the standard deviations of the apparent adhesion energies were observed to be up to 50% of the mean values [151,32].

1.2.2 Adhesive contact models

Prediction of the stiction risk relies on the contact mechanics. The domain is developed based on the Hertz contact model [48] which originally deals with the non-adhesive elastic contact between spherical bodies. For the problems of adhesive contact between spheres, there exist three analytical models: the Derjaguin-Muller-Toporov (DMT) model [33], the Johnson-Kendall-Roberts (JKR) model [57], and the Maugis model [90]. While DMT model is applicable for hard contacting bodies and long range adhesive stress, the JKR model is used for soft contacting bodies and short range adhesive stress. Maugis model is the transition solution between them.

Based on the multiple asperity contact theory in which the interaction involves only the highest asperities, statistical approaches of rough surfaces contact models, such as Greenwood and Williamson (GW) model [42] or Bush-Gibson-Thomas (BGT) model [20], were developed. In these models, the rough surface is assumed to be a Gaussian random field for which the distribution of the summits, i.e. the distribution of their

heights and radii, is well-established using the statistical moments, such as the variances of surface heights, and the variances of the first and second order spatial derivatives of surface heights. For GW model, the summit radii are approximated by their mean value while for the BGT this approximation is relaxed. The contact forces are evaluated by applying the appropriate spherical contact model on the summits using their heights and radii as input data. The contact forces between rough surfaces are then calculated by an integration of the asperity contact forces weighted with the distribution function of summits. One disadvantage of these models is the local property of summits, i.e. the summit radii are calculated using the spatial derivatives which are evaluated depending on the sampling distance. Furthermore, in order to derive the analytical solution, the apparent contact area is assumed to be infinite. As a result, it is not applicable for a probabilistic analysis which requires to account for the size of the contacting surfaces. In addition, the assumption of a Gaussian probability distribution of the surface heights might not be accurate when predicting adhesion as shown in [24, 156].

More recently, full numerical models, e.g finite element (FE) [9, 8, 7, 100, 153, 143, 142, 141] or molecular dynamics (MD) [74, 23, 106] models, were developed for contact problems. Although they bring accurate results and account for the size effect, they are not efficient in terms of computational cost. This fact is due to the relative small size of the discretized mesh required because of the short range of adhesive forces ($\mathcal{O}(1 \text{ nm})$) and of the small size of asperity radii ($\mathcal{O}(200 \text{ nm})$), compared to the size of the meshed contacting surface ($\mathcal{O}(10 \mu\text{m}^2)$).

When predicting the behaviors of MEMS structures subjected to adhesive contact, the inefficiency of these full numerical methods becomes problematic since the size of the apparent contact area increases. Therefore, it is more advantageous to apply the multiscale approach in which the meso-scale contact forces are derived using a model accounting for the adhesive interaction at the lower-scale of the adhesion phenomenon. The meso-scale adhesive forces are then integrated into the upper-scale model of the considered structure as adhesive contact laws. The behavior of the MEMS structures is then predicted effectively using the FE method. This approach was developed in [146, 127], and particularly in the author's master thesis [50], however for deterministic problems only.

1.2.3 Uncertainty quantification of multiscale phenomenon

In practice, because of the randomness in the physical aspects, such as material microstructures and rough contacting surfaces, the behaviors of the involved structures suffer from scatters. Indeed, due to these randomnesses, the problems properties such as material properties, contact behaviors, and boundaries conditions are nondeterministic. As a result, the behaviors of identical-design products might not be identical. This fact is particularly common in the context of MEMS and was considered in several studies related to the elastic behavior [85], stiction failure [151, 29], drop-induced failure [84, 83, 86], or again resonance frequencies of micro-beams [75, 76, 145].

The physical problems span on three different scales ¹.

- The lower-scale is related to the uncertainty sources, e.g. material grain structure, contacting rough surfaces.
- The meso-scale is related to the homogenized constitutive behaviors, such as elastic modulus and contact forces, evaluated on a meso-scale model, e.g. a meso-scale volume element.
- The upper-scale is related to the structural behaviors.

Let l^m , l^{meso} , l^M be the characteristic lengths at the lower-scale, the meso-scale, and the upper-scale respectively. The principle of separation of scales of a classical multiscale method is described as [38, 49, 75, 111]

$$l^m \ll l^{\text{meso}} \ll l^M. \quad (1.1)$$

The first condition, $l^m \ll l^{\text{meso}}$, implies the statistical representative of the homogenization, i.e. the meso-scale volume element is representative and the constitutive behaviors are deterministic. The second condition, $l^{\text{meso}} \ll l^M$, is the requirement of the applicability of the homogenized constitutive behaviors, i.e. the size of the problem on which homogenization is performed is much smaller than the upper-scale characteristic length on which upper-scale loads and boundary conditions vary in space. However, since l^M is reduced for MEMS, the scale separations stated in Eq. (1.1) might not hold simultaneously. Indeed, to keep $l^{\text{meso}} \ll l^M$, the condition $l^m \ll l^{\text{meso}}$ is no longer satisfied, i.e. $l^m \sim l^{\text{meso}}$. As a result, the meso-scale volume elements are stochastic and the constitutive behaviors are non-deterministic. Furthermore, it is often that there exist the local governing zones, which are identified depending on the physical problem, such as the plastic zone around the opening tip in fracture phenomenon, or the effective contact zone around the crack tip in the stiction phenomenon, see Fig. 1.3(a). Let l^{eff} be the characteristic length of that zone. l^{eff} is typically of the order of magnitude of the lower-scale, consequently $l^m \sim l^{\text{meso}} \sim l^{\text{eff}}$. That fact implies that there exist uncertainties not only in the meso-scale constitutive behaviors but also in the structural behaviors.

Quantifying the uncertainties at the upper-scale requires to characterize the randomness of the uncertainty sources and to propagate these randomnesses to the homogenized constitutive behaviors and then to the structural behaviors.

¹In a conventional multiscale method, there are three scales: micro-scale, meso-scale and macro-scale. In this work, because the considered MEMS devices are already of micro-scale size, to avoid misunderstandings, instead of using the two terms micro-scale and macro-scale, the two alternative terms lower-scale (for surface roughness) and upper-scale (or sometimes structural scale for MEMS structures) are used.

Characterization of the randomness at the lower-scale

The considered source of uncertainty in the particular context of contact problems is the contacting surface topology. The rough surfaces can be modeled using probability theory as a scalar-valued random field indexed in a 2D Euclid space [73, 68, 17]. To simulate this random field, the spectral representation method is widely used [3, 4]. The rough surface topology is statistically characterized by the probability density function and the spatial ACF of surface heights. These properties are evaluated based on surface measurements, which can be obtained accurately using Atomic-force microscopy (AFM) technique for MEMS. To generate the non-Gaussian surfaces, numerical surfaces can be generated following the method developed in [104, 152] in which the Gaussian surfaces are first generated and then mapped to the non-Gaussian ones. An alternative method to generate the non-Gaussian surfaces is to use the nonparametric probabilistic methods as developed in [116, 45, 117].

Stochastic multiscale approaches

When dealing with non-deterministic multiple scale problems, a straightforward solution is to perform a direct MCS on a multiscale model of the considered problem [86]. In this approach, the sources of uncertainties at the lower-scale are characterized and simulated as described above. To evaluate the upper-scale structural probabilistic behavior, the direct MCS has to solve the multiscale model for each generated sample of the lower-scale random sources. The disadvantage of the MCS is the slow convergence rate. The convergence rate can be accelerated using the sampling method such as important sampling, variance reduction, Latin hypercube [43, 71, 92]. Nevertheless, in our specific problem the MCS is performed on a multiscale model which requires a significant computational effort for each evaluation, because of the evaluation of the constitutive behaviors at the different integral points in the structure. These methods are thus inefficient.

To overcome this difficulty, the stochastic model-based multiscale framework in which the MCS is performed in a scale-by-scale way with two separated MCSs was developed. The first MCS is used to evaluate the samples of meso-scale constitutive behaviors. For example, the MC method was applied on meso-scale problems to evaluate the variations of elastic behaviors due to the grain structure of polysilicon film [85, 75, 76], to extract the stochastic properties of the parameters of meso-scale porous steel alloy material model [154], to evaluate open foams meso-scale properties [70], to extract probabilistic meso-scale cohesive law for polysilicon [93], to extract the effective properties of random two-phase composites [123], to study the scale dependency of homogenization for matrix-inclusion composites [130, 131], or again to consider the problem of composite materials under finite strains [77]. The second MCS can thus be conducted on the upper-scale model of the considered structures using the constitutive behaviors generated by a stochastic model constructed from the evaluated meso-scale behaviors. Such a framework has been developed to study the probabilistic structural behaviors

resulting from the randomness of material micro-structures, e.g. to study the product performance [155], and to evaluate the probability of the resonance frequencies of micro-beams [75, 76]. However, the method has never been applied before for the cases of random surface contact considered in this work.

One important component of this framework is the stochastic model representing the randomness of the meso-scale constitutive behaviors. The construction of that stochastic model is described in the following.

Construction of the generator of meso-scale behaviors

When performing MCS with a scale-by-scale approach, the meso-scale constitutive behaviors are parameterized and their parameters vectors are considered as either a vector-valued random field [25, 26], or a random vector when their spatial correlation is negligible. To deal with the random vector or vector-valued random field, the curse of dimensionality must be reduced. Therefore, before constructing the generator, a dimension reduction should be performed, e.g. using principal component analysis (PCA) on the covariance matrix for the case of random vector [53, 58, 37], or using Karhunen-Loève expansion on the ACF for the case of random field [61, 62, 72]. The reduced dimension random vector is then obtained, and a stochastic model is built to represent this random vector. A classical method for this task is to use a parametric multivariate distribution function, e.g. multivariate Gaussian distribution or maximum entropy (ME) solutions, to match the distribution moments such as means, covariance matrix and higher order moments. An alternative method which is more flexible for multidimensional cases is to use (generalized) polynomial chaos expansion (gPCE), see [139, 39, 149, 34], to construct a transformation from a chosen labeled distribution random vector, e.g. with multivariate Gaussian distribution or multivariate uniform distribution, to the studied random vector, i.e. the reduced dimension random vector.

1.3 The developed methodology

1.3.1 Overview

The objective of this work is to construct a numerical model to predict, with an acceptable computational cost, the probabilistic behavior of micro-structures subjected to adhesive contact between rough surfaces. The model involves three scales.

- The lower-scale is related to the randomness of contacting surfaces. The characteristic lengths at this scale, l^m , are the correlation length of the considered surfaces.
- The meso-scale is related to the adhesive contact behaviors evaluated between two rough surfaces. The characteristic length at this scale, l^{meso} , characterizes the size of these surfaces.

- The upper-scale is related to the structural behaviors of the considered micro structures. The characteristic length at this scale, l^M , is the size of these structures.

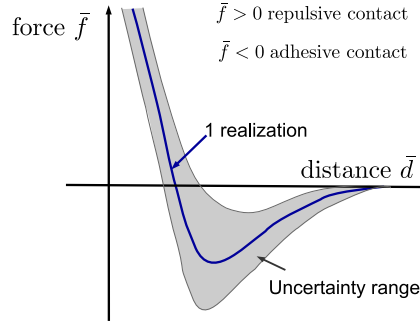


Figure 1.4: The random apparent contact forces between two rough surfaces.

As it is discussed in Sec. 1.2.3, in the context of MEMS, for $l^{\text{meso}} \ll l^M$ to hold, the length scale separation $l^{\text{meso}} \gg l^m$ is not ensured. As a result, when the contact area is much smaller than the apparent one by two or more orders of magnitudes, the apparent adhesive contact forces evaluated between meso-scale size surfaces still suffer from a scatter as illustrated in Fig. 1.4. Furthermore, due to the short range of adhesive stress (nanometers), the characteristic length l^{eff} of the effective contact zone, e.g. located around the crack tip in the case of beam failure see Fig. 1.3(a), is of the order of length scale l^m . Since the apparent adhesive contact forces are non-deterministic, and since $l^{\text{meso}} \sim l^{\text{eff}}$, the adhesion behaviors of MEMS suffers from scatters.

To obtain the probabilistic behaviors of the considered micro-structures, we apply the stochastic model-based method for which the MCS is implemented in a scale-by-scale way. This results in the stochastic model-based multiscale framework briefly described in the following items, see Fig. 1.5 for its illustration.

- (i) At the lower-scale, the randomness of the contacting rough surfaces is characterized and simulated using the spectral representation method. The topology of the contacting surfaces is measured using AFM technique. From these measurements, the probability density function of surface heights, the ACF, and the power spectral density (PSD) function – the density function of the surface heights variance in wave numbers – are evaluated. A surface generator is then developed using as input data the probability density function and the PSD function. As discussed in Sec. 1.2.1, the non-Gaussian characters of surface heights probability distribution must be accounted for to improve the accuracy when predicting stiction phenomenon.
- (ii) A meso-scale contact model is developed to evaluate the apparent adhesive contact forces between the meso-scale size generated random surfaces, see an illustration of these forces in Fig. 1.4. The model must account for the size of the generated surfaces and for the non-Gaussianity of surface heights probability distribution, while remaining efficient in terms of computational cost.

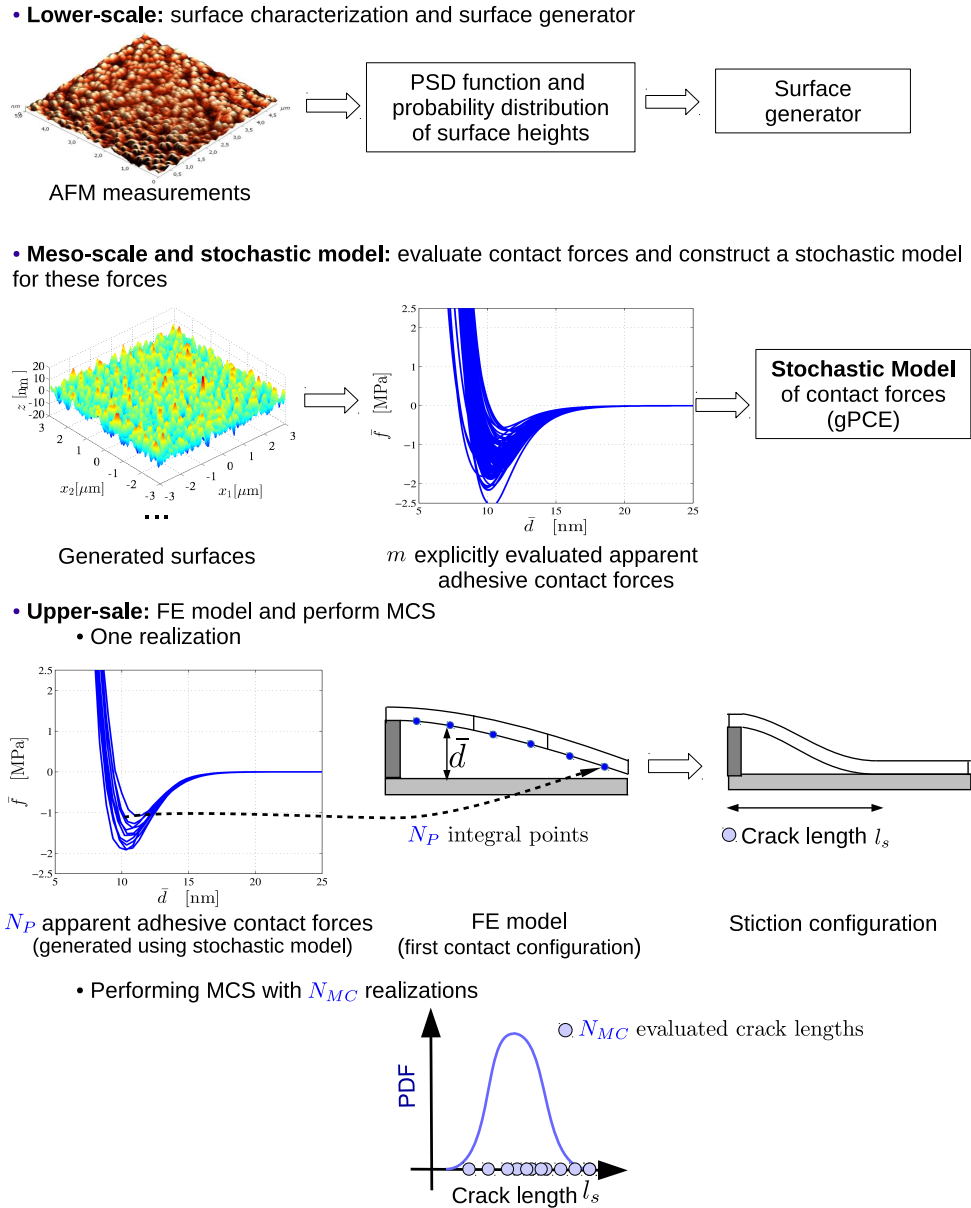


Figure 1.5: The stochastic model-based multiscale method applied for the evaluation of the probability density function (PDF) of crack lengths, see Fig. 1.1. For direct MCS, the stochastic model for apparent adhesive contact forces is excluded, and all the contact forces required to perform the MCS at the upper-scale are explicitly evaluated.

- (iii) The randomness of the meso-scale adhesive contact forces is effectively represented using a stochastic model which permits generating a large number of contact forces at a negligible computational cost while its construction requires only a relatively small number of the explicitly evaluated contact forces from step (ii). The stochas-

tic model is constructed based on the gPCE.

- (iv) At the upper-scale, a probabilistic FE model of the considered structure is developed. In that FE model, the meso-scale apparent adhesive contact forces, generated using the stochastic model in step (iii), are integrated as random contact laws. By performing MCS on that model, the probabilistic behaviors of the considered structure are evaluated.

Note that in a direct MCS, the step (iii) is excluded and all the required contact forces for step (iv) are explicitly evaluated from step (ii).

1.3.2 Features

The advantages of the proposed model are described in the following.

The semi-analytical contact model developed for rough surfaces in step (ii) is more advanced compared to the classical contact models e.g. the GW model. This model accounts for the non-Gaussian characters of the surface heights probability distribution as well as for the contacting surface size. In addition, it overcomes the disadvantages of assuming asperities as local summits, allowing to evaluate the asperity radius independently with the sampling interval.

The model has the ability to predict the uncertainty of stiction failure. By controlling the size of generated surfaces when evaluating the contact forces at step (ii), the size effect is involved leading to the randomness of the apparent contact forces, and therefore in the probabilistic behavior of the considered micro-structures.

The model is computationally efficient. To evaluate the structural probabilistic behaviors accounting for the randomness of contacting surfaces, instead of using direct MCS, i.e. all the samples of the random contact law required in step (iv) are explicitly evaluated from step (ii), the stochastic model developed in step (iii) is added to perform a scale-by-scale MCS which requires a lower computational cost. This fact is analytically proved in the following. Let m be the number of explicitly evaluated meso-scale adhesive contact forces required for the construction of the stochastic model in step (iii), N_{MC} be the number of MCS in step (iv), and N_P be the number of integral points of the structural FE model which is also the number of meso-scale contact forces required for each evaluation of the structural behavior. When performing direct MCS, the number of explicitly evaluated contact forces required is $N_{MC} \times N_P$. Because m and N_{MC} have the same numerical meaning, $m \sim N_{MC}$, and consequently $m \ll N_{MC} \times N_P$. In other words, the required number of explicitly evaluated contact forces is significantly reduced, typically by $N_p(m/N_{MC}) \sim N_P \sim \mathcal{O}(100)$ times, compared to the direct MCS. Furthermore, because the construction of the stochastic model in step (iii) is an additional step, it must be efficient. In this work, the stochastic model is developed using a truncated gPCE model for which the coefficients are effectively identified. With these achievements in computational efficiency, the proposed method becomes practical. We should keep in mind that the gain in the efficiency is obtained by the approximation

in terms of distribution when using the stochastic model to represent the randomness of the apparent adhesive contact forces.

The model is numerically verified and then validated with experimental results. As there exists an additional model in step (iii), to verify the stochastic model-based multiscale method, their results are compared with the direct MCS ones. In addition, the method is applied to model the stiction tests reported in [151] for its validation.

The model is used to broaden our understand of the stiction phenomenon. Using the proposed model, the evolution of the adhesion energies and their uncertainties in terms of the statistical characteristics of surface heights, e.g. variance, skewness, kurtosis, PSD function, and in terms of the environmental conditions, e.g. humidity level, is investigated. In addition, a comparison among different uncertainty sources, e.g. the random surfaces and the uncertain structural geometries is performed.

1.4 Thesis structure

The thesis is developed accordingly to the steps of the developed methodology, see Sec. 1.3, as follows.

Chapter 2, [Randomness in contacting surfaces](#), focuses on the characterization and simulation of contacting surfaces based on their AFM measurements. The randomness of the contacting surface heights is characterized by a non-Gaussian probability distribution and a PSD function. A surface generator is then developed in such a way that the heights of the generated surfaces match the probability density function and PSD function obtained from AFM measurements. The characterization and simulation processes are applied for two study cases: (i) two random surfaces of polysilicon substrates fabricated at IMT-Bucharest lab, and (ii) the (poly)silicon random surfaces involved in the stiction tests reported in [151]. For the second study case, since we do not have access to the AFM measurements, it is impossible to evaluate directly the PSD function. Instead we use a cut-off self-affine PSD formulation [80, 82] whose parameters are identified to ensure the following condition: the generated surfaces approximate well the available statistical quantities, such as the summits mean radius and the summits density, reported in [151].

Chapter 3, [Semi-analytical contact model for rough surfaces interactions](#), develops an adhesive contact model between rough surfaces. Motivated by the multiple asperity contact theory, a semi-analytical surface contact model is developed. The model is then applied to the experimental surfaces, investigated in Chapter 2, to evaluate the apparent adhesive contact forces in different environmental conditions controlled by the humidity level. Using the evaluated numerical results, we conduct an investigation of the effects resulting from the surface size and the non-Gaussian

characters of the surface heights probability distribution on the evaluated adhesive forces and on their observed uncertainties.

Chapter 4, [Probabilistic representation of the random apparent adhesive contact forces](#), describes the construction of the stochastic model of the random apparent adhesive contact forces. Because a sample of the apparent adhesive contact force is a force vs. distance function, see. Fig. 1.4, each contact force sample is parameterized and represented by a vector of parameters. Due to the randomness of the apparent adhesive contact forces, the parameters vector is considered as a random vector. A stochastic model is developed based on gPCE to represent the randomness of this random vector. Using this stochastic model to generate a set of the parameters vectors, one can obtain the set of corresponding apparent adhesive contact forces. The stochastic models are implemented for experimental surfaces whose contact forces are evaluated in Chapter 3.

Chapter 5, [Uncertainty quantification of microstructures subjected to adhesive contact](#), develops a FE model of micro-structure for which the apparent adhesive contact forces, generated using the stochastic model in Chapter 4, are integrated as the random contact laws. Applying a MCS on that model, the probabilistic behaviors of the considered structures are evaluated. In this chapter, the two approaches, the stochastic model-based approach and the direct MCS approach, are compared in terms of results and computational efficiency. After being verified, the stochastic model-based multiscale method is validated by comparing the numerical predictions and the experimental results reported in [151]. Using the numerical model, the stiction phenomenon is studied to point out the evolution of adhesion energies and their uncertainties in terms of the statistical parameters of the random surfaces and of the humidity level. Furthermore, the model is also extended to account for the uncertainties associated with the structural geometries for a study purpose. Although these geometrical uncertainties are simply modeled using the Gaussian distribution, this is a first step to construct an improved model which accounts for these uncertainties and for the randomness of contacting surfaces in an interactive way.

Chapter 6, [General conclusions and perspectives](#), concludes the dissertation and presents the perspectives.

1.5 Contributions

The contributions of this work are listed here below.

- (i) We have developed an original stochastic model-based multiscale methodology for adhesive contact problems of micro-structures in which the randomness of non-Gaussian contacting surfaces is characterized and propagated, in a efficient

way, to quantify the uncertainty of the involved structures. The model is verified with direct MCS and validated with the stiction tests reported in [151]. (Major contribution)

- (ii) We have developed a semi-analytical contact model to evaluate the adhesive contact forces between rough surfaces with a reduced computational cost compared to a FE model, while accounting for size effect and non-Gaussian probability distribution of surface heights, which are often neglected in an analytical model.
- (iii) We have constructed a framework to characterize and simulate the non-Gaussian random surfaces from their AFM measurements.

The outcomes of this work were published in the following papers.

Articles in peer reviewed journals

Hoang, T.V., Wu, L., Paquay, S., Golinval, J.-C., Arnst, M., & Noels, L. (2017). A computational stochastic multiscale methodology for MEMS structures involving adhesive contact. *Tribology International*, 110, 401-425.

Hoang, T.V., Wu, L., Paquay, S., Obreja, A. C., Voicu, R., Mller, R., Golinval, J.-C., & Noels, L. (2015). A probabilistic model for predicting the uncertainties of the humid stiction phenomenon on hard materials. *Journal of Computational & Applied Mathematics*, 289, 173 - 195.

Hoang, T.V., Wu, L., R., Golinval, J.-C., Arnst, M., & Noels, L. (2017). Stochastic multiscale model of MEMS stiction accounting for high order statistical moments of non-Gaussian contacting surfaces. *Journal of Microelectromechanical Systems*, in preparation.

Articles in conference proceedings

Hoang, T.V., Paquay, S., Golinval, J.-C., Wu, L., Arnst, M., & Noels, L. (2016). A Stochastic Multi-scale Model For Predicting MEMS Stiction Failure. *Proceedings of the SEM XIII International Congress and Exposition on Experimental and Applied Mechanics. (SEM XIII 2016)* (pp. 8).

Hoang, T.V., Wu, L., Paquay, S., Golinval, J.-C., Arnst, M., & Noels, L. (2016). A Study Of Dry Stiction Phenomenon In MEMS Using A Computational Stochastic Multi-scale Methodology. *EuroSimE 2016 in Montpellier* (pp. 4). IEEE.

Chapter 2

Randomness in contacting surfaces

2.1 Introduction

In practice, surfaces are rough. Indeed, the surface heights – the normal distances from the real surface to its reference mean surface assumed normally flat – are irregular, see Fig. 1.3(b). These irregularities are required to be characterized when analyzing tribology problems such as the adhesion contact in this work. Toward this end, one possibility is to use the Weierstrass-Mandelbrot function which was developed in the context of fractal theory [82,13]. Another possibility, which is more flexible, is to use the probability theory, in particular, the spectral representation method [3,119]. The latter approach gives a systematical way to evaluate the statistical properties of surface roughness from its measurements, and to construct a surface generator using these properties as input data. The two methods share one similar important characteristic, i.e. to model the surface roughness both methods use a summation of weighted sinus functions, whose wave numbers are sampled from a spectrum, and whose phases are randomly attributed. Owing to its flexibility, the spectral representation method is applied in this work and briefly described in the following in the context of adhesive contact.

The topology of a MEMS surface is accurately measured thanks to AFM technology. The statistical characteristics of surface heights including the probability density function and the ACF are then evaluated from these measurements. In addition to the ACF, the PSD function – the distribution density of the surface heights variance in wave numbers – is calculated using a Fourier analysis. The surfaces heights are usually assumed to follow a Gaussian distribution. The numerical surfaces are then generated by a summation of the random phases sinus functions whose weighted coefficients are derived from the PSD function. Although the spectral representation method was already developed, it was not used widely for the rough surface contact problems due to the significant requirement of the computational resources.

In the context of rough surface contact, the summits – the local maxima of surface topology – play an important role since only the highest ones are involved in the physical

contact interaction. For Gaussian surfaces, the statistical properties of summits are: (i) the mean radius of summits, the summits density, and the summits height variance that can be directly evaluated from the variance of surface heights and from the variances of the first and second order spatial derivatives of the surface heights; and (ii) these three variances corresponding to the zero, second, and fourth order moments of PSD function, m_{PSD}^0 , m_{PSD}^2 , and m_{PSD}^4 respectively. The proof of these properties can be found in [94]. The GW and the BGT contact models [42, 20], explained in more details in Chapter 3, were developed assuming a simple distribution of the summits heights and radii, and therefore, are widely used. Although these models are efficient in terms of computational cost, they have one significant drawback resulting from the local characteristic of the summits: the summit radius depends on the sampling interval of the measurement data. In other words, different sampling intervals result in different summits radii, and consequently, different contact forces predicted using either GW or BGT models as it is discussed in Chapter 3. Although these models are not applied in this work, the three interesting properties discussed previously will be exploited.

Using Gaussian distribution is not always an accurate approximation especially in the context of rough surface adhesive contact [24]. This fact will be proven in the next chapters. To account for the non-Gaussian characters of the surface heights probability distribution, the classical method is to apply a labeled distribution function, e.g. the beta or gamma distributions, or – more generally – the Pearson distributions family [99]. The coefficients of the chosen distribution function are then identified to match the moments, e.g. mean (usually assumed to be zero), root mean square roughness *rms*, skewness γ , and kurtosis β , which are directly evaluated from the AFM measurements. The disadvantage of this method is that there exist additional assumptions on the distribution functions, such as the finite supports of the beta distribution, which might be invalid. To avoid this problem, the ME method [54] is applied in this work. Without additional assumption, the distribution function is identified to ensure the maximization of its entropy and to match the moments obtained from AFM data.

Using the evaluated non-Gaussian probability density function and the PSD function, numerical surfaces can be generated following the method developed in [104, 152] in which the Gaussian surfaces are first generated and then mapped to the non-Gaussian ones. An alternative method for generating the non-Gaussian surfaces is to use the nonparametric probabilistic method developed in [116, 45, 117]. In this work, the first method is chosen because it is still applicable when a direct access to AFM data is not available.

The spectral representation method is developed through the characterization step described in Sec. 2.2, and the simulation step described in Sec 2.3. The method is then applied for two applications in Sec. 2.4: the experimental polysilicon surfaces fabricated at IMT-Bucharest lab, and the experimental (poly)silicon surfaces involved in the stiction tests reported in the reference [151]. For the surfaces reported in [151], we do not have access to AFM measurements but only to the statistical quantities, i.e. variance, skewness, and kurtosis of surface heights, and summits mean radius and summits

density. These information are enough to evaluate the surface heights probability distribution using the ME method. However, without access to AFM measurements, the PSD function cannot be evaluated using Fourier analysis. To overcome this difficulty, we use a self-affine cut-off formulation of PSD function [101, 80] and then identify its coefficients to satisfy the constraint that the generated surfaces approximate well the reported statistical quantities.

2.2 Characterization of contacting surfaces randomness

In this section, the characterization process used to evaluate the probability density function and the PSD function of the surface heights from the AFM measurements is described. The heights of a rough surface are modeled as a zero mean, second order, stationary, and ergodic random field, whose properties are discussed here after.

- With the second order assumption, the variance of surface heights is finite. In addition, we assume that the statistical moments upto the fourth order exist in order to account for non-Gaussian properties of surface heights.
- With the stationary assumption, the probability distribution of surface heights does not change with respect to a spatial shift.
- With the ergodicity assumption, the statistical properties of a random surface can be deduced from the measurements that have sufficiently large scan areas on that surface.

That field is denoted as $Z(\mathbf{x}, \theta)$, valued in \mathfrak{R} and indexed by $\mathbf{x} = \{x_1, x_2\} \in \mathfrak{D} \subset \mathfrak{R}^2$, where θ is the random variable defined on the probability measure space $(\Omega, \mathfrak{F}, \mathbb{P})$. The random variable and the probability measure space are discussed in Appendix A.1. That random field is characterized using a probability density function and a PSD function described in the following. In addition, although the random surfaces are treated as non-Gaussian surfaces in this work, the useful properties obtained in the cases of Gaussian surfaces are also provided.

2.2.1 Estimating probability distribution of surface heights using maximum entropy principle

The probability distribution of the surface heights can be characterized through its moments m_k , with $k \geq 1$ the moment order, defined as

$$m_k = \int_{\mathfrak{R}} z^k p_Z(z) dz, \quad (2.1)$$

where p_Z is the probability density function of the random surface height Z . Specifically, the first two moments are the mean and the variance. Normalizing the third and fourth order moments, we obtain the skewness γ , and the kurtosis β respectively as

$$\gamma = \frac{m_3}{rms^3}, \quad \beta = \frac{m_4}{rms^4}, \quad (2.2)$$

where $rms = \sqrt{m_2}$ is the root mean square roughness. For the cases p_Z is a Gaussian distribution function, $\gamma = 0$ and $\beta = 3$. These moments are estimated, using ergodicity assumption, from the measurements as

$$m_k = \frac{1}{n_s^2} \sum_{i=1}^{n_s} \sum_{j=1}^{n_s} z(x_1^{(i)}, x_2^{(j)})^k, \quad (2.3)$$

where $z(x_1^{(i)}, x_2^{(j)})$ with $\{i, j\} \in [1, \dots, n_s]^2$ is a surface measurement obtained using AFM with sampling distance Δ_L , i.e. $x_1^{(i)} - x_1^{(i-1)} = x_2^{(j)} - x_2^{(j-1)} = \Delta_L$. From these moments, using the ME principle the probability distribution of surface heights can be identified to ensure that the distribution moments are matched. The ME method [54] consists in maximizing the Shannon measure of entropy [113] and is described as

$$p_Z \in \arg \max_{p_Z} S(p_Z) = - \int_{\mathfrak{R}} p_Z(z) \ln(p_Z(z)) dz, \quad (2.4)$$

subject to the constraint equations,

$$\int_{\mathfrak{R}} p_Z(z) dz = 1, \quad (2.5)$$

$$\int_{\mathfrak{R}} z^i p_Z(z) dz = m_i, \text{ with } i = 1, \dots, k, \quad (2.6)$$

in which the last k equations stated in Eq. (2.6) imply the constraints of moments equality. To solve the ME problem, the Lagrange's method is applied. The Lagrangian $\mathbf{L}(p_Z)$ is defined as

$$\mathbf{L}(p_Z) = S(p_Z) - (\lambda_0 - 1) \left(\int_{\mathfrak{R}} p(z) dz - 1 \right) - \sum_{i=1}^k \lambda_i \left(\int_{\mathfrak{R}} p(z) z^i dz - m_i \right). \quad (2.7)$$

where $\lambda_0, \dots, \lambda_k$ are $k + 1$ Lagrange parameters to be identified. The solution of zero Frechet derivatives of the Lagrangian $\mathbf{L}(p_Z)$ is given as [54]

$$p_Z(z) = \exp(-\lambda_0 - \sum_{i=1}^k \lambda_i z^i). \quad (2.8)$$

Remarks: (i) When there are only two constraints applied, i.e. the mean and the variance, the solution of the ME method is a Gaussian distribution. (ii) In order to ensure that $\lim_{z \rightarrow \infty} p_Z(z) < +\infty$, the maximum order of the matching distribution moment k must be an even number and $\lambda_k > 0$.

Identification of distribution parameters

The Lagrange parameters of the distribution function given by Eq. (2.8) are identified following the method developed in [5,69,108]. By imposing the $k+1$ constraints described in Eqs. (2.5, 2.6) on the form of $p_Z(z)$ in Eq. (2.8), one obtains $k+1$ nonlinear equations in the Lagrange parameters to be solved. Instead of directly solving these nonlinear equations, a potential function which reaches its minimum at the solution of these equations is defined. Using the condition $\int_{\mathfrak{R}} p_Z dz = 1$, the constraints in Eq. (2.6) are equivalent to

$$\int_{\mathfrak{R}} (z^i - m_i) p_Z(z) dz = 0, \quad \text{for } i = 1, \dots, k. \quad (2.9)$$

Toward the purpose of defining the potential function, a new parameter λ'_0 is defined as $\lambda'_0 = \lambda_0 + \sum_{i=1}^k \lambda_i m_i$. The distribution function given by Eq. (2.8) is thus rewritten as

$$p_Z(z) = \exp\left(-\lambda'_0 - \sum_{i=1}^k \lambda_i (z^i - m_i)\right). \quad (2.10)$$

Accounting for the condition stated in Eq. (2.5), the distribution function is normalized as

$$p_Z(z) = \exp\left(-\sum_{i=1}^k \lambda_i (z^i - m_i)\right) / g(\lambda_1, \dots, \lambda_k), \quad (2.11)$$

where g is a function of the Lagrange parameters $\lambda_1, \dots, \lambda_k$ given by

$$g(\lambda_1, \dots, \lambda_k) \equiv \exp(\lambda'_0) = \int_{\mathfrak{R}} \exp\left(-\sum_{i=1}^k \lambda_i (z^i - m_i)\right) dz. \quad (2.12)$$

Inserting the formulation of p_Z described in Eq. (2.11) into the condition stated in Eq. (2.9) yields the k nonlinear equations in the Lagrange parameters $\lambda_1, \dots, \lambda_k$ as

$$\frac{1}{g} \int_{\mathfrak{R}} (z^i - m_i) \exp\left(-\sum_{t=1}^k \lambda_t (z^t - m_t)\right) dz = 0, \quad \text{for } i = 1, \dots, k. \quad (2.13)$$

The function g defined in Eq. (2.12) has the following properties: (i) its gradient vector ∇g vanishes at the solution of Eq. (2.13), i.e.

$$\frac{\partial g}{\partial \lambda_i} = 0, \quad \text{for } i = 1, \dots, k; \quad (2.14)$$

and (ii) its Hessian matrix $[\nabla^2 g]$, given by

$$\frac{\partial^2 g}{\partial \lambda_i \partial \lambda_j} = \int_{\mathfrak{R}} (z^i - m_i)(z^j - m_j) \exp\left(-\sum_{t=1}^k \lambda_t (z^t - m_t)\right) dz, \quad \text{for } \{i, j\} \in [1, \dots, k]^2, \quad (2.15)$$

is symmetric and positive definite owing to the linear independence of the constraints stated in Eq. (2.6). Therefore, g is a strictly convex function and reaches its minimum at the solution of Eq. (2.13). By finding the minimum of the function g which is unique whenever it exists, one can obtain the solution of the Lagrange parameters. To solve that minimization problem, the Newton method is applied with the descent direction vector $-\nabla^2 g^{-1} \nabla g$. Note that to evaluate the integrals in the formulations of the gradient vector and the Hessian matrix, the Gauss quadrature rule is applied for computational efficiency purpose [108, 1].

2.2.2 Estimating the power spectral density

Autocovariance function

The random surfaces are spatially characterized by the ACF which is given by [95]

$$\begin{aligned} r_Z(x_1, x_2, \tau_1, \tau_2) &= \mathbb{E}(Z(x_1, x_2)Z(x_1 + \tau_1, x_2 + \tau_2)) \\ &= \int_{\mathfrak{R}^2} z \tilde{z} p_{Z(x_1, x_2), Z(x_1 + \tau_1, x_2 + \tau_2)}(z, \tilde{z}) dz d\tilde{z}, \end{aligned} \quad (2.16)$$

where \mathbb{E} is the expectation operation, and $p_{Z(x_1, x_2), Z(x_1 + \tau_1, x_2 + \tau_2)}$ is the second order probability density function of the surface heights. Using the stationary assumption, one has

$$r_Z(x_1, x_2, \tau_1, \tau_2) = r_Z(\tau_1, \tau_2). \quad (2.17)$$

From Eq. (2.16), we have

$$r_Z(0, 0) = m_2. \quad (2.18)$$

The correlation length, l^m is defined in this thesis based on the ACF using the condition

$$r_Z(\boldsymbol{\tau}) < 0.01 m_2, \quad \forall \|\boldsymbol{\tau}\| = \sqrt{\tau_1^2 + \tau_2^2} > l^m. \quad (2.19)$$

Power spectral density function

Since the ACF is positive semidefinite, there exists a finite measure ν on \mathfrak{B}^2 – the Borel σ -algebra over \mathfrak{R}^2 – satisfying [3]

$$r_Z(\tau_1, \tau_2) = \int_{\mathfrak{R}^2} \exp(i(\zeta_1 \tau_1 + \zeta_2 \tau_2)) \nu(d\zeta_1, d\zeta_2), \quad \forall \{\tau_1, \tau_2\} \in \mathfrak{R}^2, \quad (2.20)$$

where $\boldsymbol{\zeta} = \{\zeta_1, \zeta_2\} \in \mathfrak{R}^2$ are the wave numbers and $i^2 = -1$. Using Eqs. (2.18, 2.20), we have $m_2 = r_Z(0, 0) = \nu(\mathfrak{R}^2)$. The spectral distribution function $f_Z : \mathfrak{R}^2 \rightarrow [0, m_2]$ is defined as

$$\begin{aligned} f_Z(\boldsymbol{\zeta}) &= \nu((-\infty, \zeta_1], (-\infty, \zeta_2]), \\ &= \int_{-\infty}^{\zeta_1} \int_{-\infty}^{\zeta_2} \nu(d\zeta'_1, d\zeta'_2). \end{aligned} \quad (2.21)$$

Because $\nu(d\zeta_1, d\zeta_2)$ is non-negative, f_Z is absolutely continuous and monotonically increasing. The PSD function $s_Z : \mathfrak{R}^2 \rightarrow [0, \infty)$ is defined as

$$s_Z(\zeta_1, \zeta_2) = \frac{\partial^2 f_Z}{\partial \zeta_1 \partial \zeta_2} \geq 0. \quad (2.22)$$

With the defined formulation in Eq. (2.22), the PSD function describes the distribution of surface height variance m_2 into wave numbers. From Eqs. (2.21) and (2.22), one has

$$\nu(d\zeta_1, d\zeta_2) = s_Z d\zeta_1 d\zeta_2. \quad (2.23)$$

Replacing the term $\nu(d\zeta_1, d\zeta_2)$ in Eq. (2.20) by $s_Z d\zeta_1 d\zeta_2$, it turns out that the ACF is the inverse Fourier transformation of the PSD function. Hence, the PSD function is evaluated by a Fourier transform of the ACF, i.e.

$$s_Z(\zeta_1, \zeta_2) = \int_{\mathfrak{R}^2} r_Z(\tau_1, \tau_2) \exp(-i(\zeta_1 \tau_1 + \zeta_2 \tau_2)) d\tau_1 d\tau_2. \quad (2.24)$$

From Eqs. (2.16) and (2.24), the PSD function is evaluated directly from the AFM measurements of the surface heights using ergodicity assumption as follows [44]

$$s_Z(\zeta) = \lim_{\chi \rightarrow \infty} \frac{1}{\chi^2} |\hat{z}(\zeta)|^2, \quad (2.25)$$

where $\mathcal{X} \times \mathcal{X}$ is the truncated size of AFM measurements, and $\hat{z}(\zeta)$ is the Fourier transform of the surface $z(\mathbf{x})$ estimated as,

$$\hat{z}(\zeta) \simeq \sum_{i=1}^{n_s} \sum_{j=1}^{n_s} z(x_1^{(i)}, x_2^{(j)}) \exp(-i(\zeta_1 x_1^{(i)} + \zeta_2 x_2^{(j)})) \Delta_L^2. \quad (2.26)$$

Since the AFM measurements are discrete data and their measurement zone is finite, the measurable range of wave number is limited as $\{\zeta_1, \zeta_2\} \in \{[-\pi/\Delta_L, -\pi/\mathcal{X}] \cup [\pi/\mathcal{X}, \pi/\Delta_L]\}^2$ as stated in Nyquist-Shannon sampling theorem [132, 114, 96]. To ensure that the wave number domain is almost covered, it is required that $\Delta_L \ll l^m < \mathcal{X}$. Equation (2.26) is numerically evaluated using the fast Fourier transformation (FFT) algorithm for which the PSD function is evaluated at the discrete sampled wave numbers with a sampling distance π/\mathcal{X} . When other wave numbers inside the measurable range are required, e.g. when generating surfaces, the PSD function is evaluated either using the interpolation technique or using additional FFT evaluations, see Appendix. A.2. In this thesis, the interpolation technique is applied for simplicity purpose.

To analyze the PSD function, a concise way is to consider their moments, which are given by

$$m_{\text{PSD}}^{k_1, k_2} = \int_{\mathfrak{R}^2} s_Z(\zeta) \zeta_1^{k_1} \zeta_2^{k_2} d\zeta. \quad (2.27)$$

In fact, the low order moments, $0 \leq k_1 + k_2 \leq 4$, are of interest since they describe the statistical properties of the summits, see Sec. 2.2.3. Using Eqs. (2.18, 2.20, 2.23), it arises that

$$m_{\text{PSD}}^0 = m_2, \quad (2.28)$$

where m_{PSD}^0 is the simplified notation of $m_{\text{PSD}}^{0,0}$, and m_2 is the variance of surface heights given by Eq. (2.1). For the cases of isotropic surfaces, the PSD function is symmetric with respect to the origin $\{\zeta_1, \zeta_2\} = \{0, 0\}$, consequently, we have

$$\begin{aligned} m_{\text{PSD}}^{1,0} = m_{\text{PSD}}^{0,1} = m_{\text{PSD}}^{1,1} &= 0; \\ m_{\text{PSD}}^{1,3} = m_{\text{PSD}}^{3,1} = m_{\text{PSD}}^{3,3} &= 0; \end{aligned} \quad (2.29)$$

and

$$\begin{aligned} m_{\text{PSD}}^{0,2} = m_{\text{PSD}}^{2,0} = m_{\text{PSD}}^2; \\ m_{\text{PSD}}^{4,0} = m_{\text{PSD}}^{0,4} = m_{\text{PSD}}^4. \end{aligned} \quad (2.30)$$

2.2.3 Relations between spectral moments and summits statistical properties in cases of Gaussian surfaces

The summit radius is evaluated as the reciprocal of the average curvatures obtained along the x_1 , x_2 directions [94]. It is remarked that the second and fourth order PSD function moments, m_{PSD}^2 and m_{PSD}^4 , are equal to the variances of the first and second derivatives of the surface heights respectively [94]. Owing to these properties, the spatial density of summits \bar{N}_{sum} , the mean radius of summits \bar{R}_{sum} , and the standard deviation of the summits heights σ_{sum} , are evaluated from PSD function moments as [6, 42, 94]

$$\begin{aligned} \bar{N}_{\text{sum}} &= \frac{1}{6\pi\sqrt{3}} \frac{m_{\text{PSD}}^4}{m_{\text{PSD}}^2}, \\ \bar{R}_{\text{sum}} &= \frac{3\sqrt{\pi}}{8\sqrt{m_{\text{PSD}}^4}}, \\ \sigma_{\text{sum}} &= \sqrt{m_2 - \frac{3.717 \times 10^{-4}}{\bar{N}_{\text{sum}}^2 \bar{R}_{\text{sum}}^2}}. \end{aligned} \quad (2.31)$$

The formulations described in Eq. (2.31) were derived based on the mathematical representation of Gaussian surfaces reported in Sec. 2.3.1 [42, 94]. In GW model, the summits height distribution is assumed to follow a Gaussian distribution. Furthermore, an analytical expression of the joint distribution of summits radii and summits heights was also obtained for the case of Gaussian surfaces by Nayak in [94].

2.3 Surface generators

A surface generator is constructed in this section, using as input data the non-Gaussian probability density function and the PSD function evaluated using the characterization

process described in Sec. 2.2. The case of Gaussian surfaces is first described before dealing with the more complicating case of non-Gaussian surfaces.

2.3.1 Generator of Gaussian surfaces

For Gaussian distribution surfaces, the surface generator is constructed from the estimated PSD function following the works of Shinozuka [115] and Poiron and Soize [103]. For a chosen integer value of μ (described later in this section), the normal height \tilde{z} can be generated as

$$\tilde{z}(\mathbf{x}, \theta) = \sqrt{2\Delta\zeta^2} \Re \left[\sum_{l_1=1}^{\mu} \sum_{l_2=1}^{\mu} v_{(l_1, l_2)}(\theta) \sqrt{\frac{1}{(2\pi)^2} s_Z(\zeta_{l_1}, \zeta_{l_2})} \exp(i x_1 \zeta_{l_1} + i x_2 \zeta_{l_2} + i \psi_{(l_1, l_2)}(\theta)) \right], \quad (2.32)$$

where

- the values $\{(\zeta_{l_1}, \zeta_{l_2}), 1 \leq l_1, l_2 \leq \mu\}$ are samples in the wave number domain such that $(\zeta_{l_1}, \zeta_{l_2}) = (-\zeta_L + (l_1 - 1)\Delta_\zeta, -\zeta_L + (l_2 - 1)\Delta_\zeta)$, with $\Delta_\zeta = 2\zeta_L/\mu$;
- the values $\{\psi_{(l_1, l_2)}, 1 \leq l_1, l_2 \leq \mu\}$ are $\mu \times \mu$ independent realizations of a uniform random variable with value in $[0, 2\pi]$; and
- the values $\{v_{(l_1, l_2)}, 1 \leq l_1, l_2 \leq \mu\}$ are such that $v_{(l_1, l_2)} = \sqrt{-\log(\xi_{(l_1, l_2)})}$, where $\{\xi_{(l_1, l_2)}, 1 \leq l_1, l_2 \leq \mu\}$ are $\mu \times \mu$ independent realizations of a uniform random variable with value in $(0, 1]$. Note that ξ and ψ are statistically independent.

The random phases are used in Eq. (2.32) to ensure that the probability distribution of generated surface heights is Gaussian [3]. Equation (2.32) is implemented using the FFT algorithm.

Using Nyquist-Shannon sampling theorem [132, 114, 96], the highest wave number ζ_L is chosen such that $\zeta_L = \pi/\Delta_L$, with Δ_L the sampling distance of measurements. Let $\mathcal{X}' \times \mathcal{X}'$ be the required size of the generated surfaces. The value of μ is chosen such that $\mu = \mathcal{X}'/\Delta_L$, and the sampling distance of wave numbers Δ_ζ is thus obtained by $\Delta_\zeta = 2\pi/\mathcal{X}'$. The PSD function is required to be evaluated for the range, $\{\zeta_{l_1}, \zeta_{l_2}\} \in \{[-\pi/\Delta_L, -\pi/\mathcal{X}'] \cup [\pi/\mathcal{X}', \pi/\Delta_L]\}^2$. When the size of the generated surfaces is larger than the measurements size, i.e. $\mathcal{X}' > \mathcal{X}$, there are wave numbers out of the measurable range stated in Nyquist-Shannon sampling theorem. The PSD function is evaluated at these wave numbers using an interpolation technique from the measurable values, see discussion in Appendix. A.2. With this method, the generated surfaces are non-periodic.

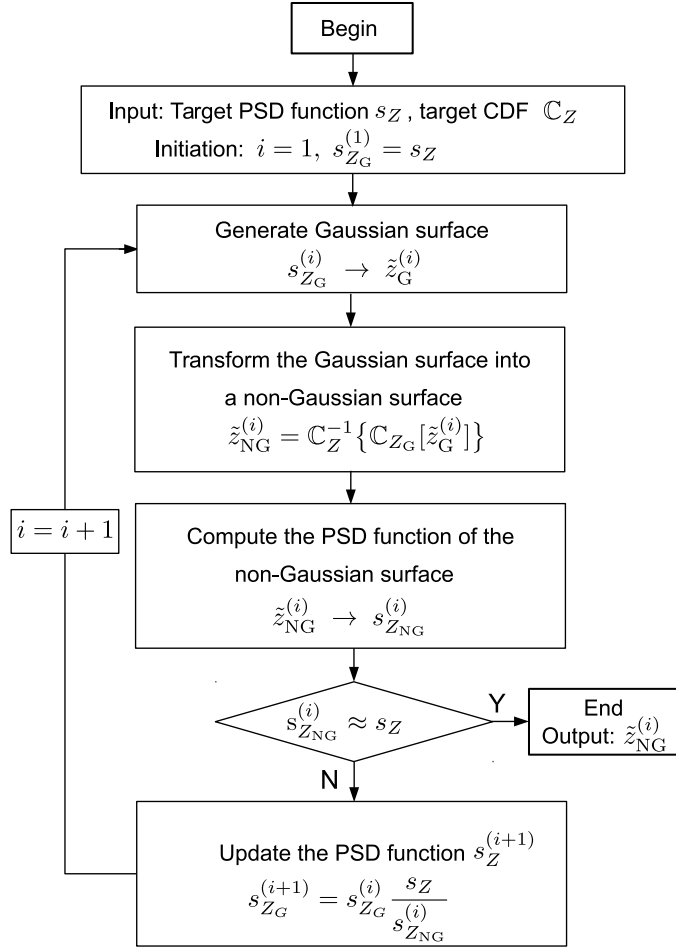


Figure 2.1: Algorithm to generate non-Gaussian surfaces respecting the target PSD s_Z , and the target non-Gaussian CDF \mathbb{C}_Z .

2.3.2 Generator of non-Gaussian surfaces

For non-Gaussian surfaces, the iterative generator developed in [104] is applied. In that method an iterative algorithm is required to ensure that the generated surfaces approximate well the target probability density function and the target PSD function, i.e. the ones obtained following Sec. 2.2. In this algorithm, see Fig. 2.1, at each iteration (i) , a Gaussian surface $\tilde{z}_G^{(i)}$ is generated from the PSD function $s_{Z_G}^{(i)}$ using the Gaussian surface generator described in Eq. (2.32). The PSD function $s_{Z_G}^{(i)}$ is adapted at each iteration and is equal to the target PSD function, s_Z , for the first iteration. In order to match the non-Gaussian probability distribution, these Gaussian surfaces are mapped using the cumulative distribution functions (CDFs) to the corresponding non-Gaussian one $\tilde{z}_{NG}^{(i)}$ following

$$\tilde{z}_{NG}^{(i)}(\mathbf{x}) = \mathbb{C}_Z^{-1} \{ \mathbb{C}_{Z_G}(\tilde{z}_G^{(i)}(\mathbf{x})) \}, \quad (2.33)$$

where \mathbb{C}_Z and $\mathbb{C}_{Z_G}(\tilde{z}_G^{(i)}(\mathbf{x}))$ are the CDFs of the target non-Gaussian surfaces obtained from the probability density function p_Z evaluated in Sec. 2.2.1, and of the Gaussian generated surface $\tilde{z}_G^{(i)}$ respectively. The mapping described in Eq. (2.33) is an isoprobabilistic transformation [110]. With that mapping, \tilde{z}_{NG} respects the target probability density function, however the PSD function is modified. The PSD function $s_{Z_{NG}}^{(i)}$ of the non-Gaussian mapped surfaces is estimated following Eq. (2.25) using the FFT method. At the end of each iteration, an adapted PSD function is thus computed following

$$s_{Z_G}^{(i+1)} = s_{Z_G}^{(i)} \frac{s_Z}{s_{Z_{NG}}^{(i)}}, \quad (2.34)$$

and is used for the generation of a new Gaussian surface in the next iteration. The process is repeated until reaching the condition $s_{Z_{NG}}^{(i)} \approx s_Z$.

Remarks on implementation. (i) To reduce the numerical errors when evaluating the PSD function of the non-Gaussian mapped surfaces, one can either increase the size of the generated numerical surface, or increase the number of numerical surfaces at each iteration. In the latter method, the PSD functions are evaluated for each numerical surface and then averaged to get the one whose numerical errors are reduced. Because the first method increases the computing memory, the latter method is chosen in this work. (ii) For a MCS, a large number of numerical surfaces is required. To generate the first numerical surface, the iterative algorithm is performed. However, for the next generations, the converged s_{Z_G} , is used directly to generate the Gaussian surfaces which are then mapped to obtain the non-Gaussian ones.

Sources of errors There are two sources of errors when applying the spectral representation method, i.e. data errors and modeling errors.

- (i) Data errors result from the measurement process, due to the measurement device and its operation. The setting parameters, such as the sampling interval, the measurement size, and the applied filters, might also induce errors on the measurement data.
- (ii) The modeling errors, in our cases, might result from the stationary assumption. For example, the grain boundary of polycrystalline materials might result in discontinuities on their surface topology and creates an error in the estimation of the PSD function. Especially for high wave numbers, the PSD function might be overestimated.

The treatment of these errors is not the subject of this works, however, their effects will be identified in the next section.

2.4 Applications

In this section, the characterization and simulation processes are applied on experimental surfaces. Two applications are considered: (i) the polysilicon surfaces fabricated by our

partner at IMT-Bucharest lab, and (ii) the (poly)silicon surfaces used in the stiction test reported in [151]. From the global view of the thesis, the generated surfaces will be used as the input data for the uncertainty quantification of the adhesive contact problems developed in the next chapters. Because the stiction test was not implemented for the first case (i), it is only for the study purpose, while the second one (ii) will be used for the validation of the model developed in this thesis.

2.4.1 Application 1: experimental surfaces fabricated at IMT-Bucharest lab

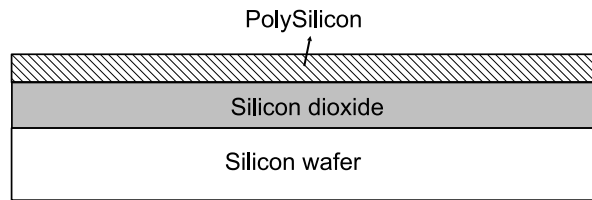


Figure 2.2: Cross section of the experimental samples. The polysilicon layers are deposited on the layer of silicon dioxide obtained using a thermal oxidation process from its silicon wafer.

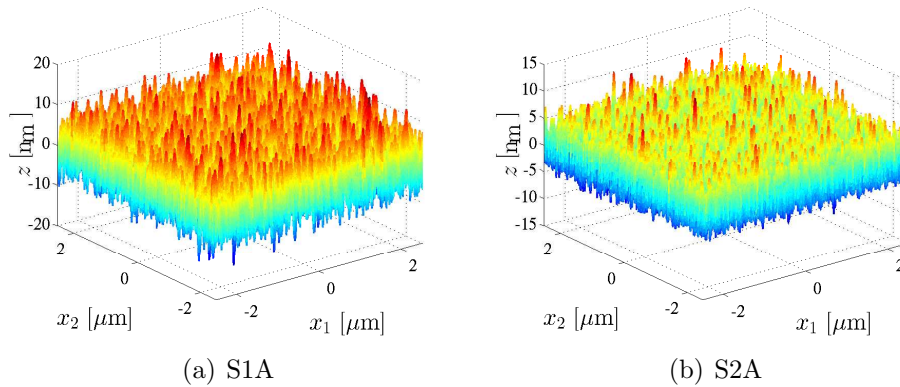


Figure 2.3: AFM measurements of S1A and S2A samples. Note that the scale along the z -axis is different with the x_1 , x_2 axes.

In the following, the fabrication process of the two experimental polysilicon samples, named S1 and S2, is briefly described. Owing to the AFM measurements of their surfaces, the spectral representation method is then applied to characterize and simulate their surfaces roughness.

2.4.1.1 Fabrication and measurement

Using surface micro-machining techniques, see Fig. 2.2, two polysilicon samples, named S1 and S2, were fabricated at IMT-Bucharest lab. From the $\langle 100 \rangle$ orientation silicon wafer of p-type, a silicon dioxide layer was grown by thermal technique at 900°C . On this silicon dioxide layer, a polysilicon layer was deposited using low pressure chemical vapor deposition (LPCVD) technique [51]. By controlling the temperature, the silane debit, and the deposit time of the LPCVD process, the obtained samples have different topological properties. A scanning electro microscope image of sample S1, shown in Fig. 1.2, illustrates the resulting surface topology on which the asperities can clearly be seen.

After manufacturing, the topologies of the two samples were measured by using the AFM technique at three different locations for each sample. These measurements are named S1A, S1B, S1C for the sample S1, and S2A, S2B, S2C for the sample S2. Each measurement has a size of $5.12 \times 5.12 \mu\text{m}^2$ with a sampling interval of $\Delta_L = 5 \text{ nm}$ and includes 1024×1024 measured points. Figure 2.3 illustrates the AFM measurements of S1A and S2A.

2.4.1.2 Characterization

The estimations of probability density function and PSD function of surface heights for the two samples S1, S2 based on these AFM measurements are described in the following. To reduce the data errors explained in Sec. 2.3.2, a low pass filter is applied on the AFM measurement data to eliminate the noise with a cutoff wave number of π/Δ_L , which is also the maximum measurable wave number following the Shannon-Nyquist theorem.

Table 2.1: The moments of the probability density function estimated from the AFM measurements of S1, S2 using Eq. (2.3).

	rms [nm]	γ [-]	β [-]
S1A	3.7	0.22	3.0
S1B	4.0	0.10	3.0
S1C	4.1	0.16	3.0
S1	4.0	0.16	3.0
S2A	2.0	0.53	3.5
S2B	2.1	0.51	3.4
S2C	2.1	0.48	3.4
S2	2.1	0.51	3.4

Estimation of the probability density function The variance, the skewness, and the kurtosis of the samples S1 and S2 are evaluated from the AFM measurements using Eq. (2.3). The obtained values are reported in Tab. 2.1. Between the two cases, S1 and S2, the non-Gaussian nature of S2 is more significant. The ME principle, described in

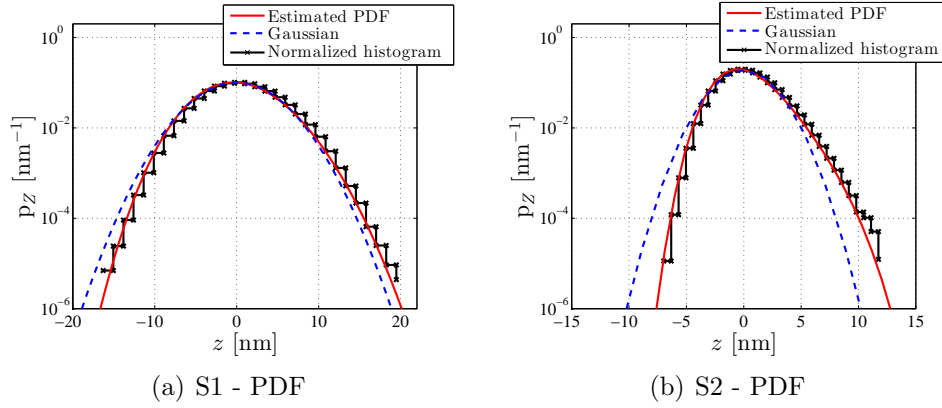


Figure 2.4: The probability density functions of surface heights obtained using the ME principle, (a) S1, and (b) S2, and the comparison between these distributions with the histograms evaluated from the AFM measurements. The case of Gaussian distributions is also reported.

Sec. 2.2.1, is applied to estimate the probability density functions of the random surfaces S1 and S2, using as the constraints the obtained first four moments (including the prescribed zero-mean). The results are illustrated in Fig. 2.4 where the logarithm scale is used to enhance the distribution resolution. The comparison of the histograms between the measurement data and the estimated ones, see Fig. 2.4(b, d), shows that probability density functions obtained by ME method approximate well the measurement data. In addition, in comparison with the Gaussian approximation, the obtained distribution functions show a significant improved accuracy when getting further from the mean value, especially in the case of S2. In the cases of S1 and S2, the skewness values are positive. As a result, in comparison with the Gaussian distributions for which the skewness is zero, the distributions obtained using the ME method are shifted to the right.

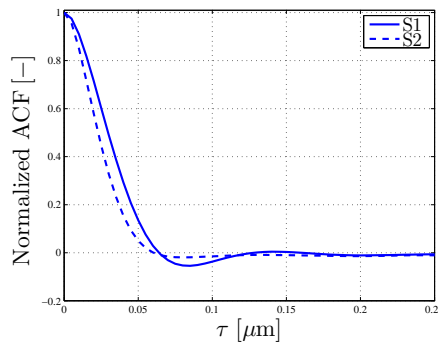
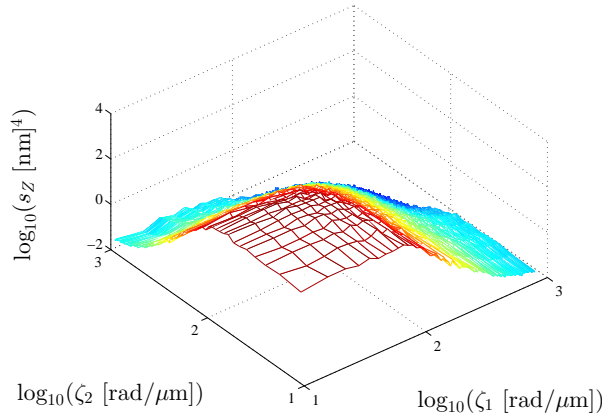
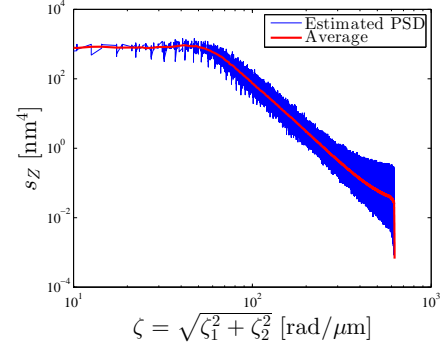


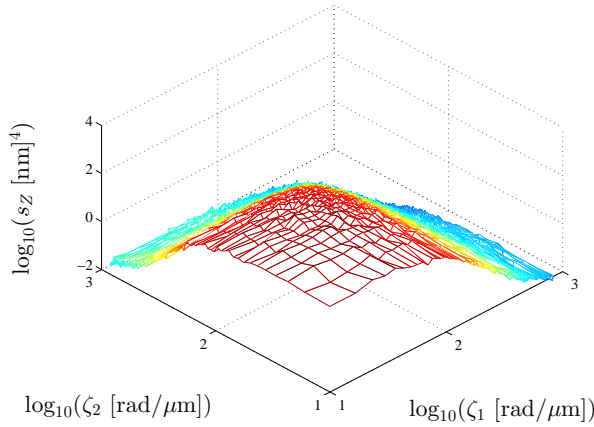
Figure 2.5: Normalized ACFs of S1 and S2 evaluated from AFM measurements.



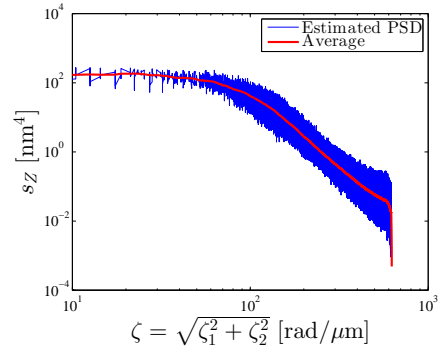
(a) 3D representation of S1 PSD



(b) Polar representation of S1 PSD



(c) 3D representation of S2 PSD



(d) Polar representation of S2 PSD

Figure 2.6: The estimated PSD functions of random surfaces S1, S2. Left, 3D representation, and right, polar representation.

Estimation of the PSD function The method described in Sec. 2.2.2 is applied here to evaluate the PSD functions of samples S1 and S2. In practice, as the measurement data are discrete and finite, the evaluation of the PSD function using Eq. (2.25) contains variance and bias errors. To reduce the variance in this estimation, the PSD function can be evaluated by averaging the calculated PSD functions for different surface measurements at different locations of the same sample following the method reported in [95], i.e. by

$$s_Z = \lim_{n \rightarrow +\infty} \frac{1}{n} \sum_{j=1}^n s_Z^{(j)}, \quad (2.35)$$

where n is the number of measurements and $s_Z^{(j)}$ is the PSD function evaluated for the measurement indexed (j) using Eq. (2.25). In our case, there are 3 measurements available at three different locations for each sample S1 and S2. To further reduce the variance error, each measurement is divided into 16 smaller surfaces of size $1.28 \times 1.28 \mu\text{m}^2$. The size of the divided surfaces remains larger than the correlation lengths of the random surfaces S1, S2 which are $\sim 0.2 \mu\text{m}$ as it is observed from the ACFs illustrated in Fig. 2.5. As a result, the statistical representativity of the divided surfaces is preserved, and the bias error remains negligible. The estimated PSD functions of samples S1, S2 are illustrated in Fig. 2.6(a, c). Using the assumption that the random surfaces are isotropic, the polar averages of the PSD functions are evaluated and illustrated in Fig. 2.6(b, d). These obtained isotropic PSD functions will be used to generate numerical surfaces in Sec. 2.4.1.3.

Remarks on the shape of the PSD functions: As it is observed from Fig. 2.6, the PSD functions have two important properties:

- (i) At low wave numbers, the PSD function is nearly constant; and
- (ii) At high wave numbers, the PSD function decays exponentially, i.e. decreases linearly in the log-scale. This is the self-affine property [80, 82].

These two characteristics were also experimentally observed for a large range of real surfaces [102].

2.4.1.3 Simulation of surfaces

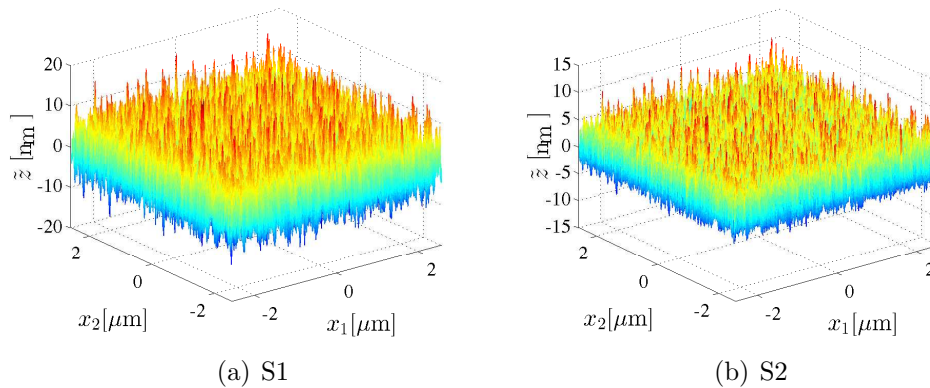


Figure 2.7: The generated surfaces for the cases of S1 and S2.

Using the stochastic model developed in Sec. 2.3, the samples of the random surfaces S1, S2 are numerical generated¹. Examples of generated surfaces are illustrated

¹Note that because the size of the generated surfaces is different and particularly bigger than the one of the AFM measurements, there exists additional sampling wave numbers on which the PSD function

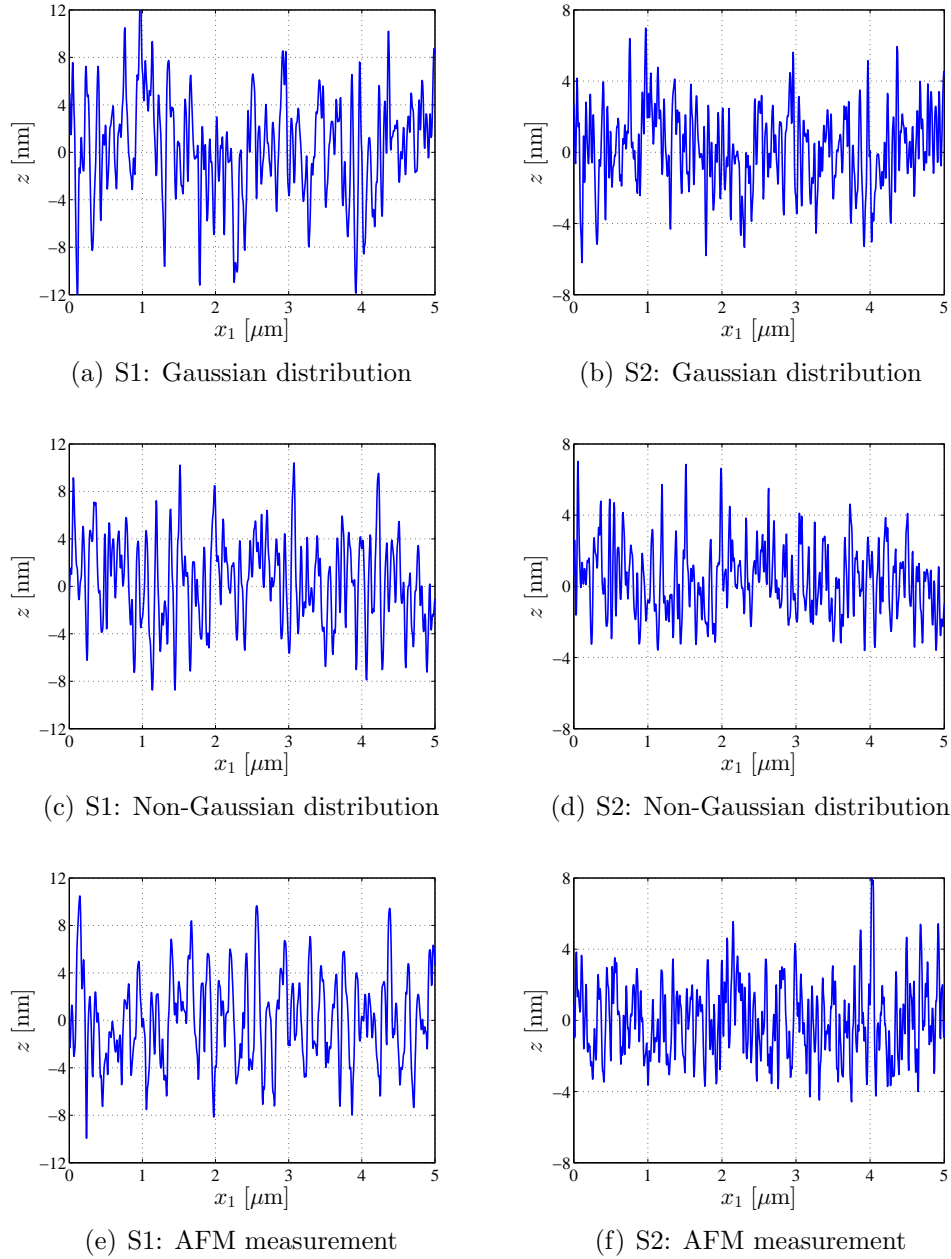


Figure 2.8: Comparison between the generated surfaces obtained for two cases: (a, b) using the Gaussian probability distribution of surface heights, (c, d) using the non-Gaussian probability distribution of surface heights, and AFM measurements (e, f). The surfaces S1 and S2 are considered respectively in the left and right columns.

should be estimated. At these points, the PSD function can be calculated either following the method described in Appendix A.2, or using an interpolation technique. In this work, the required values of PSD function are obtained by using the interpolation technique.

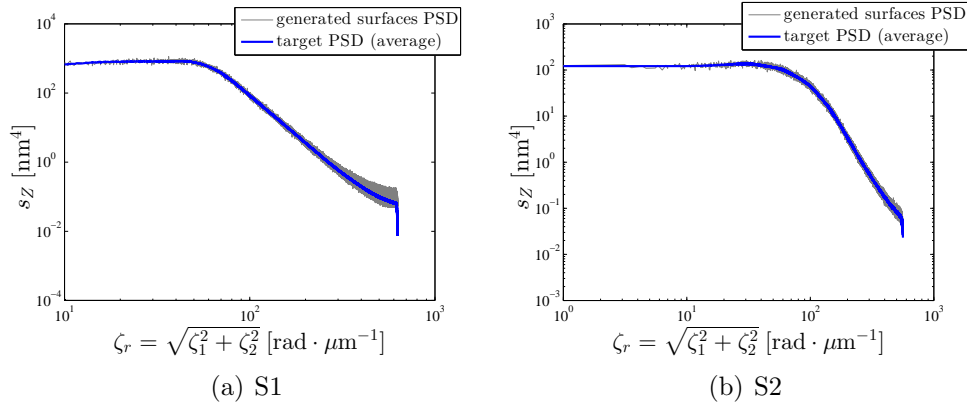


Figure 2.9: The comparison between PSD functions of the generated surfaces and the target ones, see Fig. 2.6, in polar coordinate.

in Fig. 2.7 and in Fig. 2.8 with 3D and 2D illustrations respectively. From the comparison among Gaussian generated surfaces, non-Gaussian generated surfaces, and AFM measurements in Fig. 2.8, it is observed that the surface heights are distributed nearly symmetrically with respect to the zero mean in the case of S1, while in the case of S2, these heights are significantly shifted to the positive values. This is due to the fact that the non-Gaussian characteristics are small for the case of S1, i.e. skewness $\gamma = 0.16$ and kurtosis $\beta = 3.0$, and become more important in the case of S2 with a significant positive skewness, i.e. skewness $\gamma = 0.51$ and kurtosis $\beta = 3.4$. For the developed generator, the probability density function of the generated surfaces is enforced to match the target one, thanks to the isoprobabilistic transformation in Eq. (2.33), while an iterative process is applied to obtain the target PSD function. As it is observed from Fig. 2.9, the target PSDs are well preserved.

In Tab 2.2, a comparison between the generated surfaces and the AFM measurements in terms of the probability distribution moments is reported. When considering the contact problem on the rough surfaces, in addition to these moments, the summit properties including mean radius and summits density, are also quantities of interest [42, 151]. Following [128], using the sampled surface topology, a summit is identified as a patch of 9 points peaking at the center point. Note that the summit differs from the asperity which can include more than 9 points. The mean radius of the summits is calculated as follows: the curvatures along each direction (x_1 , x_2) are computed using a 3-point central difference formula and averaged, and the mean summit radius of curvature for the whole surface is taken as the reciprocal of the mean of the average curvatures. To evaluate the summit characteristics, an interval of 20 nm is considered between sampled points. These characteristics are also reported in Tab 2.2. A good agreement is found between the non-Gaussian generated surfaces and the AFM measurements for the probability distribution moments, and summit density. The deviations are more important in terms of mean radius of the summits. However, these deviations still remain small in

Table 2.2: Comparison between AFM measurements and numerical surfaces, generated using Gaussian probability distribution (S-G) and non-Gaussian probability distribution (S-NG) of surface heights, in terms of roughness, skewness, kurtosis, mean radius of summits (\bar{R}_{sum}), and density of summits (\bar{N}_{sum}).

	S1			S2		
	AFM	S-NG	S-G	AFM	S-NG	S-G
rms [nm]	4	4	4	2.1	2.1	2.1
γ [-]	0.16	0.16	0	0.51	0.51	0
β [-]	3.0	3.0	3	3.4	3.4	3
\bar{R}_{sum} [μm]	0.090	0.061	0.065	0.093	0.074	0.083
\bar{N}_{sum} [μm^{-2}]	130	140	142	195	202	201

comparison with the observed range of summit radii, i.e. [30, 783] nm with a standard deviation of 41 nm for S1, and [38, 749] nm with a standard deviation of 38 nm for S2.

2.4.2 Application 2: on experimental surfaces used in the stiction tests reported in [151]

In this section, the developed method is applied to characterize and simulate the surfaces used in the stiction experiments reported in [151]. In this experiments set, two array samples of micro polysilicon cantilever beams and two substrates samples were fabricated. The probability distribution moments of the contacting surfaces, including the bottom surfaces of two different sets of cantilever beams, B1, B2, and the two substrate surfaces Sub1, Sub2, are reported in Tab. 2.3. The two spatial properties, the mean of summit radius and the density of summits are also reported in Tab. 2.3. The values of the mean summit radius and summits density depend on the sampling distance. It was reported to be 20 nm in the reference [124], which was also used for the numerical topology processing of the considered tests in [151].

2.4.2.1 Characterization

Estimation of the probability density function Based on the reported experimental data including roughness, skewness, and kurtosis, see Tab. 2.3, the non-Gaussian probability distribution of surface heights is estimated using the ME method developed in Sec. 2.2.1. The estimated distribution functions are illustrated and compared with the Gaussian distributions in Fig. 2.10. In contrast to the experimental surfaces in Sec. 2.4.1, the values of skewness are negative. The difference in the values of skewness as well as kurtosis is explained by a different fabrication process, i.e. in addition to the LPCVD steps as in the previous cases reported in Sec. 2.4.1, in the current case, an etching process was applied to make the cantilever beams free from substrates, and surface

Table 2.3: Comparison between the AFM measurements of contacting surfaces reported in [151] and numerical surfaces, generated using Gaussian probability distribution (S-G) and non-Gaussian probability distribution (S-NG) of surface heights, in terms of roughness, skewness, kurtosis, mean radius of summits (\bar{R}_{sum}), and density of summits (\bar{N}_{sum}).

	Bottom surfaces of the cantilever beams					
	B1			B2		
	AFM	S-NG	S-G	AFM	S-NG	S-G
rms [nm]	1.7	1.7	1.7	3.4	3.4	3.4
γ [-]	-0.78	-0.78	0	-0.76	-0.76	0
β [-]	4.6	4.6	3	3.9	3.9	3
\bar{R}_{sum} [μm]	0.41	0.41	0.30	0.84	0.85	0.56
\bar{N}_{sum} [μm^{-2}]	68	63	71	20.9	20.0	29.2

	Substrates					
	Sub1			Sub2		
	AFM	S-NG	S-G	AFM	S-NG	S-G
rms [nm]	0.17	0.17	0.17	5.5	5.5	5.5
γ [-]	-0.31	-0.31	0	-1.1	-1.1	0
β [-]	3.1	3.1	3	5.1	5.1	3
\bar{R}_{sum} [μm]	3.0	3.0	3.0	0.12	0.14	0.09
\bar{N}_{sum} [μm^{-2}]	111.5	109	115	48	59	68

pair a: B1 vs. Sub1, pair b: B2 vs. Sub1, pair c: B1 vs. Sub2

treatments such as annealing and oxygen plasma were applied ². Due to the negative skewness, in comparison with the Gaussian distributions for which the skewness is zero, the distributions obtained using the ME method are shifted to the left.

Estimation of the PSD function Because we do not have access to the AFM measurements of the surfaces, we cannot implement directly the estimation process described in Sec. 2.2.2. Instead, we use a cut-off self-affine PSD function [80,82] whose parameters are identified to satisfy the reported spatial parameters, including the density of summits and the mean radius of these summits, reported in Tab. 2.3. That PSD

²The effect of annealing and LPCVD processes on the surface topology was described in [150]. The plasma treatment was applied to obtain a super-hydrophilic state – a controlled condition applied for the stiction tests.

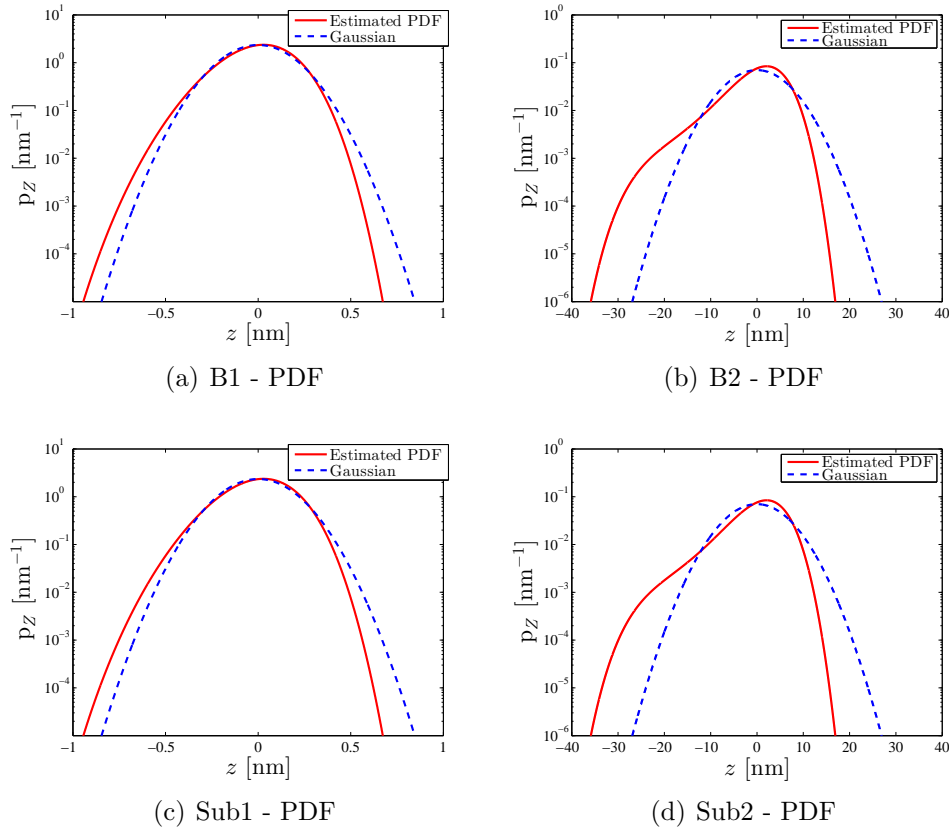


Figure 2.10: The probability density functions of surface heights obtained using the ME method with the moments reported in Tab. 2.3.

function is given by

$$s_Z(\zeta_r) = \begin{cases} s_Z^0 & \text{if } 0 \leq \zeta_r < \zeta_0 ; \\ s_Z^0 \left(\frac{\zeta_r}{\zeta_0} \right)^{\log_{10} \left(\frac{s_Z^1}{s_Z^0} \right) / \log_{10} \left(\frac{\zeta_{\max}}{\zeta_0} \right)} & \text{if } \zeta_0 \leq \zeta_r \leq \zeta_{\max} ; \\ 0 & \text{if } \zeta_{\max} < \zeta_r ; \end{cases} \quad (2.36)$$

where $\zeta_r = \sqrt{\zeta_1^2 + \zeta_2^2}$. Such a PSD function shape, see Fig. 2.11, was asymptotically verified versus the AFM measurements of surfaces S1, S2 in Sec. 2.4.1, as well as a large range of real surfaces [102]. When the surface heights follow a Gaussian probability distribution, the parameters of the self-affine PSD function can be identified from the mean summit radius, the summit density, and the root mean square roughness, owing to the relations between the PSD moments and these summit properties given in Eq. (2.31). For the non-Gaussian case considered in this work, we solved an inverse problem with an iterative process whose individual iteration is described here after.

- (i) From the mean summit radius \bar{R}_{sum}^G and the density of summits \bar{N}_{sum}^G , which are

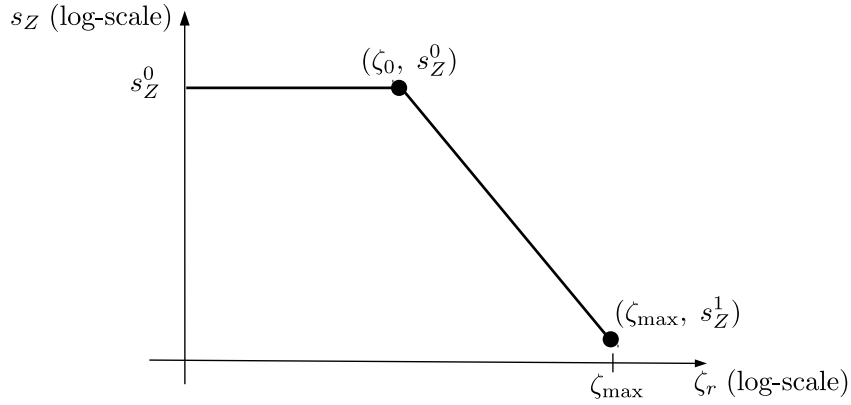


Figure 2.11: Theoretical cut-off self-affine PSD function.

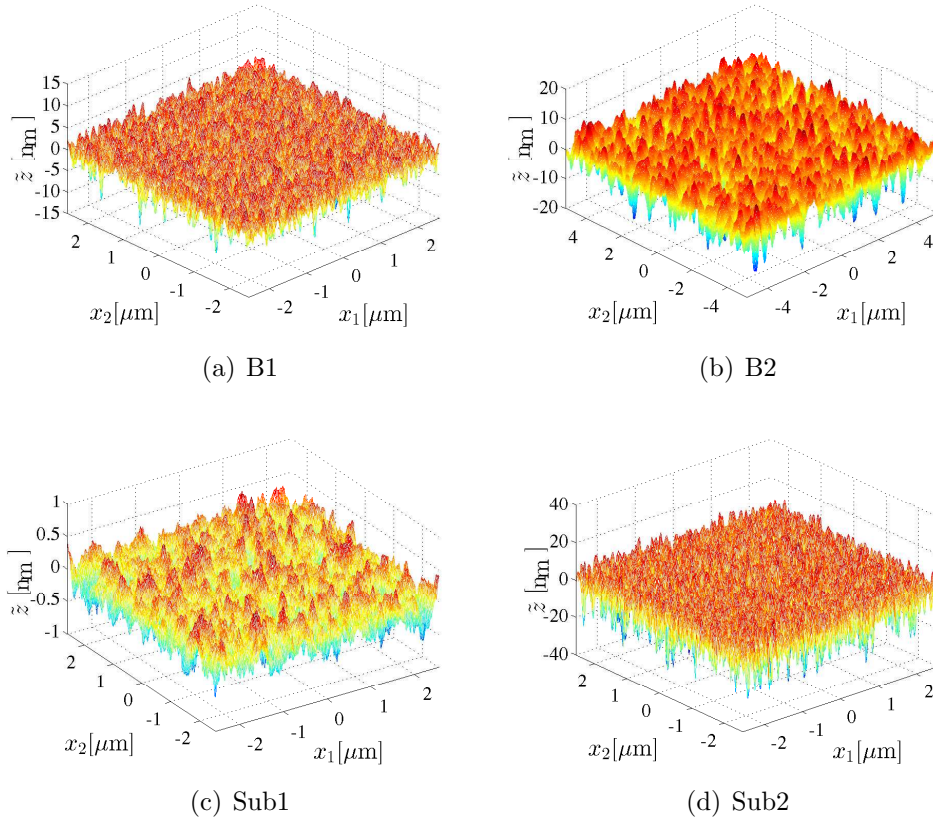


Figure 2.12: Generated surfaces for the cases of B1, B2, Sub1 and Sub2.

initiated to the target values at the first iteration, the PSD function parameters are identified based on the relations stated in Eq. (2.31).

- (ii) From the obtained PSD function, non-Gaussian surfaces are generated using the algorithm described in Sec. 2.3.

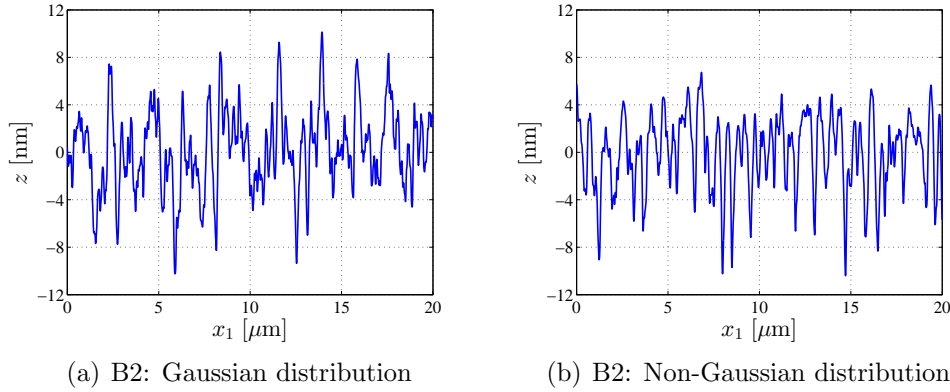


Figure 2.13: Comparison of generated surfaces. (a) using the Gaussian probability distribution of surface heights, and (b) using the non-Gaussian probability distribution of surface heights. The surface B2 is considered.

- (iii) The mean summit radius $\bar{R}_{\text{sum}}^{\text{NG}}$ and the density of summits $\bar{N}_{\text{sum}}^{\text{NG}}$ are evaluated from the generated non-Gaussian surfaces.
- (iv) If these summit properties agree with the target ones, the process is ended, else $\bar{R}_{\text{sum}}^{\text{G}}$ and $\bar{N}_{\text{sum}}^{\text{G}}$ are updated for the next iteration as: $\bar{R}_{\text{sum}}^{\text{G}} \leftarrow \bar{R}_{\text{sum}}^{\text{G}} \bar{R}_{\text{sum}} / \bar{R}_{\text{sum}}^{\text{NG}}$ and $\bar{N}_{\text{sum}}^{\text{G}} \leftarrow \bar{N}_{\text{sum}}^{\text{G}} \bar{N}_{\text{sum}} / \bar{N}_{\text{sum}}^{\text{NG}}$.

The identified parameters for the considered experimental surfaces are reported in Tab. 2.4.

Table 2.4: The parameters of the constructed PSD functions given by Eq. (2.36).

	B1	B2	Sub1	Sub2
s_Z^0 [nm^4]	525	1438	3.5	2471
s_Z^1 [nm^4]	0.8	0.3	0.001	0.2
ζ_0 [$\text{rad} \cdot \mu\text{m}^{-1}$]	32	12	10	56
ζ_{max} [$\text{rad} \cdot \mu\text{m}^{-1}$]	138	125	264	157

2.4.2.2 Simulation of the surfaces

Based on the evaluated probability density functions and the constructed PSD functions, numerical surfaces are generated using the method described in Sec. 2.3. The generated surfaces are illustrated in Fig. 2.12 and in Fig. 2.13 in 3D and 2D respectively. From the comparison between Gaussian generated surfaces and non-Gaussian generated surfaces illustrated in Fig. 2.13 for the case B2, it is observed that the surface heights are significantly shifted to the negative direction for the non-Gaussian ones. This is due

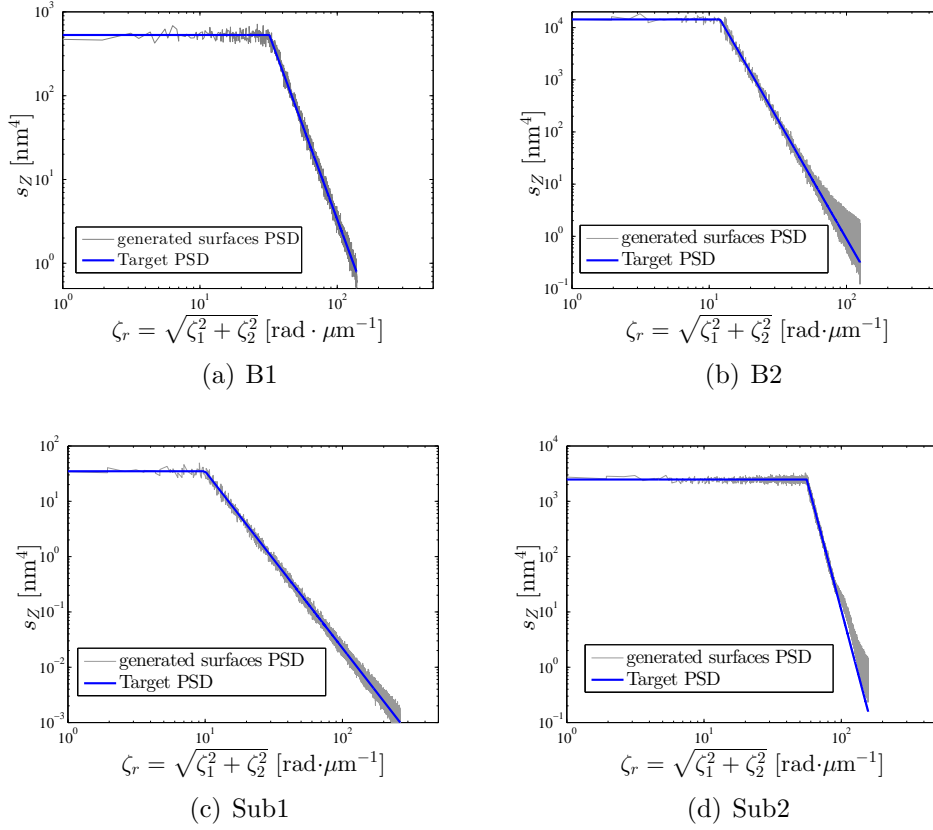


Figure 2.14: Comparison of the target PSD functions constructed using Eq. (2.36) with the coefficients given in Tab. 2.4, and the PSD functions evaluated from the generated surfaces. (a) B1 surfaces, (b) B2 surfaces, (c) Sub1 surfaces, (d) Sub2 surfaces.

to the fact that the non-Gaussian characteristics are important for this case and that the skewness is negative. That pattern is also found for the case of B1 and Sub2 for which the skewness and kurtosis are found to be similar. For the case of Sub1, the non-Gaussianity is much smaller. When generating non-Gaussian surfaces using the generator developed in Sec. 2.3, an iterative algorithm is applied to ensure that the PSD functions of the generated surfaces preserve well the target one. As it is observed in Fig. 2.14, this condition is numerically verified. For completeness, the ACFs of the generated surfaces are illustrated in Fig. 2.15.

The comparison between the measurement data and the numerical surfaces is reported Tab. 2.3. The moments including roughness, skewness, and kurtosis, are modeled with accuracy. For the spatial properties, because the PSD functions are indirectly estimated using the fractal formulation, Eq. (2.36), there exist errors in the density and the mean radius of the summits. These errors are negligible for B2 and Sub1 surfaces, moderate for B1 surfaces, and significant for Sub2 surfaces, i.e. 17% for the mean radius of summits and 23% for the density of summits. As a result, the numerical results when

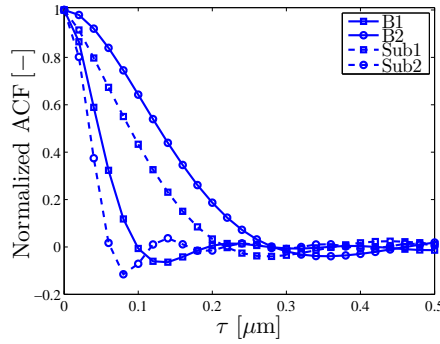


Figure 2.15: Normalized ACFs of generated surfaces Sub1, Sub2, B1, B2.

predicting the stiction phenomenon implemented in the next chapters might deviate from the experimental data for the stiction tests involving the substrate Sub2. The error in the summit mean radius of the case of Sub2 is comparable with the cases of S1 and S2 discussed in Sec. 2.4.1.2, however, the one in the summit density is much larger.

2.5 Conclusion

The randomness of the surface topology was characterized using the probability density function and the PSD function of surface heights. A non-Gaussian generator was constructed to generate the numerical surfaces respecting the obtained probability density function and PSD function.

The method was applied for two experimental cases: the fabricated polysilicon surfaces at IMT-Bucharest lab, and the (poly)silicon surfaces involved in the stiction tests in [151]. The results showed that the numerical surfaces match the target probability density function and PSD function evaluated from the characterization process. The comparison between Gaussian and non-Gaussian cases figured out that the non-Gaussianity should be accounted for to improve the accuracy when approximating the surface heights probability distribution.

With these generators, the numerical surfaces with the sizes of interest will be generated in the next chapter where an adhesive contact model is developed to evaluate the contact forces for these surfaces.

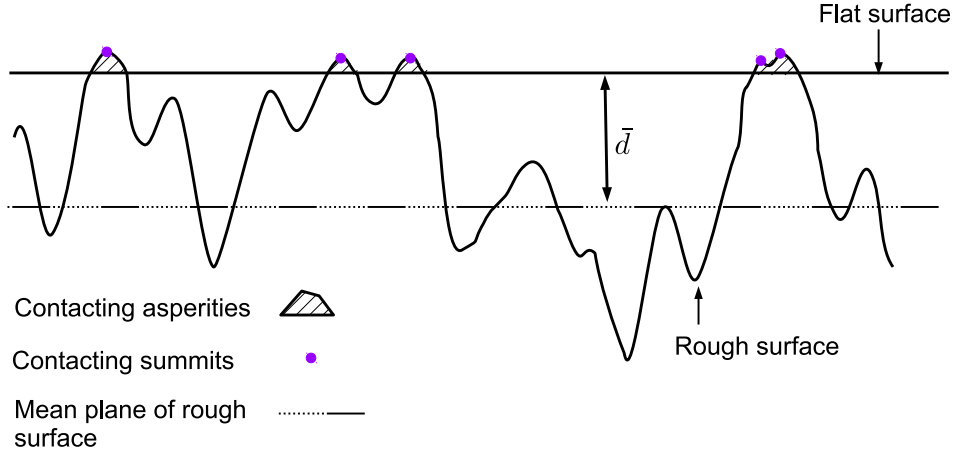
Chapter 3

Semi-analytical contact model for rough surfaces interactions

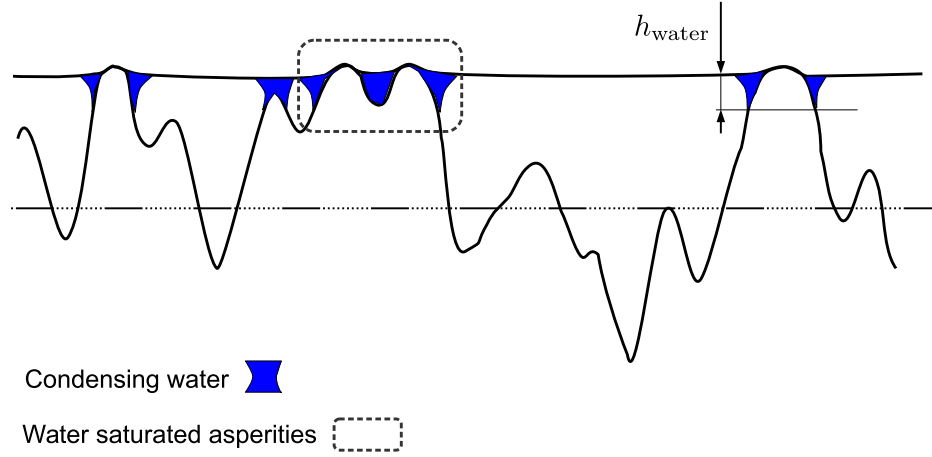
3.1 Introduction

This chapter develops a numerical model of the adhesive contact problem between rough surfaces, either characterized from the experimental surface measurements or generated using the surface generators developed in Chapter 2. Between two contacting surfaces, the vdW forces, a weak inter-molecular force, contribute to the adhesion of the contacting bodies [12, 46, 98, 35, 52, 122]. In addition, when two hydrophilic rough surfaces approach each other in air environment, the condensation of water vapor from the environment forms menisci which result in adhesive stresses due to the hydrogen bonds, see Fig. 3.1, [19, 16, 60, 2]. The menisci can be separated at different asperities or they can merge together at high humidity levels. This phenomenon is known as the saturation effect, see Fig. 3.1(b), [29].

To evaluate the adhesive contact forces between asperities, a popular methodology is to assume spherical asperities and to use an appropriate analytical asperity contact model, such as the DMT model [33], JKR model [57], or Maugis model [90], which are developed based on Hertz contact model [48] - an elastic non-adhesion contact model. The JKR model assumes soft material and short range adhesive stress, while the DMT model assumes hard material and long range adhesive stress. Between the two extreme cases, Maugis model is a transition one. These models and their underlying assumptions are described later in this chapter. To evaluate the adhesive contact forces between contacting rough surfaces, the summits-based statistical approaches such as the GW model [42] and the BGT model [20], which were developed using the multiple asperity contact theory, are widely used. These models rely on an important assumption, i.e. the Gaussian probability distribution of the surface heights which permits to derive analytically the distribution of the summits. In GW model, the summits are modeled with a constant radius and their heights follow a Gaussian distribution, see discussion in Sec. 2.2.3, [6, 94]. For BGT model, the constant radius approximation is relaxed,



(a) Reference configuration (not on scale)



(b) Deformed configuration (not on scale)

Figure 3.1: Contact configurations between a flat surface and a rough surface at contact distance \bar{d} . (a) Reference configuration with identified contacting asperities and contacting summits. (b) Deformed configuration with water menisci.

and the summits are described using a joint distribution function of their heights and of their principle curvatures. Owing to the summits distribution, the contact forces are evaluated by applying the appropriate analytical contact models, e.g. Hertz, DMT, JKR, or Maugis model, on these summits. At this step, the asperity and the summit are assumed to be equivalent. These analytical contact models have a negligible computational cost, which is their main advantage in comparison with the full numerical methods, e.g. FE method [9, 8, 7, 100, 153, 143, 142, 141] or MD method [74, 23]. However these summits-based statistical models should be employed with caution due to their limitations listed here below.

- (i) Because the size of the contacting surface is supposed to be infinite, the size effect,

required for a probabilistic analysis, is not accounted for. The assumption of the infinite surface size leads to the underestimation in the predicted adhesion energies, unless a cutoff on the support of asperity heights is introduced [29].

- (ii) The models are not applicable for non-Gaussian surfaces due to the basic assumption of Gaussian probability distribution.
- (iii) Assuming that one asperity corresponds to one summit is quite wrong as it was pointed out by Greenwood et al. in [41]. The summit is defined as a local maximum, while an asperity is what makes a contact [41,79], see Fig. 3.1(a). Due to the local property of summits, their radii depend on the sampling interval of surface measurements. In addition, an asperity can contain more than one summit, see Fig. 3.1(a).

Instead of using GW approach or a full numerical method, a semi-analytical adhesive contact model is developed to evaluate the contact forces between rough surfaces. Motivated by the multiple asperity contact theory, in this model the contacting asperities are identified from the surface topology and boundary conditions, i.e. contact distance \bar{d} see Fig. 3.1(a). These asperities are then fitted with spheres on which an appropriate analytical contact model is applied to evaluate the contact forces. The semi-analytical contact model overcomes the disadvantages of the GW model listed above, while the computational cost is still much cheaper than with full numerical methods owing to the integration of the analytical models. Because there exist interactions between asperities, e.g. the saturation effect, the integration of the analytical model is not implemented in a totally local way, i.e. asperity by asperity. Indeed, the interactions are evaluated based on their ranges, i.e. the short range elastic repulsive stress and vdW stress are evaluated using the asperity contact models, while the long range capillary interaction is evaluated in a global way for which the saturation effect is accounted for.

A limitation of the model is that the inter-asperities deformation is neglected. Indeed, the deformation of an asperity that results from its neighboring ones becomes important for soft contacting bodies under strong adhesive contact stress. In these cases, the asperities contact forces should not be evaluated separately. Another limitation results from neglecting the irreversible deformations such as plasticity. However, these limitations are beyond the considered cases in this thesis, because both the vdW and capillary interactions introduce weak stresses compared to the stiffness and strength of the considered material (polysilicon).

To verify the model, its prediction should be compared with an accurate model such as FE model. This step is not implemented in this thesis due to the difficulties when implementing the FE model for the considered adhesive contact problem. However, the numerical results will be compared with the experimental results in Chapter 5 to validate the developed methodology.

The chapter is developed as follows. In Sec. 3.2, the physical aspects of capillary and vdW forces are summarized. In Sec 3.3, based on DMT contact model, a modified DMT model is developed using the strategy of separating the interactions upon their ranges

of interaction. The strategy is applied for the spherical contact cases for verification purpose with the available analytical solutions. In Sec. 3.4, the semi-analytical model for interacting rough surfaces is developed. In Sec. 3.5, the semi-analytical model is applied for the surfaces described in Sec. 2.4. Based on the obtained results, we investigate the effects of the non-Gaussian probability distribution of surface heights and of the size of the contacting surfaces on the adhesion behaviors.

3.2 Physics of adhesive forces

In this section, the physical mechanisms of two adhesive interactions, capillary and vdW forces, are briefly described.

3.2.1 Capillary effects

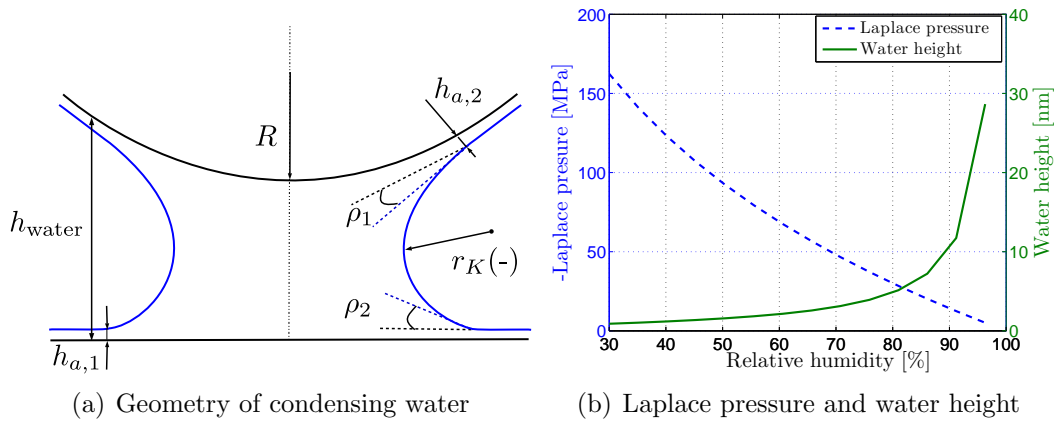


Figure 3.2: The configuration of condensing water. (a) Meniscus and absorbed surface layer between a sphere and a half space. (b) The evolution of the Laplace pressure and of the water height (without the absorbed surface layers thickness) in terms of the humidity level.

The capillary forces result from the negative pressure inside the condensing water between two hydrophilic contacting surfaces, see Fig. 3.2(a). The condensing water induces two phenomena, the creation of a meniscus and the appearance of absorbed surface layers, discussed in the following.

3.2.1.1 Water meniscus

In terms of dynamic behavior, during the separation process, the meniscus geometry varies depending on the competition between evaporation and condensation of water [30]. On the one hand, when the separation is fast, the volume of the meniscus is constant. On

the other hand, if the separation is slow the radius of meniscus and its water pressure are constant. Between the two extreme cases, the adhesion energy of the latter is reduced by a factor of 2 [30]. In this work, the assumption that the water pressure and the meniscus radius are constant is applied. Note that this assumption respects the condition of the experiments reported in [151] which are used to validate the methodology in this work. With the constant pressure assumption, the pressure inside the meniscus is equal to the Laplace pressure, which is evaluated at a given relative humidity level RH as [30,21]

$$\Delta P = \frac{\gamma_{\text{LG}}}{r_K} = \frac{\mathcal{R}T \ln RH}{V_m}, \quad (3.1)$$

where γ_{LG} is the liquid vapor energy, V_m is the liquid molar volume, \mathcal{R} is the universal gas constant, and T is the absolute temperature. In case of water condensation $V_m = 0.018$ L/mol and $\gamma_{\text{LG}} = 0.072$ N/m at $T = 300$ K. The geometry of the menisci is characterized by the contact angles $\{\rho_1, \rho_2\}$, depending on the surfaces properties, and by the Kelvin radius r_K given by [21]

$$r_K = \frac{\gamma_{\text{LG}} V_m}{\mathcal{R}T \ln RH} = \frac{0.53}{\ln RH} \text{ [nm]} < 0. \quad (3.2)$$

For the nano-scale rough surfaces, because the topology curvature is small, e.g. the radius of the contacting sphere is much larger than the Kelvin radius see Fig. 3.2(a), the capillary range, defined as the maximum contact distance at which water can condense between two bodies, is approximated by

$$h_{\text{water}} = -r_K (\cos(\rho_1) + \cos(\rho_2)). \quad (3.3)$$

The capillary forces in the present work are modeled using Dugdale cohesive model, i.e. inside the range h_{water} the pressure is constant and equal to the Laplace pressure, while outside this range the pressure vanishes. That model is consistent with the assumption of constant pressure [30].

The calculated Laplace pressures and condensing water heights for contact angles $\rho_1 = \rho_2 = 0$ are illustrated in Fig. 3.2(b). Since $0 \leq RH < 1$, from Eqs. (3.1, 3.2), the absolute value of the Laplace pressure decreases when raising the humidity level while the Kelvin radius increases, see Fig. 3.2(b). Note that $-h_{\text{water}} \times \Delta P$ is constant, and for contact angles $\rho_1 = \rho_2 = 0$, it is equal to $2\gamma_{\text{LG}}$. That value of $2\gamma_{\text{LG}}$ is also the theoretical value of the capillary energy, ω_{water} , which is reached when the contacting gap is totally saturated, i.e. either the contacting surfaces are perfectly flat or it has a roughness much smaller than the meniscus height. Furthermore, it can be observed that the Laplace pressure is much smaller than the Young's modulus of hard materials such as polysilicon, $E = 164$ GPa, while the condensing water heights are comparable with the roughness of the typical MEMS surfaces (nanometers) [29,32].

3.2.1.2 Absorbed surface layer

In humid air conditions, there exists a thin layer of water on hydrophilic surfaces called the absorbed surface layer, see Fig. 3.2(a). While its existence was experimental observed

Table 3.1: Dugdale model parameters of vdW forces.

Condition	vacuum	air $RH \sim 0$	air $RH > 0$
ω_{vdW} [J/m ²]	2.54	167.1 10^{-3}	87.4 10^{-3}
$-\sigma_{\text{vdW}}$ [GPa]	11.1	0.732	0.383
h_{vdW} [nm]	0.228	0.228	0.228

[11], it is still difficult to identify its thickness and to quantify its effects. Therefore, the absorbed surface layer is not accounted for in this thesis. With the assumptions that the pressure inside these layers is equal to the Laplace pressure, and the height of condensing water follows the superposition property, the phenomenon might be accounted for by adding the thicknesses h_{a_1} and h_{a_2} of the absorbed surface layers belonging to the two contacting surfaces into the height of the condensing water, see Fig. 3.2(a), as

$$h_{\text{water}} = -r_K (\cos(\rho_1) + \cos(\rho_2)) + h_{a_1} + h_{a_2}. \quad (3.4)$$

3.2.2 Van der Waals effect

The vdW interaction can be characterized by the adhesion energy per unit area, ω_{vdW} , given by

$$\omega_{\text{vdW}} = \frac{\mathfrak{H}}{16\pi D_0^2}, \quad (3.5)$$

where \mathfrak{H} is the Hamaker constant, and D_0 is the equilibrium distance at which the force between two half spaces is zero and is given by $D_0 = (2/15)^{1/6} r_0$ with r_0 the finite distance at which the inter-molecular potential is zero. For silicon, at room temperature, the Hamaker constant is 18.65×10^{-20} J through dry air, corresponding to $RH \sim 0$, and 9.75×10^{-20} J through water, which can be due to the menisci [22]. In practice, the polysilicon surfaces can be oxidized with thin layers (2-3 nm) of SiO₂ [122], and the Hamaker value may be changed. However the change remains lower by one order of magnitude. For the sake of simplification, the Hamaker values reported in [22] are considered in this work. For silicon, the distance $r_0 = 2.09$ Å [157] leading to $D_0 = 1.49$ Å. Using Dugdale assumption, the vdW stress, σ_{vdW} , is modeled as a constant for interaction distances smaller than the critical separation h_{vdW} , and vanishes outside this range. The energy balance leads to the relationship $\omega_{\text{vdW}} = -\sigma_{\text{vdW}} \times h_{\text{vdW}}$. For silicon, the range h_{vdW} can be deduced as $h_{\text{vdW}} = 0.97 \times 2^{1/6} r_0 = 2.28$ Å [146]. The modeling parameters of vdW interactions are reported in Tab. 3.1. In comparison with the capillary forces range h_{water} (\sim nanometers), the vdW force range h_{vdW} is much shorter. In addition, in vacuum condition and perfectly clean surfaces, the surface energy can reach the theoretical value if silicon fracture energy, i.e. 2.54 mJ/m² [22].

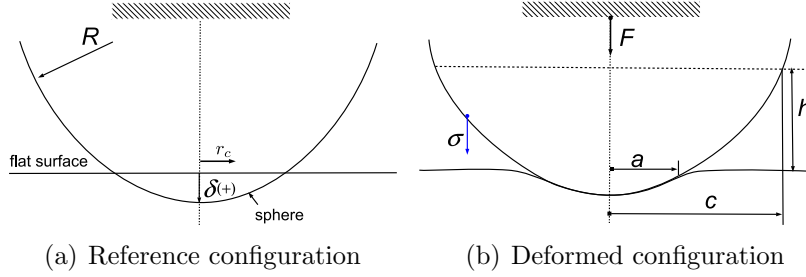


Figure 3.3: The configurations, (a) initial configuration and (b) deformed one, of the adhesive contact between a sphere and a flat surface. Depending on the considered physical problem, the adhesive interaction height h can be either the height of condensing water h_{water} or the range of the vdW adhesive pressure h_{vdW} , the adhesive interaction radius c can be either the water condensing radius c_{water} or the vdW adhesive radius c_{vdW} .

3.3 Evaluation of the asperity adhesive contact forces

3.3.1 Existing analytical contact models

In order to evaluate the adhesive elastic interaction forces between a sphere and a flat surface, there exist three well-known analytical adhesive contact models developed based on the Hertz model [48], i.e. the JKR [57], the DMT [33], and the Maugis [90] models. The details of these models are described in Appendix B.1. In addition to the common assumption that the radius of asperity is much bigger than the physical contact radius, i.e. $R \gg a$ see Fig. 3.3, the DMT and JKR models are respectively based on the following assumptions:

- (i) for the DMT model, the deformation resulting from the adhesive stress is neglected in comparison with the elastic deformation due to the physical contact, consequently the deformation is evaluated using Hertz model;
- (ii) for the JKR model, the adhesive stress outside the physical contact area is neglected.

As a result, while the DMT model is applicable for long range adhesive stress and hard materials, the JKR model is used for short range adhesive stress and soft materials. Between the two extreme cases, Maugis model is a transition solution. To identify the appropriate model, one can consider the transition parameter λ proposed by Maugis and evaluated as

$$\lambda = \left| \frac{2\sigma_0}{(\pi\omega K^2/R)^{1/3}} \right|, \quad (3.6)$$

where the two variables $\{\sigma_0, \omega\}$ can either hold for $\{\sigma_{\text{vdW}}, \omega_{\text{vdW}}\}$ or for $\{\Delta P, \omega_{\text{water}}\}$, depending on the application, and K is the reduced elastic modulus. K is evaluated as

$K = \frac{4}{3} [(1 - \nu_1^2)/E_1 + (1 - \nu_2^2)/E_2]^{-1}$ where ν_1, ν_2 are the Poisson ratios of the sphere and the half space respectively, and E_1, E_2 are their Young's moduli. The DMT model is applicable for $\lambda \ll 1$, while JKR is used for $\lambda \gg 1$. For the case of a polysilicon asperity with radius $R = 200$ nm - a typical measured radius [29, 32, 151], the values of λ and the applicable models are reported in Tab. 3.2 for different humidity levels. The considered polysilicon material has a Young's modulus $E = 164$ GPa and a Poisson ratio $\nu = 0.23$ [55]. Because silicon is a hard material in comparison with the adhesive stress of capillary and vdW interactions, the considered cases are compliant with the DMT regime for capillary interaction and with the Maugis regime for vdW interaction as it is reported in Tab. 3.2.

Table 3.2: The values of the transition parameter λ , Eq. (3.6), for a polysilicon sphere of radius 200 nm.

Humidity levels	$RH \sim 0$	$RH = 30 \%$	$RH = 50 \%$	$RH = 70 \%$
Capillary forces	-	$\lambda = 0.11$	$\lambda = 0.06$	$\lambda = 0.03$
vdW forces	$\lambda = 0.45$	$\lambda = 0.3$		
$\lambda \ll 1$: DMT model; $\lambda \gg 1$: JKR model; transition: Maugis model				

3.3.2 The modified DMT contact model: bridging asperity contact and rough surface contact models

The inter-asperities effects prevent a direct integration of the asperity contact model into the rough surface contact problem. In particular, for the case of capillary forces, a common phenomenon is saturation effect in which the menisci can merge together especially at high humidity levels, see Fig. 3.1(b). Therefore, to extend the applicability of the asperity contact models to rough surface contacts involving capillary forces, we modify the DMT contact model with an additional assumption: the deformation of an asperity at the points with a normal distance to the encountered plane larger than the capillary range h_{water} is negligible. This additional assumption is valid thanks to the fact that $\lambda \ll 1$ for capillary interactions as reported in Tab. 3.2. Using that additional assumption, we derive in a straightforward way the spherical asperity contact model, first for the capillary interactions, and then enhanced to account for the vdW interactions.

Capillary interaction cases In the original DMT theory, the adhesive force and the repulsive force are evaluated separately. The contact forces are calculated as $F = F_e + F_a$ where F_e is the elastic repulsive force, which can be obtained from Hertz theory, and F_a is the adhesive force resulting from the capillary interaction. The adhesive force is the integration of the Laplace pressure on the annulus between the contacting radius a and the water interaction radius c_{water} , i.e. $a \leq r_c \leq c = c_{\text{water}}$ see Fig. 3.3, and is thus computed as $F_a = \Delta P \pi (c_{\text{water}}^2 - a^2)$. Using the additional assumption that the radius

c_{water} depends only on the initial profile, one has

$$c_{\text{water}} = \sqrt{R^2 - (R - \delta - h_{\text{water}})^2}, \quad (3.7)$$

where δ is the interference, see Fig. 3.3. Eventually, the total adhesive contact force is evaluated by

$$F = F_r + \Delta P \pi (R^2 - (R - \delta - h_{\text{water}})^2 - a^2). \quad (3.8)$$

In Eq. (3.8), the repulsive force F_r and the contacting radius a are evaluated from the Hertz theory as

$$a^3 = \frac{RF_r}{K}, \quad (3.9)$$

$$\delta = \frac{a^2}{R}. \quad (3.10)$$

As it can be observed, this new method does not require the deformed profile as in the original DMT method. Owing to this relaxation, the modified DMT model is more flexible when applied to the rough surface contact problem in comparison with the Maugis and DMT models. Note that when $h_{\text{water}} \gg \delta$, one has

$$F \rightarrow F_r + 2\pi R h_{\text{water}} \Delta P = F_r - 2\pi R \omega_{\text{water}}, \quad (3.11)$$

which is the expression of the original DMT model, see Appendix B.1.

Verification of the modified DMT contact model The three candidate models, the Maugis, the DMT, and the modified DMT models, are compared on the contact problem between a spherical polysilicon asperity and a half space at different humidity levels. Two cases of radii of 100 nm and 800 nm are considered. The contact forces predicted by the three models are illustrated in Fig. 3.4. The extracted adhesion energies, i.e. the work required to separate the asperity from the plane, are reported in Tab. 3.3.

Table 3.3: Comparison of the adhesion energies [$\mu\text{N} \cdot \text{nm}$] obtained with the three methods.

Humidity level	$R = 100 \text{ nm}$			$R = 800 \text{ nm}$		
	30%	50%	70%	30%	50%	70%
Maugis	51×10^{-3}	81×10^{-3}	0.14	0.48	0.73	1.2
DMT	51×10^{-3}	81×10^{-3}	0.14	0.50	0.73	1.2
Modified DMT	52×10^{-3}	81×10^{-3}	0.14	0.52	0.75	1.2

As it is observed from Fig. 3.4 and Tab. 3.3, the differences in the results obtained by the three models are negligible. The largest difference is observed in the case of 800 nm-asperity radius at $RH = 30\%$ for which the difference in the adhesion energies is

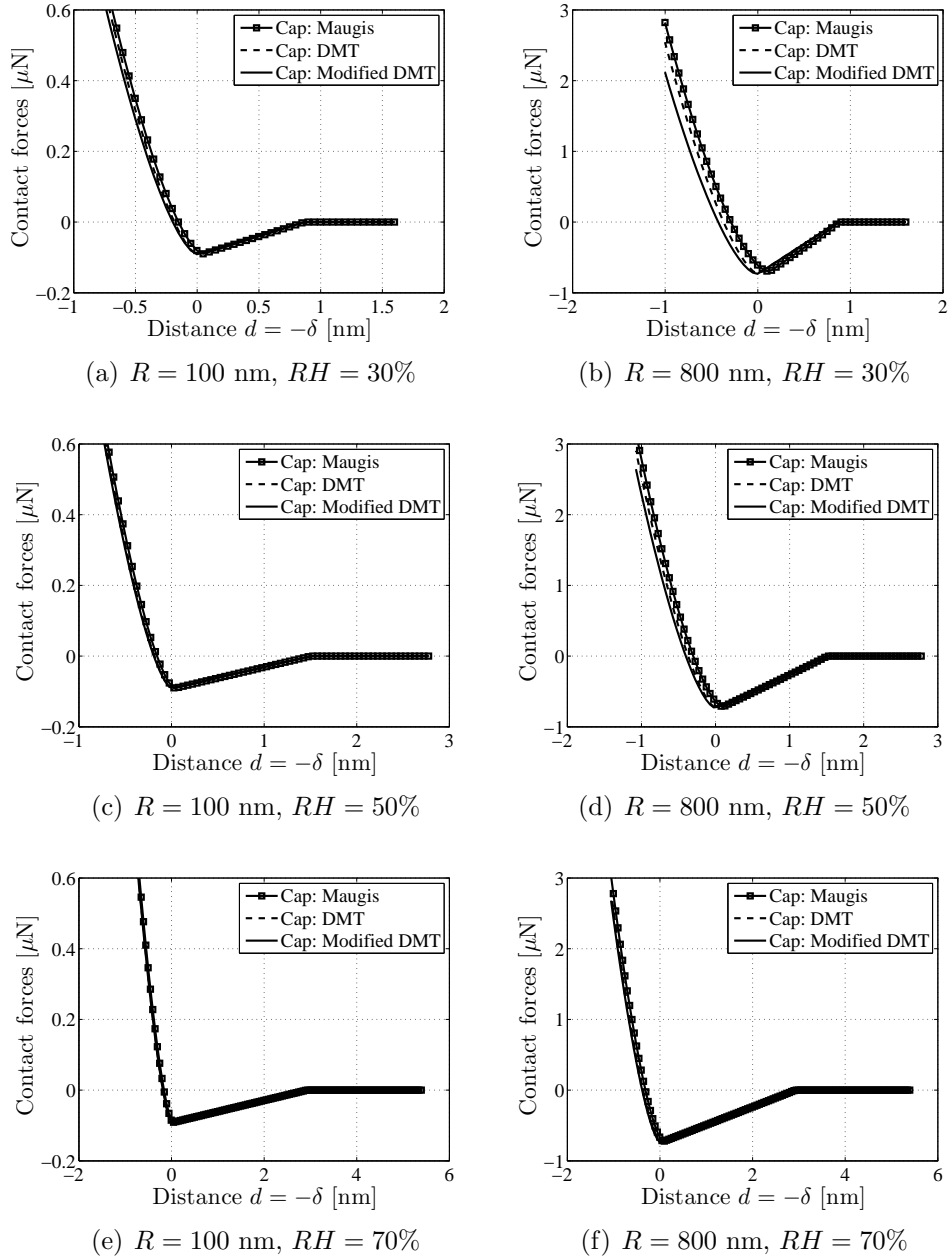


Figure 3.4: Comparison of the contact forces obtained by three methods, Maugis, DMT, and modified DMT, for polysilicon asperities of radii $R=100$ nm (left column) and $R=800$ nm (right column) at different humidity levels: 30% (first row), 50% (second row), and 70% (third row).

about 10% between the modified DMT method and the Maugis theory, and about 5% between the modified DMT method and the original DMT theory. For the other cases, the differences are below 3.3%. At 30% humidity level, the differences result from having

neglected the deformation due to the adhesive pressure in the two DMT models.

The negligible differences of the adhesion energies obtained by the three methods validate the second assumption of the modified DMT method: the deformation of asperity at a contact distance larger than the capillary range h_{water} is negligible. From this comparison we can conclude that besides Maugis model, which was proved to be valid to model the problem of humid stiction [91], both DMT and modified DMT models are applicable to our problem.

Extension of the modified DMT model to account for the vdW interaction

Because the vdW interaction range is sub-nanometer, see Tab. 3.1, its effects can be evaluated together with the elastic repulsive forces by applying the Maugis model [90], instead of Hertz model. The contact force formulation in Eq. (3.8) is extended as

$$F = F_{\text{Maugis}} + \Delta P \pi (R^2 - (R - \delta - h_{\text{water}})^2 - a^2), \quad (3.12)$$

where F_{Maugis} is the contact force resulting from the vdW interaction and elastic deformation, and is calculated using Maugis model, see Appendix B.1.4 for the explicit expression.

3.4 Semi-analytical model for rough surfaces contact

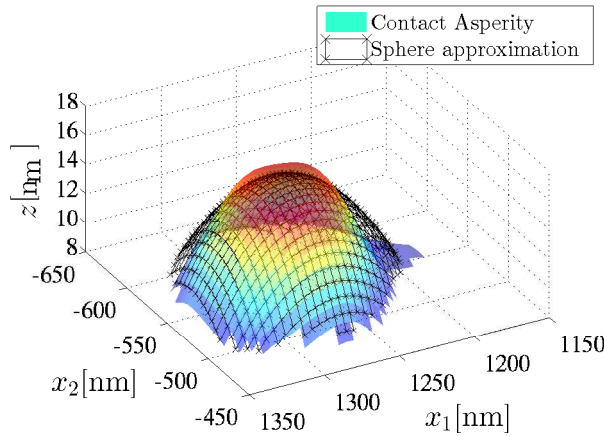


Figure 3.5: An example of fitting process: a contacting asperity identified and extracted from the surface topology and its spherical approximation.

A semi-analytical contact model is developed in this section to evaluate the adhesive contact between rough surfaces. The contact problem between two rough surfaces, e.g. z_1 and z_2 , is modeled as the contact between an equivalent rough surface, whose topology is evaluated as $z = z_1 + z_2$, and a flat surface, for which the gap between two undeformed

contacting surface topologies is preserved, see explanations in [56, page 411]. As a bridge, the modified DMT model developed and verified for the cases of spherical asperity contact in Sec. 3.3.2, is extended for the cases of rough surfaces contact. The assumption of that model is adapted for the cases of surface contact as follows: the deformation of the surface topology at contact distances larger than the capillary range h_{water} is negligible. Using that assumption, the long range interaction of Laplace pressure, and the short range interactions of vdW stress and elastic deformation, can be evaluated separately.

Let $z(\mathbf{x})$ with $\mathbf{x} \in [0, l_1^{\text{meso}}] \times [0, l_2^{\text{meso}}]$ be the topology of equivalent rough surfaces where $l_1^{\text{meso}} \times l_2^{\text{meso}}$ is the considered size. The model is developed in the four steps described in the following, see Fig. 3.6 for its algorithm sketch.

- (i) For a given contact distance \bar{d} , the contacting asperities are identified, see Fig. 3.1(a), and then fitted by spheres, see illustration in Fig. 3.5. The fitting method is described in detail in Appendix B.2. Let n_{asp} the number of identified asperities.
- (ii) The Maugis model, detailed in Appendix B.1.4, is applied on these approximated spherical asperities to evaluate their adhesive contact forces, $F_{\text{Maugis}}^{(i)}$ with $i = 1, \dots, n_{\text{asp}}$, resulting from vdW interaction and elastic deformation. The physical contacting area of each asperity, $A^{(i)}$, is also calculated by the Maugis model.
- (iii) The water condensing area A_{water} , see Fig. 3.1(b), is then evaluated as the differences between the area of parts of surface topology with interaction distances smaller than the capillary range h_{water} , and the sum of physical asperity contacting areas evaluated at step (ii) as

$$A_{\text{water}} = \int_0^{l_1^{\text{meso}}} \int_0^{l_2^{\text{meso}}} \mathbb{1}_{\leq 0}\{\bar{d} - z(\mathbf{x}) - h_{\text{water}}\} d\mathbf{x} - \sum_{i=1}^{n_{\text{asp}}} A^{(i)}, \quad (3.13)$$

where $\mathbb{1}_{\leq 0}\{\cdot\} = 1$ if $\cdot \leq 0$ and zero otherwise. The adhesive forces are then evaluated by multiplying the water condensing area with the Laplace pressure as

$$f_C = \Delta P A_{\text{water}}. \quad (3.14)$$

- (iv) The total contact force is the sum of the forces computed in steps (ii) and (iii). The apparent force is evaluated by dividing the obtained contact force with the apparent area of contacting surfaces as

$$\bar{f} = \frac{f_C + \sum_{i=1}^{n_{\text{asp}}} F_{\text{Maugis}}^{(i)}}{l_1^{\text{meso}} \times l_2^{\text{meso}}}. \quad (3.15)$$

The apparent contact forces have to be evaluated for a discrete set of contact distances $\{\bar{d}^0, \bar{d}^0 + \Delta\bar{d}, \dots, \bar{d}^0 + \kappa\Delta\bar{d}\}$ with $\Delta\bar{d}$ the sampling distance. Therefore, that process is repeated $\kappa + 1$ times in order to construct an apparent contact force vs. distance curve.

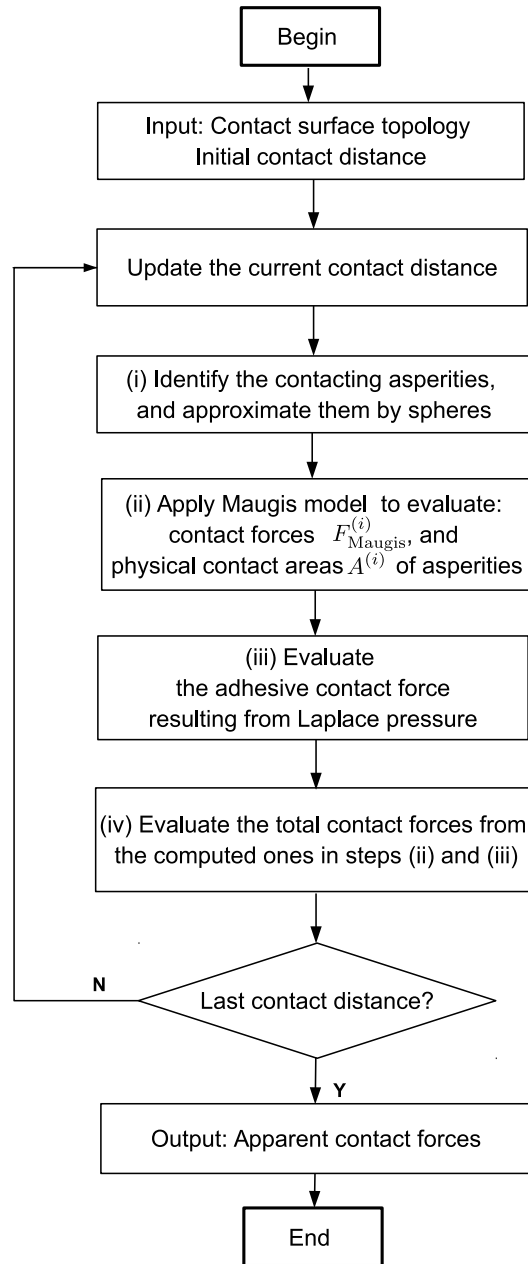


Figure 3.6: The algorithm of the semi-analytical contact models.

Errors control The accuracy of the semi-analytical model requires that the error when approximating the asperities by spheres remains small. This requirement is confirmed in Appendix B.2.2 for the cases considered in Sec. 3.5. In addition, to verify the model, a comparison with a higher fidelity model, e.g. FE model, should be performed. However, developing a FE model dealing with the non-linear adhesive contact forces on rough surfaces is not a trivial task, and therefore is not implemented in this work. Instead, the whole numerical approach developed in this work will be validated with the

experimental results.

Remarks on plasticity behavior Because both vdW stress and Laplace pressure are much smaller than the hardness of polysilicon, in this work the irreversible behaviors, such as plasticity, are neglected when evaluating the asperity interaction. To evaluate the importance of plastic deformation, a possibility is to compare the maximum stress given by Hertz model with the material hardness as it is described in Appendix B.3. A verification of the negligibility of irreversible deformation is also given in Appendix B.3 for the considered cases in Sec. 3.5. For the cases when irreversible deformations become non-negligible, the applied asperity contact models, Hertz and Maugis models, should be replaced, e.g. by the ones developed by L. Kogut and I. Etsion [66,67], or by the one developed by L. Wu et al. [144] in the case of cyclic loading.

3.5 Applications

The semi-analytical contact model developed in Sec. 3.4 is applied to evaluate the contact forces for the cases of the experimental surfaces and generated surfaces described in Sec. 2.4. For the surfaces fabricated at IMT-Bucharest lab, see Sec. 2.4.1, two contact pairs are considered: (i) pair I: between S1 vs. flat < 100 > silicon surface, and (ii) pair II: between S2 vs. flat < 100 > silicon surface. For the surfaces involved in the stiction tests reported in [151], see Sec. 2.4.2, three pairs are considered: (i) pair a: between B1 vs. Sub1, (ii) pair b: between B2 vs. Sub1, (iii) pair c: between B1 vs. Sub2. Because the stiction test is not available for S1 and S2, the pairs I and II are only considered for the illustration purpose, while for the pairs a, b, and c, the numerical predictions will be compared with the experimental data in Chapter 5 to validate the developed methods. The considered pairs are reported in Tab. 3.4. The statistical properties of the involved surfaces are found in Tabs. 2.2 and 2.3.

Table 3.4: The considered pairs of contacting surfaces.

pair I	pair II	pair a	pair b	pair c
S1 vs. flat	S2 vs. flat	B1 vs. Sub1	B2 vs. Sub1	B1 vs. Sub2
without stiction tests only for illustration purpose		used in stiction tests in [151] and considered to validate the methodology		

Two cases of the generated surfaces size, $l_1^{\text{meso}} \times l_2^{\text{meso}}$, are considered in this section: $5.12 \times 5.12 \mu\text{m}^2$ corresponding to the size of the AFM measurements of S1 and S2 reported in Sec. 2.4.1; and $1.5 \times 30 \mu\text{m}^2$. From the global view of the thesis, the contact forces will be integrated into the structural scale models developed in Chapter 5 where the size $l_1^{\text{meso}} \times l_2^{\text{meso}} = 1.5 \times 30 \mu\text{m}^2$ of generated surfaces is required.

Using the semi-analytical model developed in Sec. 3.4, the apparent adhesive contact forces are evaluated. For pair I and pair II, the semi-analytical model developed in Sec. 3.4 is first applied on the topology extracted from the AFM measurements. It is then applied on the numerical surfaces generated using the algorithm developed in Chapter 2. The predicted adhesive contact curves are illustrated in Fig. 3.7 and Fig. 3.8 for pair I and pair II respectively. From the obtained contact forces, the apparent adhesion energies \bar{e} are evaluated as

$$\bar{e} = - \int_{\mathfrak{R}} \mathbb{1}_{\leq 0} \{ \bar{f}(\bar{d}) \} \bar{f}(\bar{d}) d\bar{d} > 0. \quad (3.16)$$

The distributions of the apparent adhesion energies \bar{e} evaluated for pair I and pair II with the two considered surface sizes and at different humidity levels are illustrated in Fig. 3.9. For the pairs a, b, and c, the results are illustrated in Fig. 3.10 for the apparent adhesive contact forces, and in Fig. 3.11 for the distribution of their apparent adhesion energies.

Based on these results, the uncertainties in the adhesive contact forces, and their dependencies on the size of the surfaces, the humidity level, and the non-Gaussianity of surface heights probability distribution, are now discussed as well as the modeling errors when using the spectral methods.

Uncertainties The uncertainties in the apparent adhesive contact forces are significant, see Figs. 3.7, 3.8, and 3.10. These uncertainties result from the combination of the small interaction areas, e.g. in the range $10^{-6} - 1$ of the apparent one, with the limit size of the generated surfaces. As it is observed from Figs. 3.9 and 3.11, the lower the apparent energies, the higher their uncertainties.

Size effects From the comparison of the distributions of apparent adhesion energies \bar{e} illustrated in Fig. 3.9, it is observed that the uncertainties associated with the apparent adhesion energies are smaller for the larger surfaces. It is due to the statistical convergence following the law of large number [73]. In addition, when increasing the surface size, the mean values of the apparent adhesion energies are reduced. For the larger-size surfaces, the occurrence likelihood of the higher asperities increases. Although water condenses on these asperities increasing the adhesive forces, the repulsive contact behavior is then dominant and significantly reduces the adhesion behavior.

Effects of humidity level When rising the humidity level, the menisci height increases while the Laplace pressure proportionally decreases, see discussion in Sec. 3.2.1. With a larger menisci height, the area of condensing menisci on the contacting rough surfaces expands. Therefore, the apparent adhesion energies are significantly augmented when rising humidity level, as it is observed from Fig. 3.9. That observation also shows that the capillary interaction is more important than the vdW one in the considered cases.

Effects of non-Gaussian properties For the pair I, the non-Gaussianity in probability distribution of surface heights is not significant, and as a result the contact forces evaluated for generated Gaussian surfaces and generated non-Gaussian surfaces have similar shapes, see Fig. 3.7(b, c) and Fig. 3.7(d, e). For the other pairs: II, a, b and c, because the non-Gaussianity characteristics of surface heights probability distributions are more important, see Tabs. 2.2 and 2.3, there exists an important difference in the predicted adhesion behaviors of the Gaussian cases and non-Gaussian cases. By taking into account these non-Gaussian characteristics, the apparent adhesion energies are decreased for the pair II, see Fig. 3.8, but increased for the pairs a, b, c, see Fig. 3.11. This reflects the fact that the skewness of random surface S2 involved in pair II is positive while the skewness of surfaces B1, B2, and Sub2 involved in pairs a, b, and c, are negative, see Tabs. 2.2 and 2.3. When skewness is small, and particularly becomes negative, the contacting asperities heights are lower and more uniform while their radii are larger, see the investigation in Sec. 2.4, and consequently the apparent adhesion energies are higher [29]. Furthermore, the evaluated contact forces on the AFM measurements fall into the uncertainty ranges obtained using non-Gaussian generated surfaces, see Fig. 3.7(a, c) and Fig. 3.8(a, c), which is not the case for the Gaussian generated surfaces of pair II. These observations confirm the importance of accounting for the non-Gaussianity of surface heights probability distribution when predicting the adhesive contact behavior.

Effects of modeling errors of spectral representation method The modeling errors of the spectral representation method, described in Sec. 2.2, result in smaller summit radii for the generated surfaces compared to the AFM measurement data as discussed in Sec. 2.4.1.3. As a result, there exist errors in the predicted apparent adhesive contact forces and in their apparent adhesion energies \bar{e} . These errors might be identified by a comparison between the numerical results obtained from the generated surfaces, and from the AFM measurements, see Fig. 3.9 for pair I and pair II. However, such a comparison is difficult to be quantified due to the large uncertainty range of the obtained energies while there exist only three AFM measurements. The case of pair II at $RH = 90\%$ is the only exception in which the uncertainty of these energies is small. In this case, the average of the apparent adhesion energies is 0.034 J/m^2 for AFM measurements, and 0.04 J/m^2 for the generated surfaces. As it is observed, the bias error of the apparent adhesion energies is 15%. The numerical results show that the apparent adhesion energies vary in many orders of magnitude, e.g. for pair II: $\bar{e} \sim 10^{-7}, \dots, 10^{-5} \text{ J/m}^2$ at $RH = 30\%$ and $\bar{e} \sim 0.04 \text{ J/m}^2$ at $RH = 90\%$. Therefore, that bias error is acceptable. For the other cases, the apparent adhesion energies evaluated from AFM measurements fall into the uncertainty range evaluated from generated non-Gaussian surfaces, see Fig. 3.9. When there are more available AFM measurements, the predicted apparent contact forces can be calibrated, e.g by eliminating the bias errors.

3.6 Conclusion

In this chapter, a semi-analytical contact model was developed to evaluate the apparent adhesive contact forces between rough surfaces. The model is able to account for the size effects and therefore for the uncertainty of apparent adhesive contact forces. The model is efficient in terms of computational cost owing to the recourse to an analytical contact model. Using the developed semi-analytical contact model, the apparent adhesive contact forces were evaluated for the generated numerical surfaces and for the AFM measurements described in Chapter 2. The results confirmed the importance of the size effects and of the non-Gaussianity of surface heights probability distribution on the uncertainty of the apparent adhesion energies.

Toward the objective of this work, to quantify the uncertainty of the micro-structures behavior subjected to adhesive contact, a large amount of apparent adhesive contact forces are required. Therefore, we cannot rely solely on the limited surface topology obtained by AFM measurements, instead we have to use the numerical surfaces generated in Chapter 2. However, the total computational cost still remains high for stochastic multiscale analysis of MEMS behaviors. In order to reduce the required number of explicitly evaluated contact forces, a stochastic model is constructed in the next chapter to effectively represent the randomness of these forces.

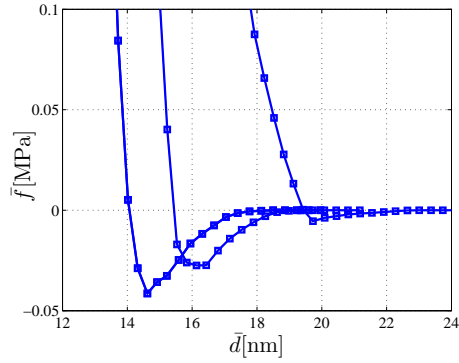
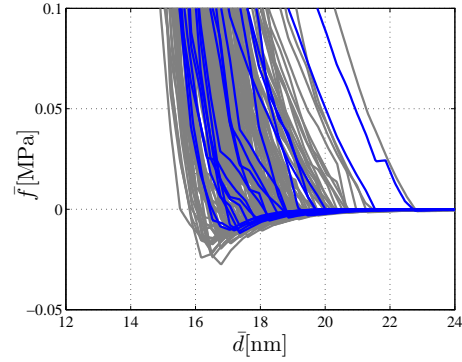
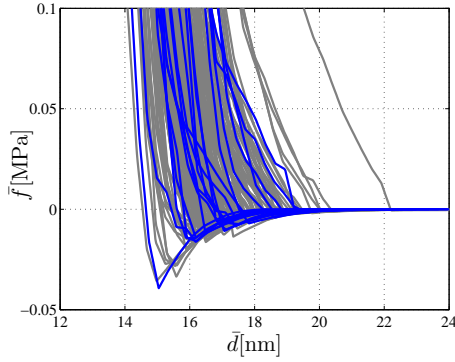
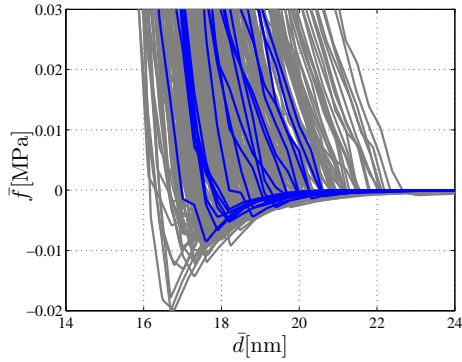
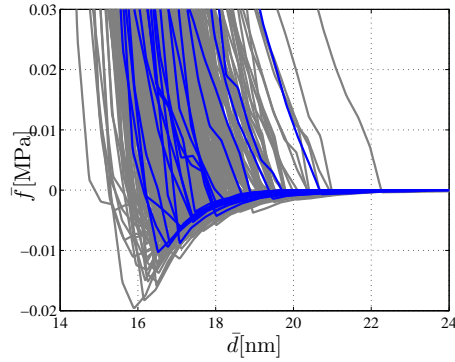
(a) AFMs: S1A, S1B, S1C, ($5.12 \times 5.12 \mu\text{m}^2$)(b) Gaussian surfaces ($5.12 \times 5.12 \mu\text{m}^2$)(c) Non-Gaussian surfaces ($5.12 \times 5.12 \mu\text{m}^2$)(d) Gaussian surfaces ($1.5 \times 30 \mu\text{m}^2$)(e) Non-Gaussian surfaces ($1.5 \times 30 \mu\text{m}^2$)

Figure 3.7: The apparent adhesive contact forces evaluated for pair I at $RH = 0.7$. Upper figures (a, b, c) report the contact forces for the surfaces of size $5.12 \times 5.12 \mu\text{m}^2$ including there cases: (a) AFM measurements, (b) generated Gaussian surfaces, and (c) generated non-Gaussian surfaces. Lower figures (d) and (e) report the contact forces for the surfaces of size $1.5 \times 30 \mu\text{m}^2$ for two cases: generated Gaussian surfaces and generated non-Gaussian surfaces respectively. For each figure (b, c, d, e), 20 realizations are highlighted from the 200 ones.

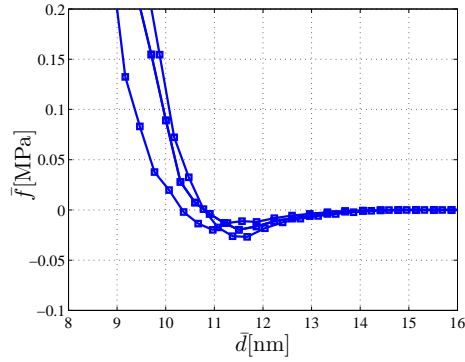
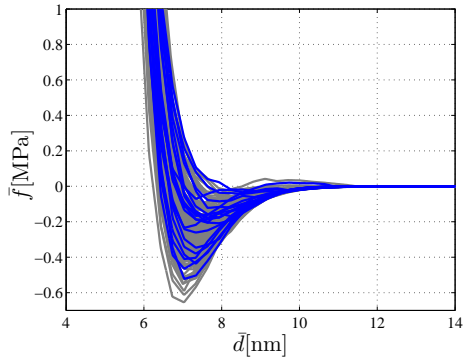
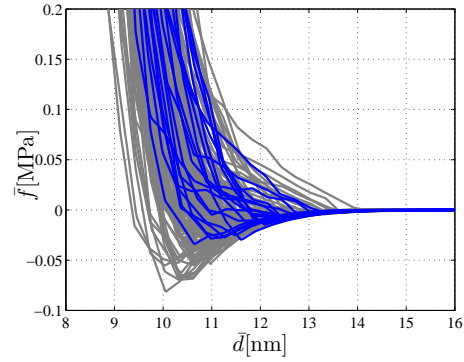
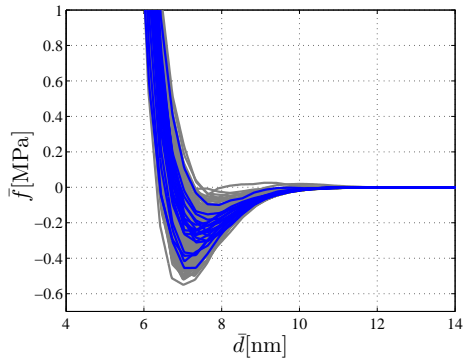
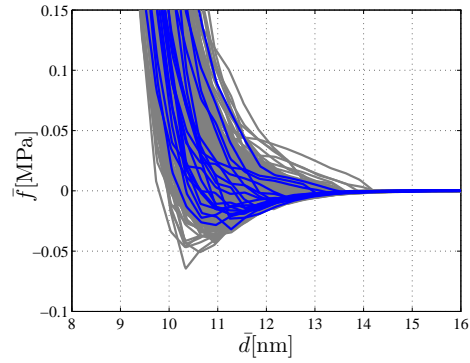
(a) AFMs: S2A, S2B, S2C, ($5.12 \times 5.12 \mu\text{m}^2$)(b) Gaussian surfaces ($5.12 \times 5.12 \mu\text{m}^2$)(c) Non-Gaussian surfaces ($5.12 \times 5.12 \mu\text{m}^2$)(d) Gaussian surface ($1.5 \times 30 \mu\text{m}^2$)(e) Non-Gaussian surface ($1.5 \times 30 \mu\text{m}^2$).

Figure 3.8: The contact forces evaluated for pair II at $RH = 0.7$. Upper figures (a, b, c) report the contact forces for the surfaces of size $5.12 \times 5.12 \mu\text{m}^2$ including there cases: (a) AFM measurements, (b) generated Gaussian surfaces, and (c) generated non-Gaussian surfaces. Lower figures (d) and (e) report the contact forces for the surfaces of size $1.5 \times 30 \mu\text{m}^2$ for two cases: generated Gaussian surfaces and generated non-Gaussian surfaces respectively. For each figure (b, c, d, e), 20 realizations are highlighted from the 200 ones. The y-axis ranges are different between (b) and (a, c).

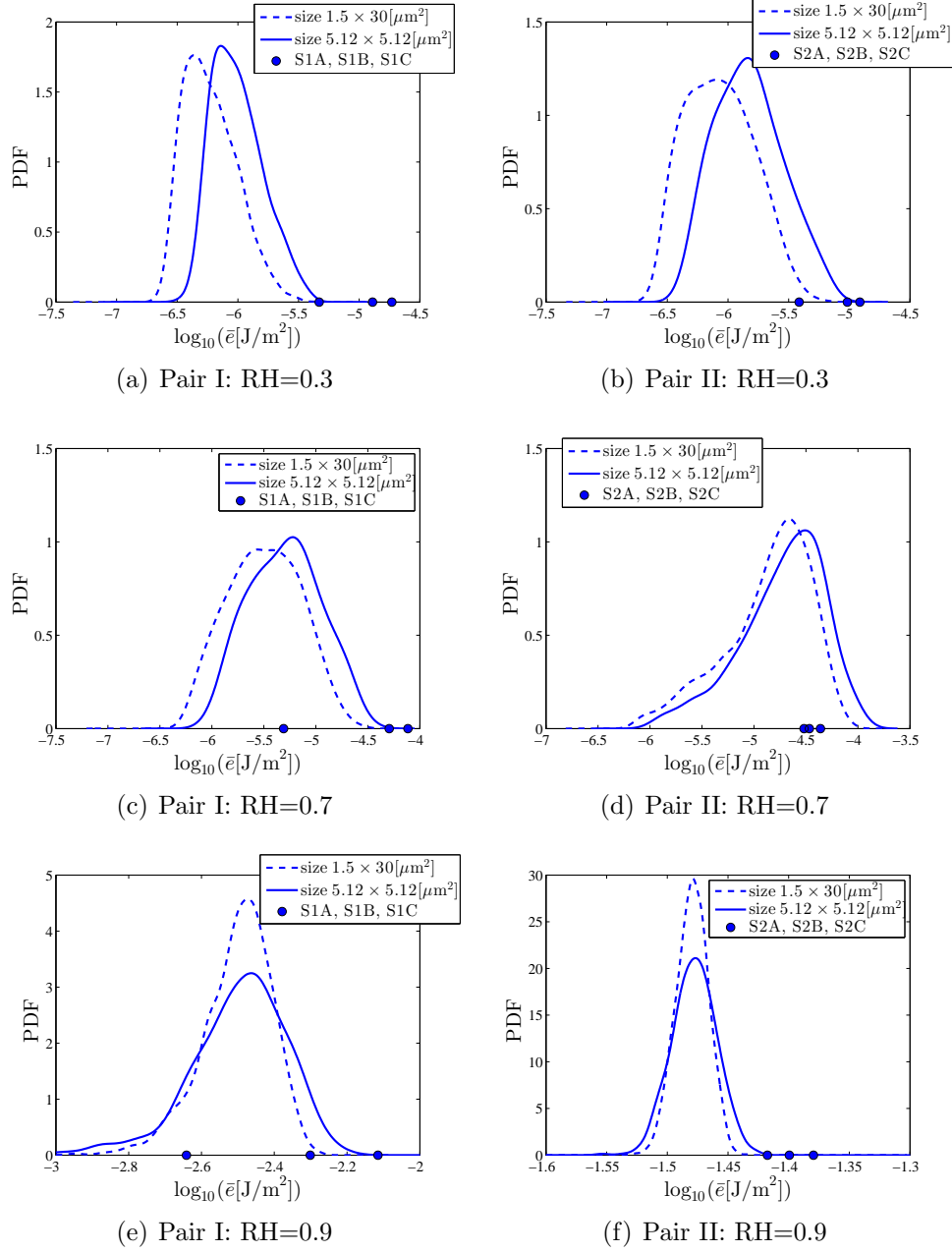


Figure 3.9: The distribution of the energies \bar{e} for the cases of pair I (left column), and pair II (right column), at different humidity levels, and for different generated surfaces sizes. The values of energy \bar{e} evaluated from AFM measurements are also given. The considered generated surfaces are the non-Gaussian ones.

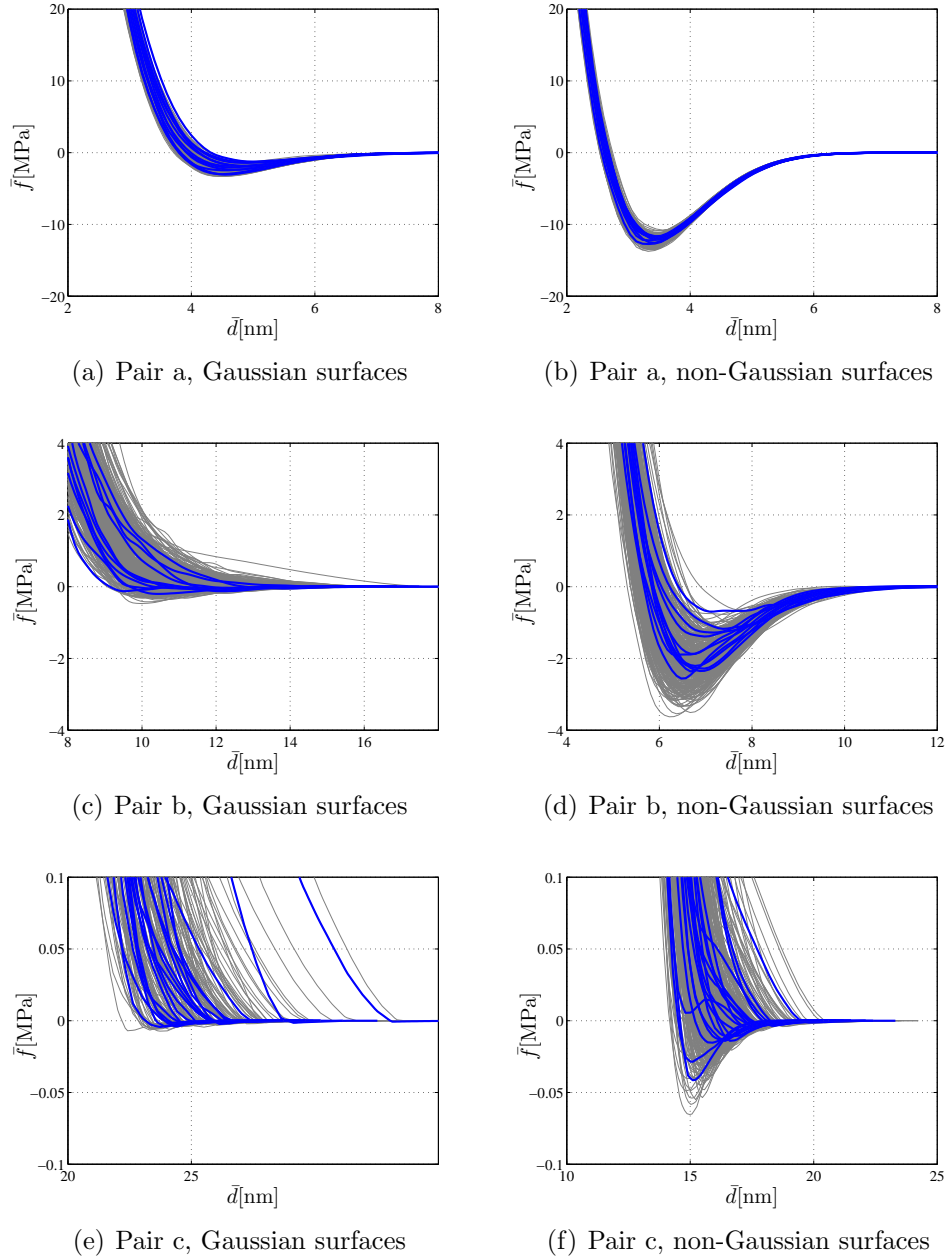


Figure 3.10: The apparent adhesive contact forces evaluated at $RH = 0.65$ for pairs a, b, and c. First column, (a, c, e), evaluated forces for Gaussian generated surfaces; second column, (b, d, f) evaluated forces for non-Gaussian generated surfaces. From top to bottom: pair a, pair b, pair c. For each figure, 20 realizations are highlighted from the 200 ones.

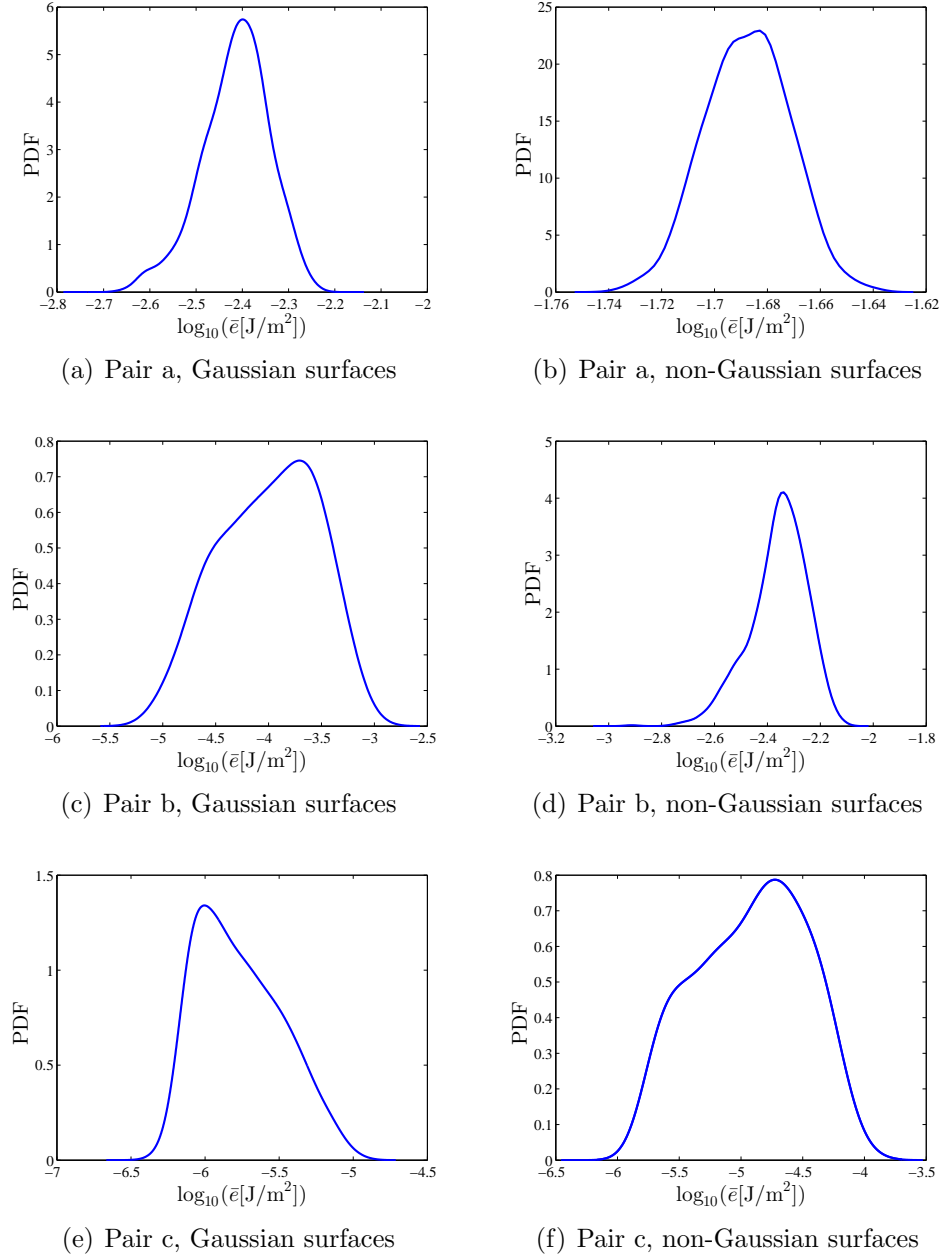


Figure 3.11: The distributions of apparent adhesive energies evaluated for pairs a, b, and c at $RH = 0.65$. First column, (a, c, e), the distributions of apparent adhesive energies evaluated for Gaussian generated surfaces; second column, (b, d, f) the distributions of apparent adhesive energies evaluated for non-Gaussian generated surfaces. From top to bottom: pair a, pair b, pair c.

Chapter 4

Probabilistic representation of the random apparent adhesive contact forces

4.1 Introduction

To reduce the number of explicitly evaluated apparent contact forces required for the MCS at the structural scale, a stochastic model of these forces is constructed. Toward this end, the apparent force vs. distance curves obtained in Chapter 3 are parametrized via an analytical adhesive contact function in order to be represented by vectors of parameters. The stochastic model is then constructed to generate random parameters vectors. To construct the stochastic model approximating the probability of the target random vector, common methods choose a labeled distribution, e.g. uniform, Gaussian or log-normal distribution ..., whose parameters are estimated using the input set of explicitly evaluated samples. An alternative method, based on the gPCE, see e.g. [39,119,10,118,34], constructs a transformation from a labeled random vector, whose distribution is known, to the target random vector. The second method is more flexible than the first one in approximating the studied random vectors as it can represent any second order random vectors and is therefore adopted in this work.

To identify the coefficients of the gPCE, one possibility is to solve the maximum likelihood problem [140]. Because of the high computational cost required when evaluating the gradients of the likelihood function as well as the possibility of multiple local maxima of this function, the gradient-free optimization methods, e.g the simulated annealing algorithm [64] and the genetic optimization algorithm [40], were applied in [105, 10]. Another approach is to project the Rosenblatt isoprobabilistic transformation [110], defined between the chosen labeled random variables and the target random variables, on the system of polynomial chaos functions owing to the orthogonal properties of this system [28]. Note that the projection is numerically achieved using quadrature rules. When the dimension of the target random variables remains small, i.e. ~ 3 , the eval-

uation of that projection is highly efficient in terms of computational cost. For higher dimension cases, the number of integral points required for the numerical projection increases exponentially, and as a consequence the computational efficiency is significantly reduced. In this work, the latter method is applied, however only after performing a dimension reduction [53, 58] to address the effect of the curse of dimensionality.

The structure of this chapter is developed as follow. In Sec. 4.2, the parameterization of the apparent adhesive contact forces is described, then in Sec 4.3 the stochastic model is developed to represent the randomness of the obtained parameters vectors. Finally, in Sec. 4.4, the stochastic models are constructed for the evaluated apparent adhesive contact forces reported in Sec. 3.5.

4.2 Parametrization of the apparent adhesive contact forces

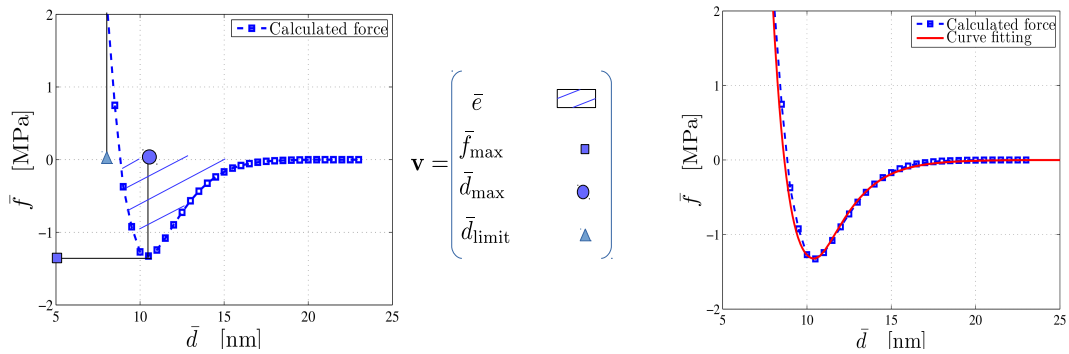


Figure 4.1: Curve fitting of a typical apparent adhesive contact force function. Left figure: An explicitly evaluated apparent contact force function, see Sec. 3.4, and its parameters. Right figure: The evaluated apparent contact force represented by the analytical function, Eq. (4.5).

The calculated apparent adhesive contact forces are first characterized by a set of physical parameters and then fitted by an analytical function derived from the Morse potential. In the context of adhesive problems, there are 4 key features characterizing the adhesive contact force \bar{f} which are listed here below.

- (i) The maximum pull-out adhesive force \bar{f}_{\max} defined by

$$\bar{f}_{\max} = \max_d \{-\bar{f}(d)\} > 0; \quad (4.1)$$

- (ii) The distance \bar{d}_{\max} at which the apparent contact force reaches its maximum adhesive force

$$\bar{d}_{\max} = \arg \max_{\bar{d}} \{-\bar{f}(\bar{d})\}; \quad (4.2)$$

- (iii) The apparent adhesion energy, \bar{e} , which has been defined in Eq. (3.16), as

$$\bar{e} = - \int_{\mathfrak{R}} \mathbb{1}_{\leq 0} \{\bar{f}(\bar{d})\} \bar{f}(\bar{d}) d\bar{d} > 0, \quad (4.3)$$

where $\mathbb{1}_{\leq 0} \{\cdot\} = 1$ if $\cdot \leq 0$ and zero otherwise;

- (iv) The threshold distance \bar{d}_{limit} at which the apparent contact force reaches a certain limit positive force \bar{f}_{limit} defined as the maximum considered compressive force of interest. Beyond this limit force, the compressive behavior dominates the adhesive behavior, and therefore is not relevant in the scope of an adhesive contact study.

These 4 key features of the adhesive contact force are represented by the parameters vector

$$\mathbf{v} = [\bar{e}, \bar{f}_{\max}, \bar{d}_{\max}, \bar{d}_{\text{limit}}]^T. \quad (4.4)$$

The following function is considered to fit the apparent adhesive contact forces

$$\mathcal{G}(\bar{d}) = \begin{cases} \bar{f}_{\max} (e^{-2a_{\text{right}}(\bar{d}-\bar{d}_{\max})} - 2e^{-a_{\text{right}}(\bar{d}-\bar{d}_{\max})}) & \text{for } \bar{d} \geq \bar{d}_{\max}; \\ \bar{f}_{\max} (e^{-2a_{\text{left}}(\bar{d}-\bar{d}_{\max})} - 2e^{-a_{\text{left}}(\bar{d}-\bar{d}_{\max})}) & \text{for } \bar{d} < \bar{d}_{\max}. \end{cases} \quad (4.5)$$

In fact, the fitting analytical function is derived from the well-known Morse potential¹. By separating the two wings with the different coefficients (a_{right} and a_{left}), the proposed function has four fitting coefficients, one more coefficient than the original Morse formulation. Consequently, it is consistent with the dimension of the parameter vector \mathbf{v} defined in Eq. (4.4). This fitting function reaches its maximum adhesive force \bar{f}_{\max} at a distance \bar{d}_{\max} . The other coefficients of the fitting function $\{a_{\text{right}}, a_{\text{left}}\}$ are identified by solving the following equations

$$\begin{aligned} \bar{f}_{\max} (e^{-2a_{\text{left}}(\bar{d}_{\text{limit}}-\bar{d}_{\max})} - 2e^{-a_{\text{left}}(\bar{d}_{\text{limit}}-\bar{d}_{\max})}) &= \bar{f}_{\text{limit}}; \\ - \int_{\mathfrak{R}} \mathbb{1}_{\leq 0} \{\mathcal{G}(\bar{d}; a_{\text{right}}, a_{\text{left}})\} \mathcal{G}(\bar{d}; a_{\text{right}}, a_{\text{left}}) d\bar{d} &= \bar{e}. \end{aligned} \quad (4.6)$$

One can thus obtain the physical parameters vector \mathbf{v} , Eq. (4.4), from a given sample of apparent contact forces and also can reconstruct that sample knowing its physical parameters vector using Eq. (4.5). In other words, an apparent contact force can be represented by the parameters vector \mathbf{v} .

¹Both the Morse potential, used to fit energy functions, and its derivative, used to fit distance-force curves, have the same characteristics since they are described by the exponential functions. Thus for simplicity the analytical function in Eq. (4.5) uses the Morse potential directly instead of its derivative to fit the adhesive contact forces.

4.3 Stochastic model of the random apparent adhesive contact forces based on the gPCE

Because there exist uncertainties in the apparent adhesive contact forces, see Sec. 3.5, the parameters vector defined in Eq. (4.4) is considered as a random vector denoted \mathbf{V} . A stochastic model is constructed using the gPCE to generate the realizations of that random vector from which the corresponding apparent adhesive contact forces are obtained using the adhesive contact functions defined in Eq. (4.5). The stochastic model is constructed based on a set of m explicitly evaluated apparent contact forces, see examples in Sec. 3.5, from which the set of m corresponding physical parameters vectors $\{\mathbf{v}^{(1)}, \dots, \mathbf{v}^{(m)}\}$ – samples of the random vector \mathbf{V} – is obtained using the parametrization process described in Sec. 4.2. The value of m is chosen such that the distribution of the random vector \mathbf{V} is evaluated with accuracy from the samples $\{\mathbf{v}^{(1)}, \dots, \mathbf{v}^{(m)}\}$.

Remark: As it will be shown in Sec. 5.3, the spatial correlation between two adjacent apparent adhesive contact forces is negligible. Therefore, the stochastic model developed in the following does not take the spatial correlation into account. For the cases of non-negligible spatial correlation, the model can be extended, e.g. by coupling a Karhunen-Loève expansion with the gPCE stochastic model as developed in [25, 26, 10].

In the considered problem, the construction of the stochastic model must deal with two challenges: (i) the stochastic model must respect the physical bounds of the modeled random variables, i.e. the generated samples are preconditioned by those bounds; and (ii) the effect of curse of dimensionality [118], i.e. the number of orthogonal polynomials in a gPCE model which increases exponentially with the dimensionality, must be minimized. Although the dimension of the target random vector \mathbf{V} is only four, it is still useful to apply a dimension reduction process to reduce the computational cost when evaluating the coefficients of the gPCE model. These challenges are first accounted for in Sec. 4.3.1, before developing the stochastic model in Sec. 4.3.2.

4.3.1 Input data processing

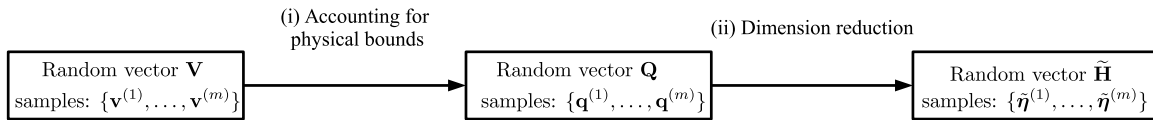


Figure 4.2: The two data processing procedures, treatment of physical bounds, and dimension reduction.

In this section, the two data processes illustrated in Fig. 4.2 are described. The first procedure introduces the random vector \mathbf{Q} which accounts for the physical bounds applied on \mathbf{V} . In the second procedure, a dimension reduction process is applied on the random vector \mathbf{Q} and the reduced dimension random vector $\tilde{\mathbf{H}}$ is obtained. These two procedures are accomplished in such a way that their inverse processes, $\tilde{\mathbf{H}} \rightarrow \mathbf{Q} \rightarrow \mathbf{V}$,

exist. As a result, the stochastic model for the random vector \mathbf{V} can be constructed indirectly through the random vector $\tilde{\mathbf{H}}$ in Sec. 4.3.2.

Introduction of the physical bounds The random vector \mathbf{V} is constrained by the physical conditions:

- (i) The 2 variables $\{\bar{e}, \bar{f}_{\max}\}$ are non-negative; and
- (ii) The distance \bar{d}_{\max} at which the apparent contact force reaches its maximum adhesive force is larger than the threshold distance \bar{d}_{limit} , see Fig. 4.1.

These two constraints have to be taken into account in the way of constructing the stochastic model to ensure consistency. Toward this end, we introduce a standardized random vector \mathbf{Q} valued in \mathfrak{R}^4 whose samples $\{\mathbf{q}^{(1)}, \dots, \mathbf{q}^{(m)}\}$ are evaluated from the parameters vectors $\{\mathbf{v}^{(1)}, \dots, \mathbf{v}^{(m)}\}$ as

$$\mathbf{q}^{(k)} = \left[\frac{\log(\bar{e}^{(k)})}{\sigma_{\log(\bar{e})}}, \frac{\log(\bar{f}_{\max}^{(k)})}{\sigma_{\log(\bar{f}_{\max})}}, \frac{\bar{d}_{\max}^{(k)}}{\sigma_{\bar{d}_{\max}}}, \frac{\log(\bar{d}_{\max}^{(k)} - \bar{d}_{\text{limit}}^{(k)})}{\sigma_{\log(\bar{d}_{\max} - \bar{d}_{\text{limit}})}} \right]^T, \quad \text{with } k = 1, \dots, m, \quad (4.7)$$

where σ_{\cdot} is the standard deviation of the random variable \cdot evaluated from m samples $\{\mathbf{v}^{(1)}, \dots, \mathbf{v}^{(m)}\}$, e.g.

$$\sigma_{\log(\bar{e})} \approx \left[\frac{\sum_{k=1}^m (\log(\bar{e}^{(k)}) - \mathbb{E}\{\log(\bar{e})\})^2}{m-1} \right]^{1/2}, \quad (4.8)$$

with

$$\mathbb{E}\{\log(\bar{e})\} \approx \frac{\sum_{k=1}^m \log(\bar{e}^{(k)})}{m}. \quad (4.9)$$

The transformation in Eq. (4.7) is bijective and its inverse is given by

$$\mathbf{v} = \left[\exp(q_1 \sigma_{\log(\bar{e})}), \exp(q_2 \sigma_{\log(\bar{f}_{\max})}), q_3 \sigma_{\bar{d}_{\max}}, q_3 \sigma_{\bar{d}_{\max}} - \exp(q_4 \sigma_{\log(\bar{d}_{\max} - \bar{d}_{\text{limit}})}) \right]^T. \quad (4.10)$$

Therefore, using the stochastic model that is developed in the next Sec. 4.3.2, one can generate realizations \mathbf{q} , from which the corresponding realizations \mathbf{v} can be evaluated using Eq. (4.10), while respecting their physical bounds. In Eq. (4.10), the superscript index $^{(k)}$ has been omitted in order to remain general which is useful for the development of the generator of the apparent contact forces discussed in the following.

Linear dimension reduction To reduce the effect of the curse of dimensionality, a linear dimension reduction process is applied before constructing the gPCE. The idea of the linear dimension reduction is to seek for a few orthogonal linear combinations of the original basis with the largest variances. In this work, the linear dimension reduction is performed using the PCA of the covariance matrix [53, 58, 37].

Using the input data of m vectors $\{\mathbf{q}^{(1)}, \dots, \mathbf{q}^{(m)}\}$ evaluated from Eq. (4.7) one can estimate their mean vector $\bar{\mathbf{q}}$ and their covariance matrix $[C_{\mathbf{Q}}]$ as

$$\bar{\mathbf{q}} \approx \frac{\sum_{k=1}^m \mathbf{q}^{(k)}}{m}, \quad [C_{\mathbf{Q}}] \approx \frac{\sum_{k=1}^m (\mathbf{q}^{(k)} - \bar{\mathbf{q}})(\mathbf{q}^{(k)} - \bar{\mathbf{q}})^T}{m-1}. \quad (4.11)$$

Applying the principal component transformation, we deduce the random vector \mathbf{H} with its realization $\boldsymbol{\eta}$ evaluated as

$$\boldsymbol{\eta}^T = (\mathbf{q} - \bar{\mathbf{q}})^T [A][\Lambda]^{-1/2}, \quad (4.12)$$

where $[A] = [\mathbf{a}_1, \dots, \mathbf{a}_4]$ is a matrix of the 4 eigenvectors of the matrix $[C_{\mathbf{Q}}]$ satisfying $[A][A]^T = I_4$ with I_4 the 4-dimensional unit vector, and $[\Lambda] = \text{diag}(\boldsymbol{\lambda})$ is a diagonal matrix of the 4 corresponding ordered eigenvalues $\lambda_1 \geq \dots \geq \lambda_4 \geq 0$. The random vector \mathbf{H} is characterized by a zero mean and identity covariance matrix, and its components are uncorrelated in the sense of covariance². The 4-dimensional random vector \mathbf{Q} can be represented by the N_g -dimensional ($N_g \leq 4$) random vector $\tilde{\mathbf{H}}$ with its realization $\tilde{\boldsymbol{\eta}}$ defined by the first N_g components of vector $\boldsymbol{\eta}$,

$$\tilde{\boldsymbol{\eta}} = \{\eta_1, \dots, \eta_{N_g}\}, \quad (4.13)$$

where N_g is the reduced dimension. That dimension reduction is obtained by the following approximation,

$$q_i \simeq \bar{q}_i + \sum_{j=1}^{N_g} \sqrt{\lambda_j} A_{ij} \eta_j, \quad \text{for } i = 1, \dots, 4. \quad (4.14)$$

The superscript "tilde" is added in the notations $\tilde{\mathbf{H}}$ ($\tilde{\boldsymbol{\eta}}$) in order to indicate the reduced dimension quantities, and to differ them from the original quantities \mathbf{H} ($\boldsymbol{\eta}$). The number of reduced dimensions N_g can be chosen in order to verify the condition

$$\text{Err}^{\text{DR}}(N_g) = \frac{\sum_{i=N_g+1}^4 \lambda_i}{\sum_{i=1}^4 \lambda_i} < \epsilon, \quad (4.15)$$

where $\epsilon \ll 1$ is the admitted error.

4.3.2 gPCE representation

4.3.2.1 Development of gPCE representation

Because the sequential transformation $\tilde{\mathbf{H}} \xrightarrow{\text{Eq. (4.14)}} \mathbf{Q} \xrightarrow{\text{Eq. (4.10)}} \mathbf{V}$ exists, the reduced dimension random vector $\tilde{\mathbf{H}}$ has the ability to represent the random vector \mathbf{V} of apparent contact force parameters. In this section, a stochastic model is constructed in order

²Uncorrelated random variables are not necessarily independent

to generate realizations of the random vector $\tilde{\mathbf{H}}$ using as input data its m explicitly evaluated samples $\{\tilde{\boldsymbol{\eta}}^{(1)}, \dots, \tilde{\boldsymbol{\eta}}^{(m)}\}$, obtained using Eqs. (4.12, 4.13). The stochastic model developed in this work is a truncated N_d -order gPCE mapping the random vector $\boldsymbol{\Xi}$, uniformly distributed in the N_g -dimensional unit cube $[0, 1]^{N_g}$, to the random vector $\tilde{\mathbf{H}}^{\text{PC}}$, which is enforced to be an approximation in terms of distribution of the objective random vector $\tilde{\mathbf{H}}$. That truncated gPCE is formulated as [39, 119, 149]

$$\underbrace{\tilde{\mathbf{H}}^{\text{PC}} = \sum_{\alpha=1}^N \mathbf{c}_\alpha \Psi_\alpha(\boldsymbol{\Xi})}_{N_d\text{-order gPCE}} \stackrel{\text{d.}}{\approx} \tilde{\mathbf{H}}, \quad (4.16)$$

where $\stackrel{\text{d.}}{\approx}$ means the approximation in terms of distribution, $\mathbf{c}_1, \dots, \mathbf{c}_N$ are N_g -dimensional vectors of coefficients to be identified, and where $\Psi_\alpha(\boldsymbol{\Xi})$ with $\{\alpha = 1, \dots, N\}$ are the renumbered orthogonal Legendre polynomials defined in $[0, 1]^{N_g}$ and whose orders are truncated by N_d . The polynomials Ψ_α are given by

$$\Psi_\alpha \in \left\{ \Psi^{(n_1, n_2, \dots, n_{N_g})} = \prod_{i=1}^{N_g} \Psi^{(n_i)}(\xi_i) : \sum_1^{N_g} n_i \leq N_d \right\}. \quad (4.17)$$

where $\Psi^{(n_i)}$ is a n_i -order Legendre polynomial defined in $[0, 1]$. The expressions of the Legendre polynomials are given in Appendix C.1 and illustrated in Fig. 4.3 for the unidimensional case. The number of polynomials Ψ_α of the truncated N_d -order gPCE is

$$N = \binom{N_d + N_g}{N_g} = (N_d + N_g)! / N_d! / N_g!. \quad (4.18)$$

These polynomials Ψ_α are $p_{\boldsymbol{\Xi}}$ -orthonormal, i.e.

$$\int_{[0,1]^{N_g}} \Psi_\alpha(\boldsymbol{\xi}) \Psi_\beta(\boldsymbol{\xi}) p_{\boldsymbol{\Xi}}(\boldsymbol{\xi}) d\boldsymbol{\xi} = \delta_{\alpha\beta}, \quad (4.19)$$

where $p_{\boldsymbol{\Xi}} = 1$ is the probabilistic density function of random vector $\boldsymbol{\Xi}$, and $\delta_{\alpha\beta}$ is the Kronecker symbol.

The coefficients $\mathbf{c}_1, \dots, \mathbf{c}_N$ are identified in order to constrain the approximation in terms of distribution as stated by Eq. (4.16). During the identification process, the distribution of the random vector $\tilde{\mathbf{H}}$ is estimated from its m explicitly evaluated samples $\{\tilde{\boldsymbol{\eta}}^{(1)}, \dots, \tilde{\boldsymbol{\eta}}^{(m)}\}$ using the multivariate kernel density estimation (MKDE) detailed in Appendix C.2. To identify the gPCE coefficients the isoprobabilistic Rosenblatt transformation is used. That transformation matches each sample of the random vector $\boldsymbol{\Xi}$ to a sample of the random vector $\tilde{\mathbf{H}}$ using CDFs [110]. The coefficients of the gPCE model are identified by projecting that transformation on the orthogonal Legendre polynomials [28]. That projection is numerically implemented using the Gauss quadrature rule at negligible computational cost for the low dimension cases.

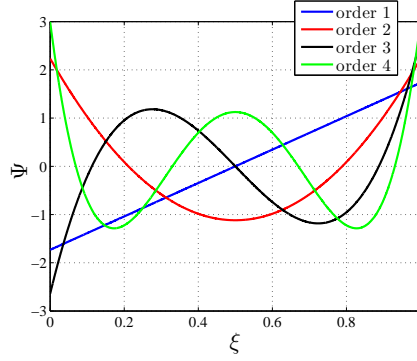


Figure 4.3: The first four Legendre polynomials.

Rosenblatt transformation The Rosenblatt transformation [110] $\Xi = \mathfrak{T}(\tilde{\mathbf{H}})$ is detailed component by component by

$$\begin{aligned}\xi_1 &= \mathbb{C}_{\tilde{\mathbf{H}}}(\eta_1), \\ \xi_2 &= \mathbb{C}_{\tilde{\mathbf{H}}}(\eta_2|\eta_1), \\ &\dots \\ \xi_{N_g} &= \mathbb{C}_{\tilde{\mathbf{H}}}(\eta_{N_g}|\eta_{N_g-1}, \dots, \eta_1),\end{aligned}\tag{4.20}$$

where $(\mathbb{C}_{\tilde{\mathbf{H}}}(\eta_i|\eta_{i-1}, \dots, \eta_1))$ $\mathbb{C}_{\tilde{\mathbf{H}}}(\eta_i)$ are the (conditional) CDFs of the random variable H_i evaluated at η_i , which are given as

$$\mathbb{C}_{\tilde{\mathbf{H}}}(\eta_i|\eta_{i-1}, \dots, \eta_1) = \int_{-\infty}^{\eta_i} p_{\tilde{\mathbf{H}}}(\eta_i = x|\eta_{i-1}, \dots, \eta_1)dx, \quad \text{with } i = 1, \dots, N_g, \tag{4.21}$$

with $(p_{\tilde{\mathbf{H}}}(\eta_i|\eta_{i-1}, \dots, \eta_1))$ $p_{\tilde{\mathbf{H}}}(\eta_i)$ the (conditional) distribution functions of the random variable H_i . These distribution functions are evaluated using the MKDE detailed in Appendix C.2. Owing to the strictly monotonic property of the CDFs, the inverse of Rosenblatt transformation,

$$\tilde{\mathbf{H}} = \mathfrak{T}^{-1}(\Xi), \tag{4.22}$$

exists and is detailed component by component as

$$\begin{aligned}\eta_1 &= \mathbb{C}_{\tilde{\mathbf{H}}}^{-1}(\xi_1), \\ \eta_2 &= \mathbb{C}_{\tilde{\mathbf{H}}}^{-1}(\xi_2|\eta_1), \\ &\dots \\ \eta_{N_g} &= \mathbb{C}_{\tilde{\mathbf{H}}}^{-1}(\xi_{N_g}|\eta_{N_g-1}, \dots, \eta_1).\end{aligned}\tag{4.23}$$

The inverse Rosenblatt transformation described in Eq. (4.22) allows generating samples of the random vector $\tilde{\mathbf{H}}$. Indeed, with this transformation, one can generate samples of a uniform distribution random vector Ξ , from which the corresponding realizations of

the random vector $\tilde{\mathbf{H}}$ are evaluated. However, evaluating the inverse Rosenblatt transformation requires a non-trivial computational effort devoted to the evaluation of the CDFs, Eq. (4.21). Therefore, to achieve the goal of negligible computational cost when evaluating the stochastic model, the inverse Rosenblatt transformation in Eq. (4.22) is approximated using gPCE model in Eq. (4.16) as

$$\underbrace{\tilde{\mathbf{H}} = \mathfrak{T}^{-1}(\Xi)}_{\text{Rosenblatt transformation}} \approx \underbrace{\tilde{\mathbf{H}}^{\text{PC}} = \sum_{\alpha=1}^N \mathbf{c}_\alpha \Psi_\alpha(\Xi)}_{N_d\text{-order gPCE}}. \quad (4.24)$$

Identification of the gPCE coefficients Thanks to the p_Ξ -orthonormal property of the polynomial chaos system stated in Eq. (4.19), the coefficients \mathbf{c}_α can be evaluated by projecting Eq. (4.24) on the polynomial chaos system [28], leading to

$$\mathbf{c}_\alpha = \int_{[0,1]^{N_g}} \mathfrak{T}^{-1}(\boldsymbol{\xi}) \Psi_\alpha(\boldsymbol{\xi}) d\boldsymbol{\xi}. \quad (4.25)$$

In particular, Eq. (4.25) is detailed component by component as

$$\begin{aligned} c_{\alpha_1} &= \int_{[0,1]} \mathbb{C}_{\tilde{\mathbf{H}}}^{-1}(\xi_1) \Psi_\alpha(\xi_1) d\xi_1, \\ c_{\alpha_2} &= \int_{[0,1]^2} \mathbb{C}_{\tilde{\mathbf{H}}}^{-1}(\xi_2|\xi_1) \Psi_\alpha(\xi_1, \xi_2) d\xi_1 d\xi_2, \\ &\dots \\ c_{\alpha_{N_g}} &= \int_{[0,1]^{N_g}} \mathbb{C}_{\tilde{\mathbf{H}}}^{-1}(\xi_{N_g}|\xi_1, \xi_2, \dots, \xi_{N_g-1}) \Psi_\alpha(\xi_1, \xi_2, \dots, \xi_{N_g}) d\xi_1 d\xi_2 \dots d\xi_{N_g}, \end{aligned} \quad (4.26)$$

where $\Psi_\alpha(\xi_1, \dots, \xi_i)$ with $i \leq N_g$ is defined as

$$\Psi_\alpha(\xi_1, \dots, \xi_i) = \int_{[0,1]^{N_g-i}} \Psi_\alpha(\boldsymbol{\xi}) d\xi_{i+1} \dots d\xi_{N_g}. \quad (4.27)$$

Due to the p_Ξ -orthonormal properties, see Eq. (4.19), we have

$$\Psi^{(n_1, n_2, \dots, n_{N_g})}(\xi_1, \dots, \xi_i) = \begin{cases} 0 & \text{if } \exists k > i : n_k \neq 0, \\ \Psi^{(n_1, n_2, \dots, n_i)}(\xi_1, \dots, \xi_i), & \text{if } n_k = 0 \forall k > i. \end{cases} \quad (4.28)$$

4.3.2.2 Numerical implementation

Numerical evaluation of the gPCE coefficient In terms of numerical implementation, the integration in Eq. (4.26) is efficiently evaluated using quadrature rules [148]. Indeed, using the Gauss quadrature rule [1], the $N_d + 1$ integral points t_i with $i = 1, \dots, N_d + 1$ are identified from the integration support $[0, 1]$, and associated with

the weights w_i such that $\sum_{i=1}^{N_d+1} w_i = 1$. The coefficients of the gPCE are evaluated by applying a Gauss quadrature rule on Eq (4.26), leading to

$$\begin{aligned}
 c_{\alpha_1} &\simeq \sum_{i=1}^{N_d+1} \widehat{\mathbb{C}}_{\tilde{\mathbf{H}}}^{-1}(\xi_1 = t_i) \Psi_{\alpha}(\xi_1 = t_i) w_i, \\
 c_{\alpha_2} &\simeq \sum_{i=1}^{N_d+1} \sum_{j=1}^{N_d+1} \widehat{\mathbb{C}}_{\tilde{\mathbf{H}}}^{-1}(\xi_2 = t_i | \xi_1 = t_j) \Psi_{\alpha}(\xi_1 = t_i, \xi_2 = t_j) w_i w_j, \\
 &\dots \\
 c_{\alpha_{N_g}} &\simeq \sum_{i=1}^{N_d+1} \sum_{j=1}^{N_d+1} \dots \sum_{k=1}^{N_d+1} \widehat{\mathbb{C}}_{\tilde{\mathbf{H}}}^{-1}(\xi_{N_g} = t_k | \xi_1 = t_i, \xi_2 = t_j, \dots) \times \\
 &\quad \Psi_{\alpha}(\xi_1 = t_i, \xi_2 = t_j, \dots, \xi_{N_g} = t_k) w_i w_j \dots w_k,
 \end{aligned} \tag{4.29}$$

where $\widehat{\mathbb{C}}_{\tilde{\mathbf{H}}}$ are the approximations of the CDFs obtained using MKDE discussed in Appendix C.2. To evaluate Eq. (4.29), the values of inverse CDFs are obtained using the linear interpolation technique on the approximated CDFs [28], see Appendix C.2 for details. Note that the total number of integral points, i.e. $\mathcal{O}((N_d + 1)^{N_g} \times N)$, increases exponentially with the reduced dimension number N_g . Therefore, the method is confirmed to be efficient in terms computational cost only when N_g remains small. This is the reason for the requirement of the dimension reduction process.

Error estimation The order N_d of the gPCE representation is crucial to enhance the approximation stated in Eq. (4.24). To quantify that approximation, the mean integral square errors are evaluated as [148]

$$\text{relMISE}_i^{\text{PC}}(N_d) = \frac{\int_{[0,1]} (\widehat{\mathfrak{T}}_i^{-1}(\boldsymbol{\xi}) - \sum_{\alpha=1}^N c_{\alpha_i} \Psi_{\alpha}(\boldsymbol{\xi}))^2 d\boldsymbol{\xi}}{\int_{[0,1]} (\widehat{\mathfrak{T}}_i^{-1}(\boldsymbol{\xi}))^2 d\boldsymbol{\xi}}, \quad \text{with } i = 1..N_g; \tag{4.30}$$

$$\text{relMISE}^{\text{PC}}(N_d) = \frac{\int_{[0,1]^{N_g}} \|\widehat{\mathfrak{T}}^{-1}(\boldsymbol{\xi}) - \sum_{\alpha=1}^N \mathbf{c}_{\alpha} \Psi_{\alpha}(\boldsymbol{\xi})\|^2 d\boldsymbol{\xi}}{\int_{[0,1]^{N_g}} \|\widehat{\mathfrak{T}}^{-1}(\boldsymbol{\xi})\|^2 d\boldsymbol{\xi}}. \tag{4.31}$$

where $\widehat{\mathfrak{T}}$ is the approximation of \mathfrak{T} obtained using MKDE as discussed previously. The errors $\text{relMISE}_i^{\text{PC}}$ and $\text{relMISE}^{\text{PC}}$ are also evaluated using a Gauss quadrature rule.

4.4 Applications

The stochastic models of the random apparent adhesive contact forces are developed using the input data sets of m explicitly evaluated apparent adhesive contact forces obtained in Sec. 3.5. The five surface pairs described in Tab. 3.4 are considered. The

value of m is identified by a convergence analysis when estimating the probability distribution of the apparent adhesive contact forces, as it is illustrated in Fig. 4.4 for the case of apparent adhesion energy \bar{e} . It is observed that with the choice of $m = 5000$ the convergence is reached. Using the parametrization process described in Sec. 4.2, the

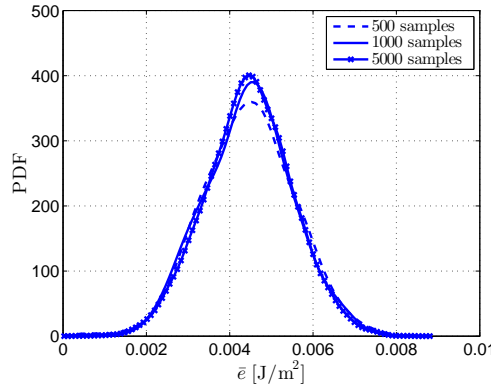


Figure 4.4: The convergence with respect to m when approximating the probability density function of the apparent adhesion energy \bar{e} . The illustrated case corresponds to pair b at $RH = 0.65\%$.

data set is represented by $m = 5000$ samples $\{\mathbf{v}^{(1)}, \dots, \mathbf{v}^{(m)}\}$ of the random parameters vector \mathbf{V} . The stochastic model of the random vector \mathbf{V} is constructed from those m input samples and following the two processes – input data processing and gPCE representation – described in Sec. 4.3. The generated forces using the constructed stochastic model are then compared with the explicitly evaluated ones.

4.4.1 Identification of the reduced dimensions number N_g

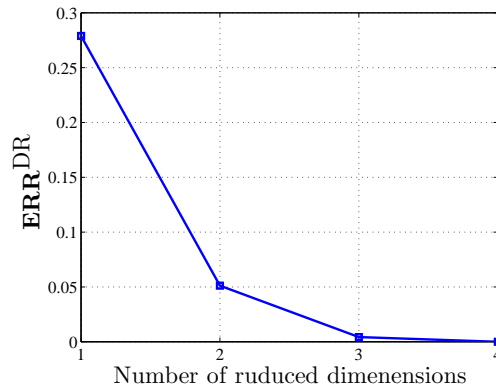


Figure 4.5: The error due to the dimension reduction process Err^{DR} . The illustrated case corresponds to pair b at $RH = 0.65\%$.

To lower the effect of the curse of dimensionality, the linear dimension reduction reported in Section 4.3.1 is applied. From the input data set $\{\mathbf{v}^{(1)}, \dots, \mathbf{v}^{(m)}\}$ with $m = 5000$, the corresponding samples $\{\mathbf{q}^{(1)}, \dots, \mathbf{q}^{(m)}\}$ of the random vector \mathbf{Q} are evaluated by Eq. (4.7). Using the principal component transformation given by Eq. (4.12), the m samples $\{\boldsymbol{\eta}^{(1)}, \dots, \boldsymbol{\eta}^{(m)}\}$ of the orthogonal random vector \mathbf{H} can be obtained. The dimension reduction error Err^{DR} can then be evaluated using Eq. (4.15) and is illustrated in Fig. 4.5. These numerical results of the error Err^{DR} suggest that the number of reduced dimensions can be chosen as $N_g = 3$ with the corresponding error $\text{Err}^{\text{DR}} = 0.005$. Although there is only one dimension less, the number of the coefficients of gPCE model is lowered by $(N_d + 4)/4$ times, e.g. $(N_d + 4)/4 = 4$ for $N_d = 12$, which justifies the process. From m samples $\{\boldsymbol{\eta}^{(1)}, \dots, \boldsymbol{\eta}^{(m)}\}$, the corresponding reduced dimension vectors $\{\tilde{\boldsymbol{\eta}}^{(1)}, \dots, \tilde{\boldsymbol{\eta}}^{(m)}\}$ are obtained as $\tilde{\boldsymbol{\eta}}^{(k)} = \{\eta_1^{(k)}, \eta_2^{(k)}, \eta_3^{(k)}\}$ with $k = 1, \dots, m$.

4.4.2 Construction of the gPCE representation

To identify the coefficients of the gPCE model, see Eq. (4.16) for the compact form and Eq. (4.24) for the detailed form, the inverse Rosenblatt transformation is projected on the polynomial chaos system, Eq. (4.26). The integrations in Eq. (4.26) are efficiently achieved using a Gauss quadrature rule, see Eq. (4.29). With the input of $m = 5000$ reduced dimension vectors $\{\tilde{\boldsymbol{\eta}}^{(1)}, \dots, \tilde{\boldsymbol{\eta}}^{(m)}\}$, one can access to the approximations of the probability density function owing to the MKDE method, the CDFs, and the inverse CDFs, see Appendix C.2.

To study the convergence of the gPCE model in terms of the truncated order of the gPCE model N_d , we can consider three aspects: (i) the comparison in terms of distributions between the two random vectors $\tilde{\mathbf{H}}$ and $\tilde{\mathbf{H}}^{\text{PC}}$, see Fig. 4.6, (ii) the mean square integral errors defined in Eqs. (4.30-4.31), see Fig. 4.7(a); and (iii) the comparison of gPCE model and Rosenblatt transformation, Eq. (4.24), see Figs. 4.7(b, c) for $\{\boldsymbol{\tau}_1^{-1}, \boldsymbol{\tau}_2^{-1}\}$. As it can be observed from Figs. 4.6 and 4.7, the constructed 12-order gPCE model can approximate the randomness of the reduced dimension random vector \mathbf{H} within an error $\text{relMISE}^{\text{PC}}(N_d = 12) = 5\%$.

4.4.3 Results

The generated samples of the random apparent contact forces are compared in Figs. 4.8 and 4.9 with their explicitly evaluated ones obtained in Sec. 3.5 for the five considered surface pairs described in Tab. 3.4. The comparisons in terms of the distribution of parameters, \bar{f}_{max} , \bar{e} , \bar{d}_{max} , and \bar{d}_{limit} are illustrated in Fig. 4.10. These comparisons show that the randomness of apparent contact forces is well approximated by the stochastic model.

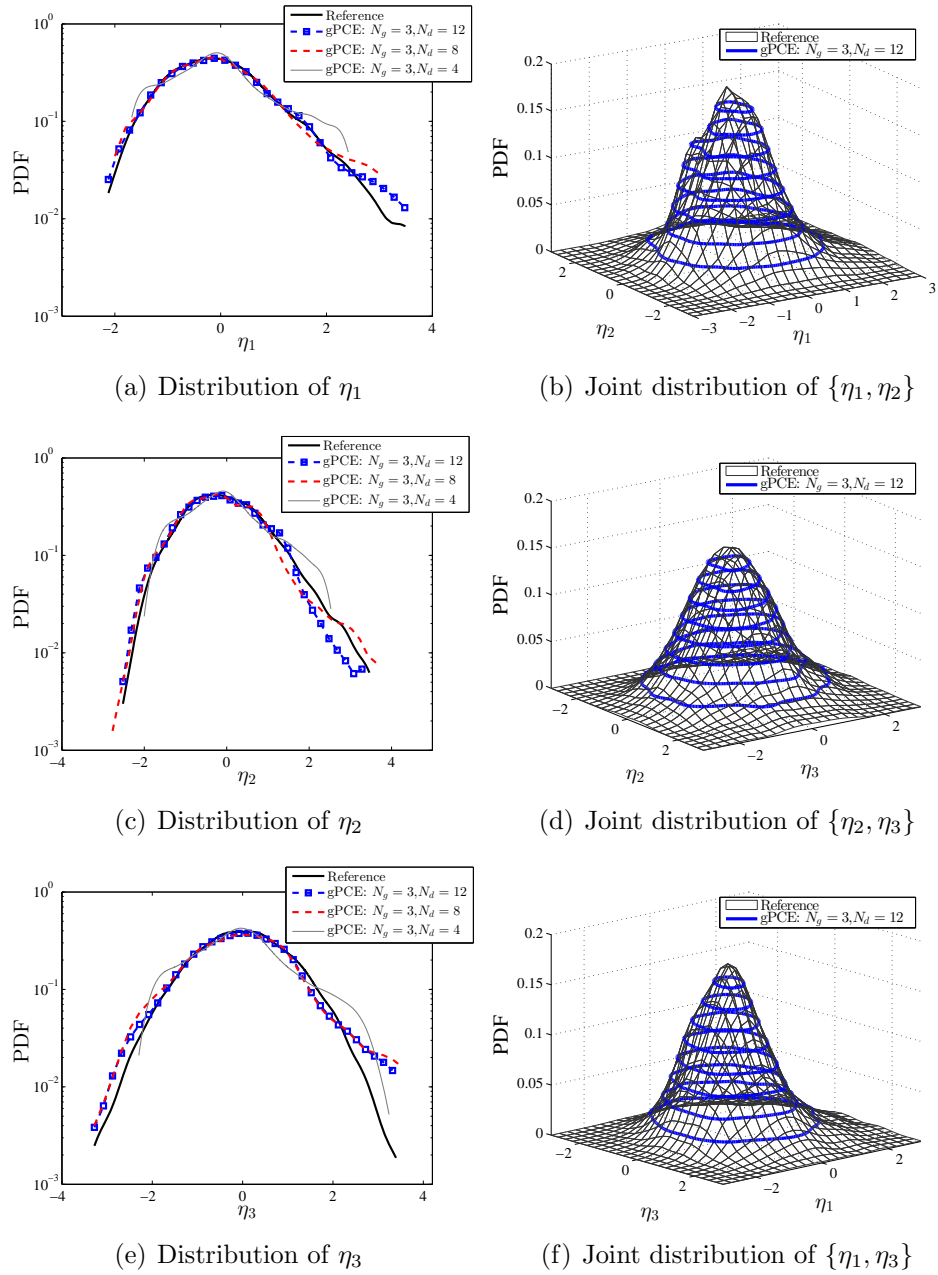


Figure 4.6: The convergence analysis of gPCE model described by Eq. (4.16) in terms of the order N_d . The figures illustrate the comparisons in terms of the probability distributions (a, b, c) and the joint bivariate distributions (d, e, f), between the random vector $\tilde{\mathbf{H}}^{\text{PC}}$ evaluated using gPCE models with different values of N_d and the reference ones obtained from m explicitly evaluated contact forces. The illustrated case is pair b at $RH = 65\%$.

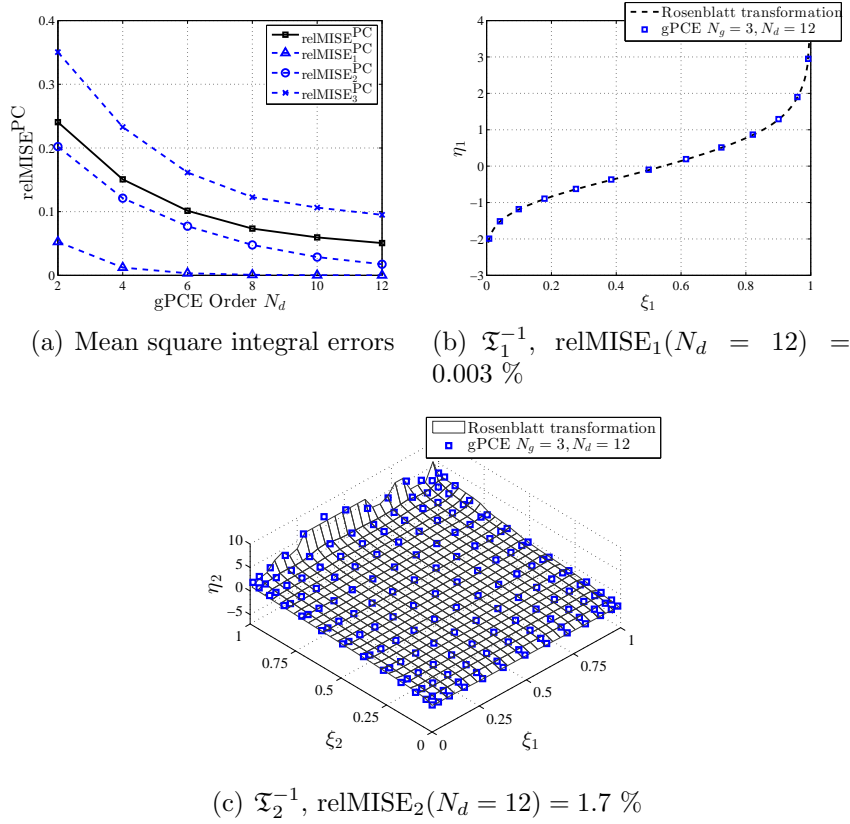


Figure 4.7: The convergence analysis of gPCE model in terms of the order N_d . (a) The mean square integral error defined in Eqs. (4.30-4.31). (b, c) The comparisons between the Rosenblatt transformation and the gPCE model. The illustrated case is pair b at $RH = 65 \%$.

4.5 Conclusion

A stochastic model of the apparent adhesive contact forces was developed in this chapter. First, a parameterization process was applied on the contact force vs. distance curve. A gPCE model was then constructed to represent the randomness of the parameters vectors obtained from the parameterization process. The gPCE coefficients were identified in an efficient way by projecting the isoprobabilistic transformation on the polynomial systems. The Gauss quadrature rule was applied to implement the projection integration.

The stochastic models were constructed for the five considered applications and for different humidity levels, and were shown to be accurate in representing the explicitly evaluated apparent contact forces with their uncertainty. The generated samples of these forces using the stochastic models will be integrated in the next chapter as random contact laws into the structural models to evaluate probabilistic structural behaviors subjected to adhesion.

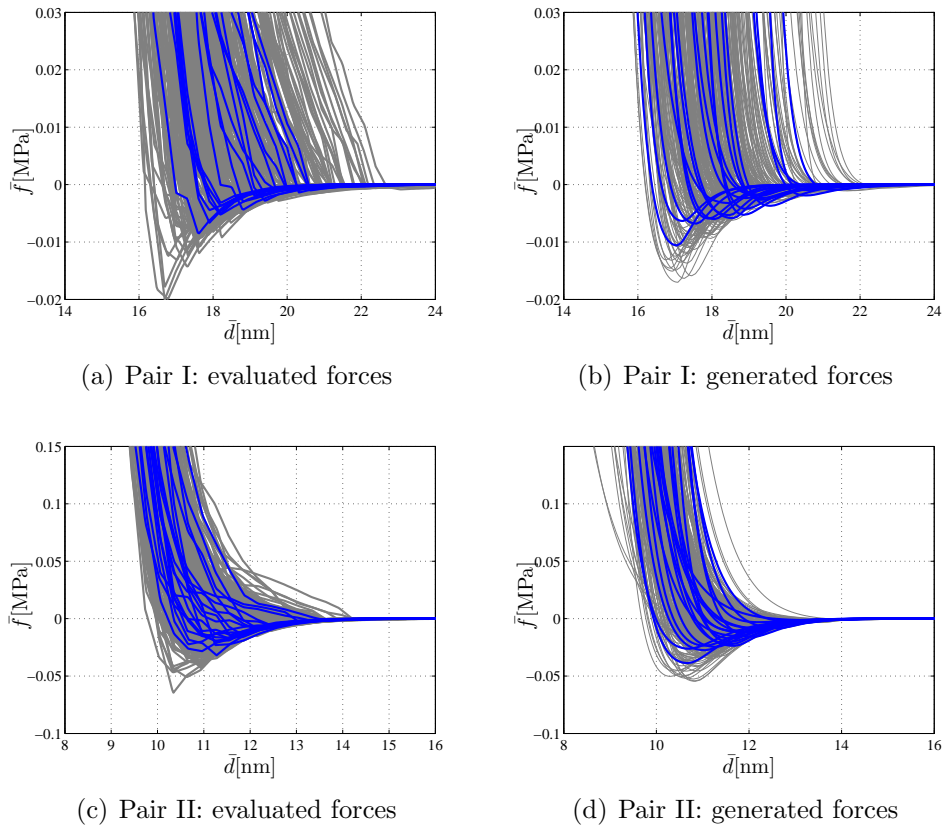


Figure 4.8: Comparison between the apparent contact forces explicitly evaluated (a, c) (copied from Figs. 3.7(e) and 3.8(e)), and the generated ones using their corresponding stochastic models (b, d). The illustrated cases are pair I (first row), and pair II (second row) at $RH = 70\%$. For each figure, 20 realizations are highlighted out of the 200 ones.

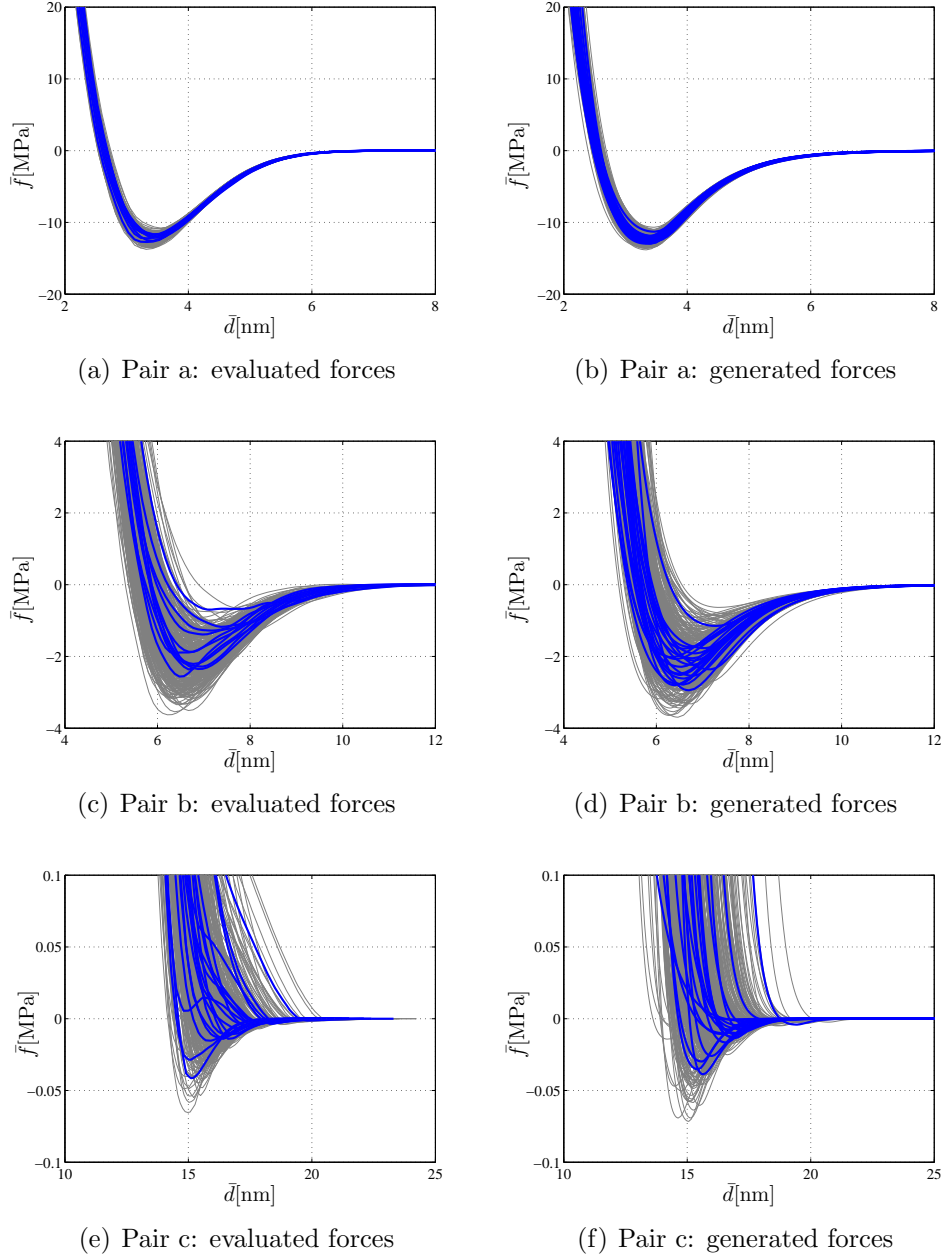


Figure 4.9: Comparison between the apparent contact forces explicitly evaluated (a, c, e) (copied from Fig. 3.10), and the generated ones using their corresponding stochastic models (b, d, f). The illustrated cases are pair a (first row), pair b (second row), and pair c (third row) at $RH = 65\%$. For each figure, 20 realizations are highlighted out of the 200 ones.

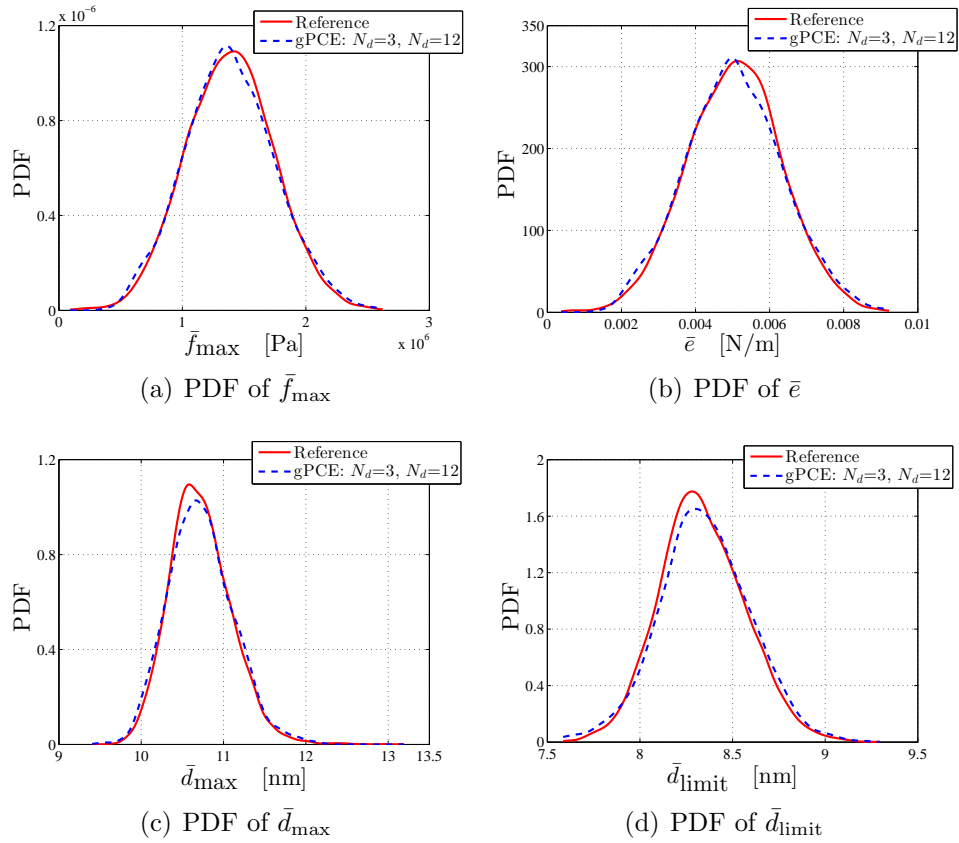


Figure 4.10: The comparison between the distributions of the random vector \mathbf{V}^{PC} generated by the gPCE model and the references obtained from the m explicitly evaluated contact forces. The illustrated case is pair b at $RH = 65\%$.

Chapter 5

Uncertainty quantification of microstructures subjected to adhesive contact

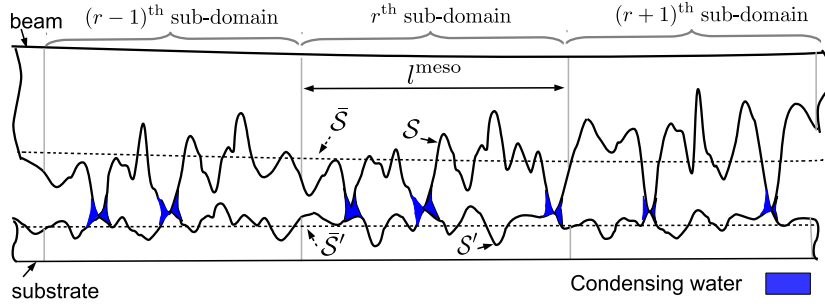
5.1 Introduction

To evaluate the behavior of micro-structures subjected to adhesive contact, a multiscale model is developed in this chapter. For the deterministic cases, the requirement for developing such a model is the scale separation such that

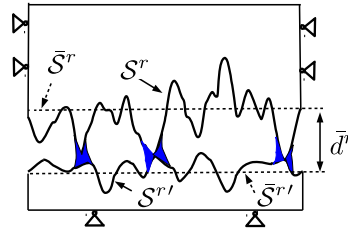
$$l^M \gg l^{\text{meso}} \text{ and } l^{\text{meso}} \gg l^m, \quad (5.1)$$

where $l^M \sim \mathcal{O}(100 \mu\text{m})$ is the characteristic length of the micro-structures, $l^m \sim \mathcal{O}(0.3 \mu\text{m})$ is the characteristic length of the random surface, i.e. the correlation length of surface topology, see Figs. 2.5 and 2.15, and l^{meso} is the characteristic length of the rough contacting surfaces on which the meso-scale apparent adhesive contact behaviors are evaluated. When the first condition is satisfied, one can divide the contact zone into smaller contact sub-domains with size $l_1^{\text{meso}} \times l_2^{\text{meso}}$ at which the variation of the structural displacement is negligible compared to the surface roughness¹, see Fig. 5.1(a). The structural behavior is evaluated by applying the semi-analytical contact model, developed in Chapter 3, to evaluate the apparent adhesive contact forces in each contact sub-domain, see Fig. 5.1(b), and then integrating them as contact laws into the upper-scale model of the considered structure, see Fig. 5.1(c). Due to the reduced size of MEMS l^M , to verify the condition $l^{\text{meso}} \ll l^M$, $l^{\text{meso}} \sim \mathcal{O}(1 \mu\text{m})$. As a result, the scale separation $l^{\text{meso}} \gg l^m$ cannot be fulfilled simultaneously, and the meso-scale problem is not statistically representative. Moreover, since the contact area might be much smaller than the apparent one, the apparent adhesive contact forces suffer from a scatter, as observed in Chapter 3. The uncertainties associated with these contact forces are propagated in order to evaluate the probabilistic behavior of the considered

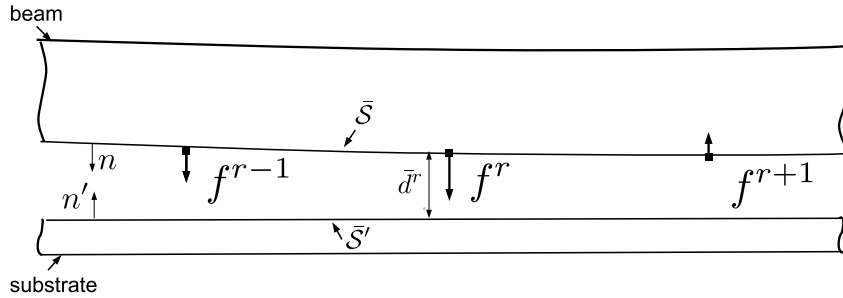
¹For a conventional choice of 2D contact model, $l_1^{\text{meso}} = l_2^{\text{meso}} = l^{\text{meso}}$.



(a) Original problem (not on scale).



(b) Meso-scale contact problem for r -th sub-domain (not on scale).



(c) Approximated problem using multiscale technique (not on scale).

Figure 5.1: The multiscale model of the adhesive contact problem applied for micro beams. (a) The original contact problem between the rough surfaces of beam and substrate. (b) The meso-scale contact problem used to evaluate the r^{th} apparent adhesive contact forces. (c) The approximated problem at the structural scale using a multiscale technique in which the contact forces are evaluated from the meso-scale contact problem in (b).

structure. This task is carried out by performing a MCS on the constructed multiscale model using the apparent adhesive contact forces which are either explicitly evaluated as in Chapter 3 – the direct MCS approach, or generated using the stochastic model developed in Chapter 4 – the stochastic model-based MCS approach. These approaches are sketched in Fig. 1.5.

In this chapter, the multiscale model is first developed in Sec. 5.2. The two approaches, i.e. direct MCS and stochastic model-based MCS, are then performed on the multiscale model for the studied interacting surface pairs summarized in Tab. 3.4. The predictions obtained by the two approaches are compared to verify the stochastic model-based approach in Sec. 5.3. The comparison in terms of computational cost is also described to evaluate the efficiency of the stochastic-model based method. The numerical predictions are then compared with the experimental results in Sec. 5.4. Based on the comparisons, the uncertainty of the structural behaviors, the effects of the non-Gaussian probability distribution of the contacting surface heights, and the validation of the developed method, are reviewed. In addition, by relying on the numerical model, the uncertainty of the structural behaviors due to different sources, i.e. from the rough contacting surfaces and from the uncertain geometrical dimensions, are compared.

5.2 Stochastic multiscale scheme for adhesive contact problems

The contact problem is described as the contact between two bodies \mathcal{B} and \mathcal{B}' on which the contact interaction is defined between the rough surfaces $\mathcal{S}(\theta)$ and $\mathcal{S}'(\theta)$ belonging to \mathcal{B} and \mathcal{B}' respectively. In this work, \mathcal{S} and \mathcal{S}' are assumed to be nominally flat. Let us define $\bar{\mathcal{S}}$ and $\bar{\mathcal{S}'}$ the mean surfaces of the random surfaces $\mathcal{S}(\theta)$ and $\mathcal{S}'(\theta)$ respectively. Thanks to the scale separation $l^m \ll l^M$, these random surfaces are modeled as

$$\begin{aligned}\mathbf{x}_{\mathcal{S}}(l_1, l_2, \theta) &= \mathbf{x}_{\bar{\mathcal{S}}}(l_1, l_2) + z(l_1, l_2, \theta)\mathbf{n}(l_1, l_2), \\ \mathbf{x}_{\mathcal{S}'}(l_1, l_2, \theta) &= \mathbf{x}_{\bar{\mathcal{S}'}}(l_1, l_2) + z'(l_1, l_2, \theta)\mathbf{n}'(l_1, l_2),\end{aligned}\tag{5.2}$$

where $\mathbf{x}_{\mathcal{S}}$, $\mathbf{x}_{\bar{\mathcal{S}}}$, $\mathbf{x}_{\mathcal{S}'}$, $\mathbf{x}_{\bar{\mathcal{S}'}}$ are the coordinates of the points of the surfaces \mathcal{S} , $\bar{\mathcal{S}}$, \mathcal{S}' and $\bar{\mathcal{S}'}$, respectively, $\tilde{z}(\theta)$, $\tilde{z}'(\theta)$ are the independently generated surfaces heights using the generator developed in Chapter 2, \mathbf{n} , \mathbf{n}' are the outward unit normal vectors, here constant, belonging to $\bar{\mathcal{S}}$, $\bar{\mathcal{S}'}$ respectively, and l_1, l_2 are the local Cartesian coordinates.

Applying a multiscale approach, the original problem is substituted by an approximated one in which the contact boundary, defined by the rough surfaces \mathcal{S} and \mathcal{S}' , are redefined at the upper-scale by their mean surfaces $\bar{\mathcal{S}}$ and $\bar{\mathcal{S}'}$ respectively, and the apparent adhesive contact forces are associated to that boundary as contact laws, to represent the lower-scale interaction, see Fig. 5.1. In this work, one body is assumed to be rigid. For example, in the case of micro beams, see Fig. 1.3(a), the bending stiffness of the beam is much smaller than the stiffness of the substrate due to its reduced moment area². The upper-scale scale problem is then efficiently solved by a FE model of a beam interacting with a rigid plane.

The integration of these apparent adhesive contact forces into the FE model is numerically implemented in such a way that each integral point, used to evaluate the

²Note that this assumption is not applied at the lower-scale when evaluating the apparent adhesive contact forces as both contact bodies are deformable, see details in Chapter 3.

equivalent nodal forces and located on $\bar{\mathcal{S}}$, is associated with an apparent adhesive contact force. Because these contact forces are random, as observed in Sec. 3.5, different integral points are randomly associated with different contact forces. In this section, the probabilistic multiscale FE model is developed using the random apparent contact forces as the scales bridge and the energy consistency condition to derive the expression of the homogenized contact law.

5.2.1 Upper-scale governing equation

The governing equation of the contact problem at the structural scale in the case of small deformation, small strain, and zero volume force, is given by

$$\nabla \cdot \boldsymbol{\sigma} = 0 \text{ in } \mathcal{B}. \quad (5.3)$$

The body is subjected to the conventional boundary conditions

$$\begin{aligned} \boldsymbol{\sigma} \cdot \mathbf{n} &= \mathbf{f}^a \text{ on } \partial\mathcal{B}_a, \\ \mathbf{u} &= 0 \text{ on } \partial\mathcal{B}_u, \end{aligned} \quad (5.4)$$

and to the normal adhesive contact boundary as

$$\boldsymbol{\sigma} \cdot \mathbf{n} = f(\theta, \mathbf{u}_{\bar{\mathcal{S}}})\mathbf{n} \text{ on } \bar{\mathcal{S}}, \quad (5.5)$$

where \mathbf{u} is the displacement vector, $\boldsymbol{\sigma}$ is the Cauchy stress tensor, \mathbf{f}^a is the applied forces on the boundary $\partial\mathcal{B}_a$, $\partial\mathcal{B}_u$ is the boundary of the prescribed displacement, \mathbf{n} is the outward unit normal vector, $\mathbf{u}_{\bar{\mathcal{S}}}$ is the displacement vector of the contact boundary $\bar{\mathcal{S}}$, and f is the normal homogenized adhesive contact forces applied on the contact boundary $\bar{\mathcal{S}}$. The homogenized contact force f represents the lower-scale rough surface adhesive contact evaluated from the surface samples $\mathcal{S}(\theta)$ and $\mathcal{S}'(\theta)$. Its value depends on the contact configuration derived by the displacement of $\bar{\mathcal{S}}$, $\mathbf{u}_{\bar{\mathcal{S}}}$. The weak formulation of the governing equation described in Eq. (5.3) is given by

$$\begin{aligned} \int_{\mathcal{B}} \boldsymbol{\sigma} : \delta\boldsymbol{\epsilon} \, d\mathcal{B} &= \int_{\partial\mathcal{B}_a} \mathbf{f}^a \cdot \delta\mathbf{u} \, d\partial\mathcal{B}_a + \int_{\bar{\mathcal{S}}} [f(\theta, \mathbf{u}_{\bar{\mathcal{S}}})\mathbf{n}] \cdot \delta\mathbf{u}_{\bar{\mathcal{S}}} \, d\bar{\mathcal{S}}, \\ &\forall \delta\mathbf{u} \text{ kinematically admissible,} \end{aligned} \quad (5.6)$$

where $\boldsymbol{\epsilon}$ is the infinitesimal strain tensor evaluated as $\boldsymbol{\epsilon} = \frac{1}{2}(\nabla\mathbf{u} + (\nabla\mathbf{u})^T)$. To derive the expression of the contact force f , we focus in the next section on the second term of the right hand side of Eq. (5.6), which corresponds to the virtual external work δW^c ,

$$\delta W^c = \int_{\bar{\mathcal{S}}} [f(\theta, \mathbf{u}_{\bar{\mathcal{S}}})\mathbf{n}] \cdot \delta\mathbf{u}_{\bar{\mathcal{S}}} \, d\bar{\mathcal{S}}. \quad (5.7)$$

5.2.2 Expression of the homogenized contact force f

Let $\mathbf{x}^r \in \bar{\mathcal{S}}$, with $r = 1, \dots, N_p$, be the N_p integral points located on the mean surface $\bar{\mathcal{S}}$ of the upper-scale numerical model. These integral points are used to evaluate the virtual external work of the contact forces, Eq. (5.7). Each integral point is associated with a contact sub-domain which involves a part, \mathcal{S}^r , of the rough surface \mathcal{S} with size $l_1^{\text{meso}} \times l_2^{\text{meso}}$ and centered at \mathbf{x}^r . Using the assumption that \mathcal{S} and \mathcal{S}' are nominal flat, we can identify the interacting surfaces \mathcal{S}'' of \mathcal{S}^r with a similar process. As discussed previously, since $l^{\text{meso}} \ll l^{\text{M}}$, the variation of the displacement $\bar{u}_{\bar{\mathcal{S}}^r}$ of the mean surface $\bar{\mathcal{S}}^r$ is negligible in comparison with the roughness of the surfaces, see analyses in Section 5.3.1. With that assumption, let us define \bar{d}^r the normal distance from the mean surface $\bar{\mathcal{S}}^r$ to the encountered mean surface $\bar{\mathcal{S}}''$.

In the upper-scale model, the homogenized contact force f at \mathbf{x}^r is required to represent the interaction between \mathcal{S}^r and \mathcal{S}'' . The energy consistency requirement is stated as

$$[f(\mathbf{x}^r)\mathbf{n}] \cdot \delta \mathbf{u}_{\bar{\mathcal{S}}}(\mathbf{x}^r) = \frac{1}{A_{\bar{\mathcal{S}}^r}} \int_{\mathcal{S}^r(\theta)} f^{\text{m}}(\bar{d}^r, \theta) \delta \bar{d}^r d\mathcal{S}, \quad \text{with } r = 1, \dots, N_p, \quad (5.8)$$

where f^{m} is the lower-scale normal contact force resulting from the adhesive interaction between \mathcal{S}^r and \mathcal{S}'' , and $A_{\bar{\mathcal{S}}^r} = l_1^{\text{meso}} \times l_2^{\text{meso}}$. Since on the meso-scale contact problem, the displacement of the mean surface is uniform and constrained to be $\delta \bar{d}^r = -\mathbf{n} \cdot \delta \mathbf{u}_{\bar{\mathcal{S}}}$, this last relation (5.8) yields the definition of homogenized forces

$$f(\mathbf{x}^r) := -\bar{f}^r = -\frac{1}{A_{\bar{\mathcal{S}}^r}} \int_{\mathcal{S}^r(\theta)} f^{\text{m}}(\bar{d}^r, \theta) d\mathcal{S}, \quad \text{with } r = 1, \dots, N_p, \quad (5.9)$$

which corresponds to the meso-scale apparent adhesive contact forces evaluated in Chapter 3, with a change of sign to be compatible with the boundary condition stated in Eq. (5.5).

5.2.3 Stochastic FE model involving adhesive contact

Applying the FE method [158], the displacement field is approximated by

$$\mathbf{u}(\mathbf{x}) \approx \mathbf{u}^h(\mathbf{x}) = \{\Psi^{\text{FE}}(\mathbf{x})\}^T \{\mathbf{u}\}, \quad (5.10)$$

where $\{\Psi^{\text{FE}}(\mathbf{x})\}$ is a matrix assembling the FE shape functions, and $\{\mathbf{u}\}$ is a vector assembling the nodal displacements. Using the weak formulation stated in Eq. (5.6) with the upper-scale contact forces given by Eq. (5.9), the structural behaviors can be identified by solving the FE model equations

$$[K]\{\mathbf{u}(\theta)\} = \{\mathbf{f}^c(\mathbf{u}^h, \theta)\} + \{\mathbf{f}^a\}, \quad (5.11)$$

where $[K]$ is stiffness matrix constructed from the element stiffness matrices, see e.g. Appendix D.1 for the case of Euler-Bernoulli beam theory, $\{\mathbf{f}^a\}$ is the vector assembling

the equivalent nodal applied forces, and \mathbf{f}^c is the vector assembling the equivalent nodal contact forces resulting from the homogenized contact theory defined in Eq. (5.9). The problem is non-linear because the nodal forces $\{\mathbf{f}^c\}$ depend on the actual configuration $\{\mathbf{u}\}$.

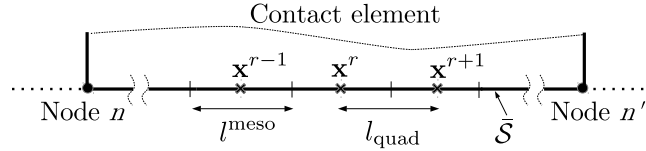


Figure 5.2: Rectangular 1D contact element with equally spaced integral points \mathbf{x}^r used to evaluate the nodal contact forces.

In order to evaluate the nodal contact forces $\{\mathbf{f}^c\}$ corresponding to a realization of random surfaces $\mathcal{S}(\theta)$ and $\mathcal{S}'(\theta)$, this work has recourse to the rectangular type quadrature rule in which the integral points are equally spaced with a distance l^{quad} chosen to be equal to the meso-scale length, $l^{\text{quad}} = l^{\text{meso}}$, see e.g. Fig. 5.2. The nodal forces, $\mathbf{f}^{c,n}$, at a node n belonging to the mean surfaces $\bar{\mathcal{S}}$ are computed by applying the FE discretization on the homogenized contact force defined in Eq. (5.9), leading to

$$\mathbf{f}^{c,n}(\mathbf{u}^h, \theta) = - \sum_{r=1}^{N_p} \bar{f}^r(\bar{d}^r, \theta) \Psi^{\text{FE},n}(\mathbf{x}^r) \mathbf{n}(\mathbf{x}^r) A_{\bar{\mathcal{S}}^r}. \quad (5.12)$$

The contact distance \bar{d}^r is defined based on the actual configuration of $\bar{\mathcal{S}}^r$, and consequently depends on \mathbf{u}^h . Therefore, the problem stated by Eq. (5.11) is non-linear. To deal with the non-linearity, the Newton-Raphson method is applied.

Remark: The multiscale framework is developed for the following cases: the mean surfaces of the contacting rough surfaces are non-parallel, however at the meso-scale size $l_1^{\text{meso}} \times l_2^{\text{meso}}$, the variation of the distances between the mean surfaces is much smaller than the considered roughness. For a completeness, in the following, two scenarios in which that assumption is not valid are discussed. (a) When the non-parallel degree at the meso-scale is comparable with or larger than the ratio between the considered roughness and the meso-scale length, the multiscale method should be modified to account for the lack of parallelism. For instance, when evaluating the meso-scale apparent contact forces, in addition to the contact distance \bar{d}^r and the uncertainty parameter θ , other parameters such as the surfaces interaction angle can be added. In this case, the meso-scale contact forces are evaluated for non-parallel mean surfaces according to the values of these additional parameters. (b) When the structural contact geometries are not between two nominal parallel surfaces anymore, e.g. between an edge of a triangular prism and a surface, the multiscale approach is adapted by changing the notion of the mean surface $\bar{\mathcal{S}}$ by the successive interactions of two non-parallel surfaces couples. For the sake of simplification when evaluating the apparent contact forces and when developing the

stochastic method, we assume that the surfaces are nominally parallel, the cases (a) and (b) being beyond the scope of this work.

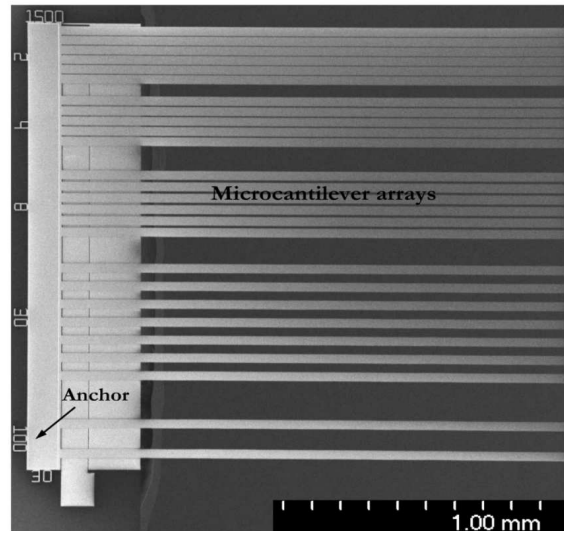
5.2.4 Resolution method

To solve the upper-scale governing equation, Eq. (5.11), two methods were developed, the direct MCS approach and the stochastic model-based approach, see Fig. 1.5 for their flow charts.

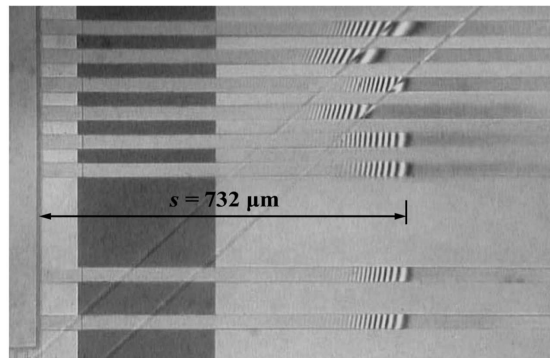
When using direct MCS approach, N_{MC} surface pairs with random heights, $z(\theta)$ and $z'(\theta)$, are generated with a size equivalent to the size of \mathcal{S} . Each surfaces pair is then divided into N_P contact sub-domains with size $l_1^{\text{meso}} \times l_2^{\text{meso}}$. The corresponding apparent adhesive contact forces are evaluated using the semi-analytical contact model developed in Chapter 3. By inserting each set of N_P apparent contact forces into Eqs. (5.11, 5.12), the corresponding behavior of a structure realization is evaluated. The MCS results in a set of N_{MC} structural behaviors from which their statistical properties, e.g. mean, variance, distribution, are identified. The number of explicit evaluations of the apparent adhesive contact forces is thus $N_{MC} \times N_P$.

The alternative method is the stochastic model-based approach, in which instead of using the explicitly evaluated contact forces, N_{MC} sets of N_P contact forces are generated using the stochastic model developed in Chapter 4. Applying the same process as in the direct MCS, N_{MC} structural behaviors are then evaluated, and their statistical properties are identified. When using the stochastic model of apparent adhesive contact forces, there exists an additional approximation – the approximation in terms of distribution – see Eq. (4.16). The effect of this approximation on the accuracy when predicting the upper-scale quantities will be verified by comparing the results of the two approaches in Sec. 5.3. Thanks to that approximation, the required number of the apparent adhesive contact forces that are explicitly evaluated is significantly reduced, i.e. $m \ll N_{MC} \times N_P$, and the computational efficiency is improved, see details in Sec. 5.3.3.

Remarks: (i) In a conventional multiscale model in which the apparent contact forces are deterministic, the distance between two adjacent integral points is much bigger than the meso-scale length, $l^{\text{quad}} \gg l^{\text{meso}}$. For the present case, since the apparent contact forces are non-deterministic, as observed in Chapter 3, in order to account for the size effect on their randomness, the distance between two adjacent integral points, is chosen to be equal to the meso-scale length, $l^{\text{quad}} = l^{\text{meso}}$. The rectangular quadrature rule with equally spaced integral points is therefore applied when evaluating the nodal contact forces. (ii) With this choice, the correlation between the adjacent apparent adhesive contact forces is negligible due to the combination of two effects: the distance between two adjacent points is larger than the correlation length of random surfaces $l^{\text{quad}} = l^{\text{meso}} > l^m$, and the interaction area is much smaller than the apparent one. (iii) When using non-uniformly spaced quadrature rules, e.g. Gauss quadrature rule, the distances between two integral points, l_{quad} , are not constant. This would require either to evaluate different surface sizes l_{meso} , or to consider $l_{\text{meso}} > l_{\text{quad}}$ and to account for the spatial correlation [75]. To keep it simple, we use the rectangle rule.



(a)



(b)

Figure 5.3: Stiction tests reported in [151]. (a) The fabricated micro-cantilever beam arrays (top view). (b) Interferometric image of the cantilever beams undergoing stiction failure for the case of pair a at humidity levels of 45% (top view).

5.3 Verification of the stochastic model-based multiscale method

The probabilistic multiscale methods are applied to quantify the uncertainties of the humid stiction phenomenon of polysilicon micro cantilever beams, as illustrated in Fig. 1.3. In particular, the stiction experiments reported in [151] are modeled. This section provides the comparisons between the two methods, the direct MCS approach and the stochastic model-based approach, in terms of numerical predictions and computational efficiency.

Stiction tests description. In those experiments, stiction tests were performed on arrays of micro polysilicon cantilever beams, see Fig. 5.3(a). First, the cantilever beams were put on the substrates made of silicon or polysilicon. Then, the clamped ends of the beams were moved up to a given height h . Due to the adhesive stress resulting from vdW and capillary interactions, the beams exhibit the S-shape stiction configuration, see Fig. 5.3(b). Note that, in practice, there exists another failure configuration, the arc-shape configuration which is characterized by a lower required adhesion energy see Fig. 1.3. The S-shape configuration was often used in stiction experiments as it is more stable. Using an interferometric device, the failure configurations of beams are captured, see Fig. 5.3(b). The crack length, l_s , was then measured and used to evaluate the upper-scale apparent adhesion energy Γ (in J/m²) as [88, 89, 31]

$$\Gamma = \frac{3}{2} E \frac{h^2 t^3}{l_s^4}, \text{ for S-shape failure,} \quad (5.13)$$

or as

$$\Gamma = \frac{3}{8} E \frac{h^2 t^3}{l_s^4}, \text{ for arc-shape failure,} \quad (5.14)$$

where E is the Young's modulus of the beam, and t is the beam thickness. For the deterministic problems, $\Gamma = \bar{e}$, where \bar{e} is the meso-scale apparent adhesion energy defined in Eq. (3.16). The development of Eqs. (5.13), (5.14) are given in Appendix D.2.

Three sets of tests were conducted with two different beam sets B1, B2 and two different substrates Sub1, Sub2, as: (i) pair a: between beam set B1 and substrate Sub 1, (ii) pair b: between beam set B2 and substrate Sub1, and (iii) pair c: between beam set B1 and substrate Sub2, see their properties in Tab. 2.3. All the contacting surfaces were treated to become super-hydrophilic, i.e. almost zero contact angle. The geometrical dimensions of the beams are: the beam thickness $t = 2.6 \mu\text{m}$, the beam length $L = 1500 \mu\text{m}$, the beam width $w = 30 \mu\text{m}$. The gap is $h = 20 \mu\text{m}$ for pairs a and b. For pair c, the value h was not reported in the reference [151]. Because the reported values of apparent adhesion energies for pair c are much smaller in comparison with pairs a, b, we chose $h = 2 \mu\text{m}$ in order to ensure that the modeled beams reach the S-shape configuration.

Because of the large computational cost of the direct MCS approach, in this section only one case is considered to verify the accuracy of the stochastic model-based approach, i.e. pair b at $RH = 0.65\%$. In that case, the random surfaces \mathcal{S} and \mathcal{S}' are respectively the surfaces B2 and Sub1, see Tab. 2.3 for their properties. In the following, the multiscale model of the adhesive cantilever beam is first illustrated on a generated surfaces pair realization, before being coupled with the uncertainty quantification methods, i.e. the direct MCS approach and the stochastic model-based approach. After being numerically verified with the direct MCS, the stochastic model-based approach will be experimentally validated in Sec. 5.4 for the other humidity levels and the other pairs.

5.3.1 Implementation of the deterministic multiscale FE model for micro cantilever beam undergoing stiction

A pair of surfaces \mathcal{S} and \mathcal{S}' of size corresponding to the beam bottom area, $l \times w$, is generated using the surfaces generator developed in Chapter 2³. The surfaces are then divided into N_p non-overlapping surfaces \mathcal{S}^r and \mathcal{S}'^r of size $l^{\text{meso}} \times w$, with $r = 1, \dots, N_p$ and $N_p = l/l^{\text{meso}}$, corresponding to N_p contact sub-domains. The value of l^{meso} is chosen to be $1.5 \mu\text{m}$ and the corresponding value of N_p is 1000. That choice will be justified later in this section by a convergence analysis. The apparent adhesive contact forces are evaluated for each contact sub-domain by solving the meso-scale contact problem using the methodology described in Section 3.4 and then fitted via the analytical function defined by Eq. (4.5). They are then integrated into the FE model of cantilever beam using Eq. (5.12) to evaluate the corresponding structural behavior. In the following, the main numerical features of the multiscale FE model of the micro cantilever beam are discussed. In addition, the negligibility of the spatial correlation between neighbor apparent contact forces is verified.

Failure simulation process. In the present numerical model, to predict the stiction configuration of a micro cantilever beam with the shortest possible crack length, we perform a loading-unloading simulation. The process is illustrated in terms of the evaluation of the beam central line in Figs. 5.4(a,b), and in terms of the evaluation of the beam internal energy in Fig. 5.4(c). The internal energy is evaluated as

$$U_E = \frac{1}{2} \{\mathbf{u}\}^T [K] \{\mathbf{u}\}. \quad (5.15)$$

The two phases of the process are described in the following.

- (i) **Loading:** The cantilever beam is first loaded by increasing an external force applied at a given distance, e.g. $100 \mu\text{m}$, from the clamp. The external force pushes the cantilever beam into contact with the substrate, see Fig. 5.4(a). When a contact zone is initiated, the apparent adhesive contact forces are activated and pull the cantilever beam on its substrate, and, as a consequence, the contact zone develops. The loading process is ended when the loaded crack length reaches a certain value which is smaller than the expected minimum crack length. The pull-in phenomenon⁴, see Figs. 5.4(a, c), characterized by the sharp increase of the internal energy resulting from the increase of the beam deformation, is observed during the loading process. Because the apparent contact forces of different contact

³A huge computer memory is required when generating a surface of size $l^{\text{meso}} \times w = 1500 \times 30 \mu\text{m}^2$ with the interval 5 nm. Therefore, instead of generating that big surface, we generate 50 statistically independent surface samples of size $30 \times 30 \mu\text{m}^2$ to build up the required surface

⁴Pull-in phenomenon is due to the instability happening when two bodies approach each other under adhesive contact condition. Pull-in is a sharp change of contacting bodies from a current equilibrium configuration to a new one with higher adhesion energy due to the acting of adhesive forces.

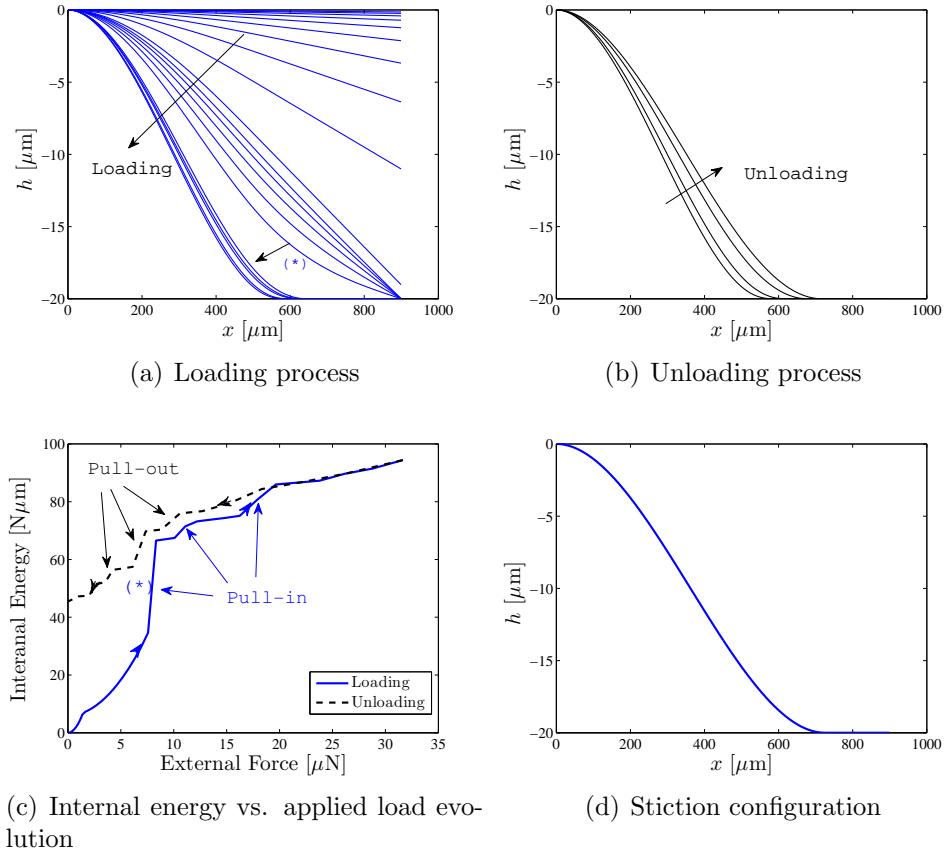


Figure 5.4: The failure simulation process. (a) The evaluation of the beam central line during the loading process. The pull-in marked as (*) is illustrated in the evaluation of internal energy, see Fig. 5.4(c). (b) The evaluation of the beam central line during unloading process. (c) The evaluation of internal energy during loading and unloading process. The pull-in marked as (*) is illustrated in the evaluation of the beam central line, see Fig. 5.4(a). (d) The obtained configuration of beam central line at the stiction failure state.

sub-domains are different, the pull-in phenomenon occurs multiple times. That phenomenon is also experimental observed in [121].

- (ii) **Unloading:** The applied load is then gradually decreased to zero, see Fig. 5.4(b). At the end of the unloading process, the failure configuration can be obtained, see Fig. 5.4(d). As during the loading process, the pull-out phenomenon⁵, see Fig. 5.4(b,c), characterized by the simultaneous decrease of the internal energy, can be observed multiple times during the unloading process.

⁵Pull-out phenomenon is due to the instability happening when separating two bodies from each other under adhesive contact condition. Pull-out is a sharp change of contacting bodies from a current equilibrium configuration under adhesive forces to a new one with lower adhesion energy.

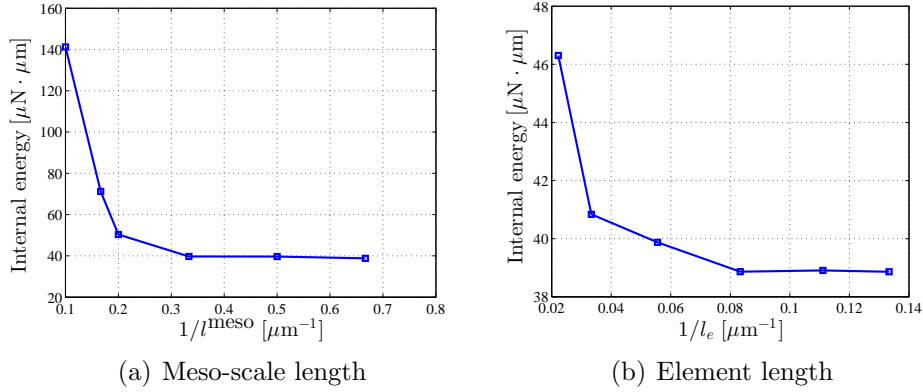


Figure 5.5: The convergence analysis with respect to (a) the meso-scale length l^{meso} , and (b) the element lengths l_e , in terms of the internal energies. For the case (a), $l_e = 5l^{\text{meso}}$. For the case (b), $l^{\text{meso}} = 1.5 \mu\text{m}$.

Determination of the meso-scale length. The meso-scale length l^{meso} , is determined in order to satisfy the two conditions: (i) the variation of the beam central line displacement inside a contact sub-domain is negligible in comparison with the root mean square roughness, and (ii) $l^{\text{meso}} > l^{\text{m}}$ in order for the homogenization process to hold. For the first condition, we can perform a convergence analysis with respect to l^{meso} in terms of the beam internal energy. Figure 5.5(a) illustrates the internal energy at the stiction configuration evaluated by the FE models using different meso-scale lengths l^{meso} on the same sample pair of the contacting surfaces \mathcal{S} and \mathcal{S}' . It is observed that the solution converges when reducing the length l^{meso} . These numerical results suggest that we can choose the meso-scale length as $l^{\text{meso}} = 1.5 \mu\text{m}$ for which the condition $l^{\text{meso}} > l^{\text{m}} \sim 0.3 \mu\text{m}$ is also verified, see Fig. 2.15 for the ACFs of the considered random surfaces.

Mesh convergence. The cantilever beam is discretized into finite elements of size $l_e \times w$. The convergence with respect to the element length l_e is illustrated in Fig. 5.5(b). These numerical results suggest that we can choose the element length as $l_e = 7.5 \mu\text{m}$. This means that for each element in the beam FE model, there are five integral points, corresponding to five apparent contact forces, required to evaluate the equivalent nodal forces using Eq. (5.12). The choice of $l_e = 7.5 \mu\text{m}$ and $l^{\text{meso}} = 1.5 \mu\text{m}$ is also verified in Appendix D.2.1 for the deterministic problem for which the analytical solution is available.

Spatial correlation of the neighboring apparent contact forces. The normalized spatial correlations of components V_i with $i = 1, \dots, 4$, see Eq. (4.4), of the random

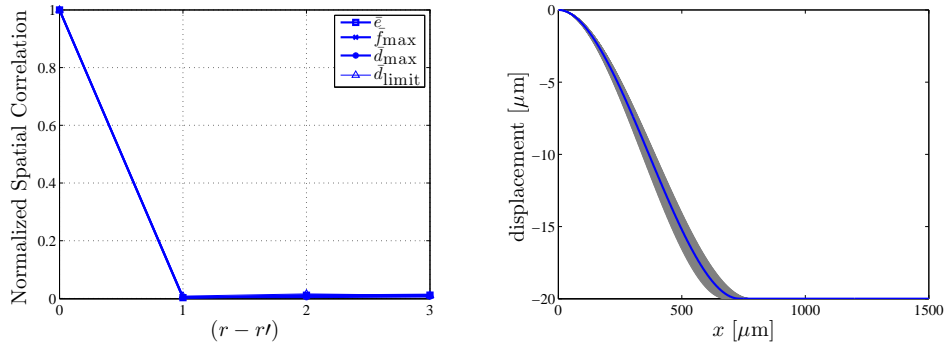


Figure 5.6: FE analysis of the cantilever beams under stiction. (a) The normalized spatial correlations of the random variables $\bar{\epsilon}$, \bar{f}_{\max} , \bar{d}_{\max} , \bar{d}_{limit} for the case of pair b at $RH = 65\%$ considered in Sec. 5.3. The four correlation curves are close to each other. (b) The 1000 realizations of beam structures with a highlighted one obtained by performing the direct MCS on the multiscale beam model. The case of pair b at $RH = 0.65$ is illustrated.

vector \mathbf{V} are defined by

$$\frac{\mathbb{E}[(V_i^r - \mathbb{E}(V_i))(V_i^{r'} - \mathbb{E}(V_i))]}{\mathbb{E}[(V_i - \mathbb{E}(V_i))^2]}, \quad \text{with } \{r, r'\} \in \{1, \dots, N_p\}^2, \quad (5.16)$$

and are illustrated in Fig. 5.6(a). This figure shows that the spatial correlations can be neglected, since in the multiscale model two adjacent contact sub-domains are such that $|r - r'| = 1$, see Fig. 5.2.

In the following, the uncertainty propagation approaches, i.e. the direct MCS method and the stochastic model-based method, are coupled with the multiscale FE model.

5.3.2 Implementation of the two uncertainty quantification approaches

Implementation of direct MCS method. Using the random surface generator described in Section 2.3, one can generate $N_{MC} = 1000$ pairs of surfaces $\mathcal{S}(\theta_k)$, $\mathcal{S}'(\theta_k)$, with $k = \{1, \dots, N_{MC}\}$, of the beam size $l \times w$ from which the N_{MC} corresponding structural behaviors are computed using the multiscale FE model as implemented in Section 5.3.1. The obtained S-shape configurations are visualized in Fig. 5.6(b). From the obtained results, a set of N_{MC} values of the upper-scale apparent adhesion energies is evaluated using Eq. (5.13), and their distribution is then identified.

Implementation of the stochastic model-based multiscale method. Using the stochastic model developed in Sec. 4.4.2, N_{MC} sets of the N_p apparent contact forces are generated. Performing a similar MCS, however using these generated forces, a set of

N_{MC} micro beam behaviors is obtained. The distribution of the upper-scale apparent adhesion energies is then identified.

5.3.3 Comparison between the two uncertainty propagation approaches

The two uncertainty propagation methods, the direct MCS method as a reference and the stochastic model-based method, see Fig. 1.5, are compared in terms of the distributions of the predicted quantities of interest. In addition, a comparison of the computational efficiency of the two methods is performed.

The distributions of crack lengths. The comparison between the results of the stochastic model and the reference ones in terms of statistical quantities and of the distribution of crack lengths is illustrated in Fig. 5.7. The numerical results illustrate that the stochastic model can predict the nominate properties of the crack length distribution.

Computational efficiency. The stochastic model-based method is more efficient than the direct MCS method in terms of computational cost. It is due to the facts that: (i) the number of explicitly evaluated contact forces required to build the stochastic model, $m = 5000$ see Sec. 4.4.2, is much smaller than the one required for the direct MCS, e.g. $N_{MC} \times N_p = 1000000$ for $N_{MC} = 1000$ beam samples and $N_p = 1000$ contact sub-domains; and (ii) the coefficients of the gPCE model, Eq. (4.16), are efficiently evaluated as discussed in Sec. 4.3. Note that the number $N_p = 1000$ is the theoretical number. As we already knew in advance by experiments that the crack lengths is in the range $\min(l_s) > 600 \mu\text{m}$ and $\max(l_s) < 900 \mu\text{m}$, the number of N_p can be reduced to $(\max(l_s) - \min(L_s)) / l^{\text{meso}} \sim 200$. That reduction is not applicable in general when the experiments are not available. To evaluate the stiction failure configuration of one beam sample, a direct MCS method takes several hours (~ 16 hours) on one processor⁶ which mainly devotes for evaluating the 200 apparent adhesive contact forces. In total, obtaining 1000 samples of the beam behaviors requires 671 CPU computing days. In case of the stochastic model-based method, the constructed stochastic model is used to generate the apparent adhesive contact forces, therefore the computational time to obtain the stiction failure of one beam sample devotes only for running the FE model of the beam, and significantly reduces to ~ 5 minutes in the same computing condition. In the stochastic model-based method, $N_p = 1000$ is keep. To construct the gPCE stochastic model from $m = 5000$ samples of explicitly evaluated adhesive contact forces, the computational time for the coefficient identification is only 7 minutes, and the time to explicitly evaluate $m = 5000$ contact forces is 14 CPU computing days. Totally, the computation time to obtain $N_{MC} = 1000$ samples of beam behaviors is only 17 CPU

⁶The performance is measured using Intel® Core™ i7-4600U @ CPU 2.10GHz.

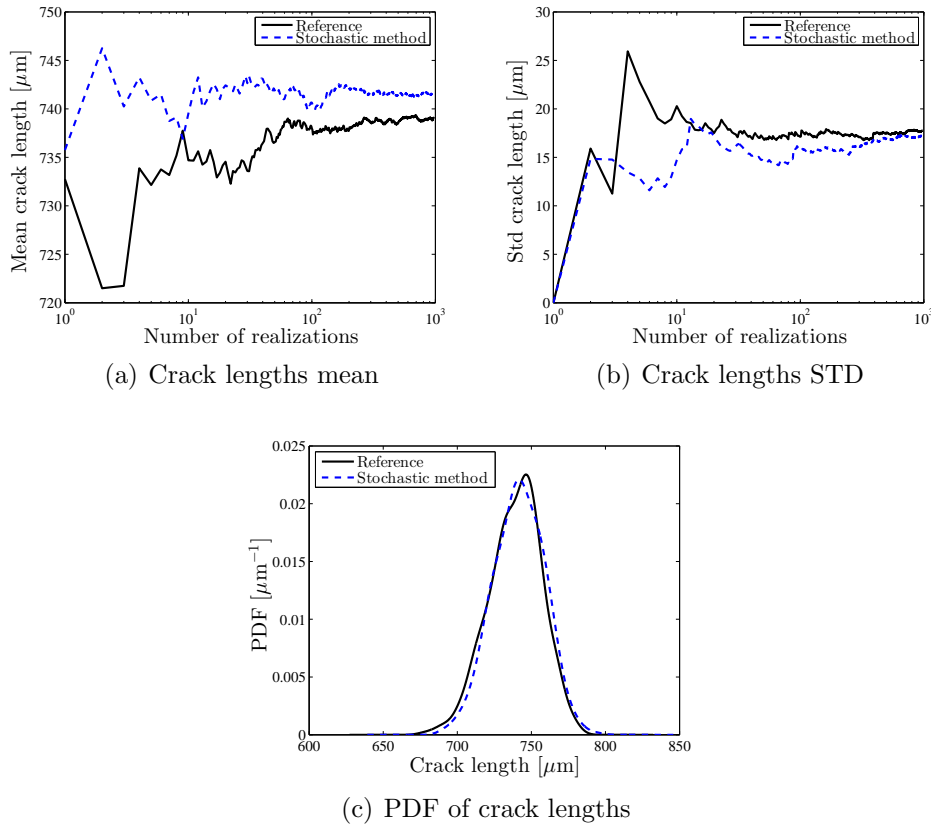


Figure 5.7: The comparison between the two uncertainty propagation methods: stochastic model using gPCE and the direct MCS method as reference in terms of the distribution of crack lengths. (a) The convergence of the mean of crack length. (b) The convergence of the standard deviation (STD) of crack length. (c) The converged distribution of crack length.

days for the stochastic model-based method. For this case, by applying the developed stochastic model-based multiscale method, the overall computational time is reduced by 97% in comparison with direct MCS multiscale method.

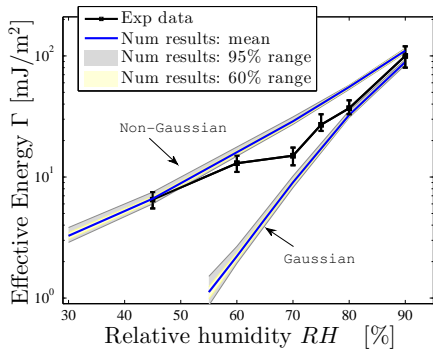
5.4 Validation with experimental results and discussion of physical aspects

In this section, the stochastic model-based multiscale method is applied to predict the stiction tests reported in [151], see their descriptions in Sec. 5.3. The test involves three pairs a, b, and c, see Tab. 3.4. The dimensions of the cantilever beam structures are given as: the beam width $w = 30 \mu\text{m}$ for all these three pairs, and the gap height $h = 20 \mu\text{m}$ for pairs a and b, and $h = 2 \mu\text{m}$ for pair c. In addition to the three

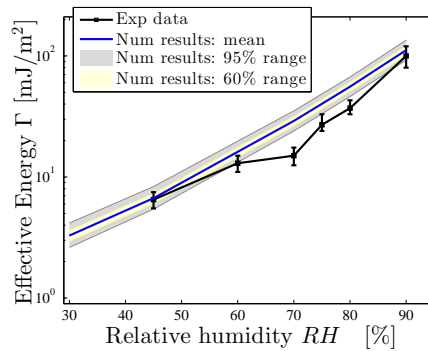
pairs: a, b, and c involved in the stiction tests, the two pairs: I and II, see Tab. 3.4, are also considered with the similar micro cantilever beam structures, $w = 30 \mu\text{m}$ and $h = 20 \mu\text{m}$. Although the length of the experimental beams is $L = 1500 \mu\text{m}$, in the numerical model it was extended up to $4500 \mu\text{m}$ for the low apparent adhesion energies cases, e.g. at low humidity levels, to ensure that the S-shape failures are obtained. Based on the comparison between the numerical predictions and experimental results, the stochastic model-based multiscale method will be validated, and the evolution of the adhesion energies with their uncertainties will be studied.

Due to the fabrication and conducted experimental processes, the geometrical dimensions can vary. The effect of the geometrical dimensions uncertainties should be considered and compared with the one originating from the random surfaces when predicting the probability of the upper-scale apparent adhesion energies. In order to account for the effect of the randomness of the geometrical dimensions, including beam width, beam length, beam thickness and the gap height, on the upper-scale apparent adhesion energies, the current model is extended by considering these dimensions as random variables. For a sake of study purposes, these parameters are modeled as Gaussian random variables with the standard deviations equal to 2.5% of their mean values.

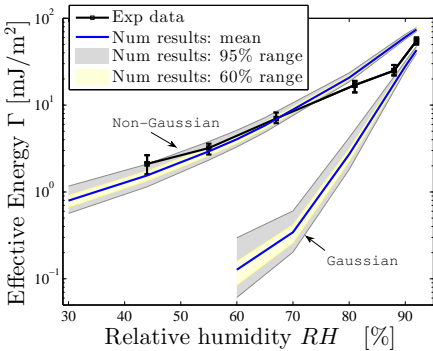
Moreover, an observation from Sec. 3.5 is that the non-Gaussianity of surface heights probability distribution plays an important role in the adhesive contact model. In the following, we bring out the comparison between the experimental results and the numerical results evaluated for three cases: (i) Gaussian contacting surfaces, (ii) non-Gaussian contacting surfaces, and (iii) extending the case (ii) to account for the randomness of geometry. The comparison is conducted using the evaluation of upper-scale apparent adhesion energies illustrated in Fig. 5.8, and using the crack lengths from the numerical model and from the experiments reported in Tabs. 5.1. Based on that comparison, we discuss four issues: the effect of non-Gaussian probability distribution of the contacting surface heights on the upper-scale apparent adhesion energies, the evolution of the upper-scale apparent adhesion energies and of their uncertainty with the humidity level and the surface roughness, the effects of the uncertainties associated with the geometrical dimensions compared to the ones of random surfaces on the structural behaviors, and the validation of the developed method. Although the experiments are not implemented for pairs I and II, during the discussion, we refer to these results, see Figs. 5.9 and Tab. 5.2, as a further source of information.



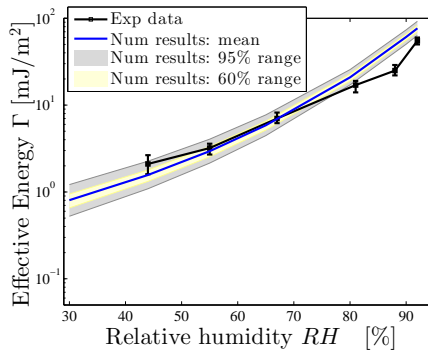
(a) Pair a: experimental data and numerical results for Gaussian and non-Gaussian surfaces



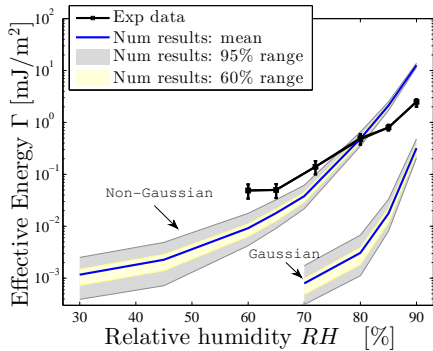
(b) Pair a: experimental data and numerical results for non-Gaussian surfaces with random geometries



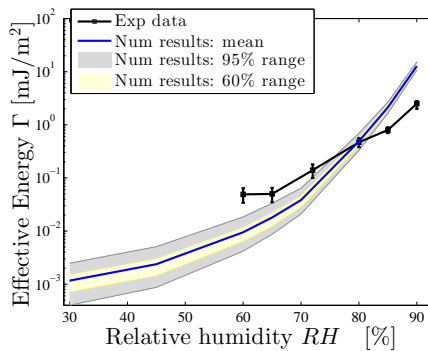
(c) Pair b: experimental data and numerical results for Gaussian and non-Gaussian surfaces



(d) Pair b: experimental data and numerical results for non-Gaussian surfaces with random geometries

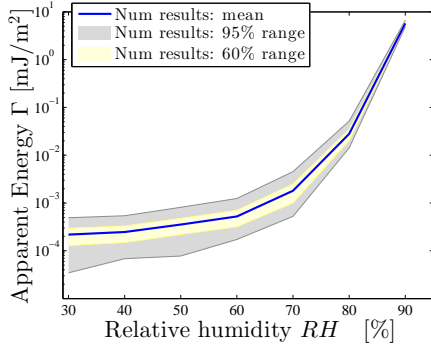


(e) Pair c: experimental data and numerical results for Gaussian and non-Gaussian surfaces

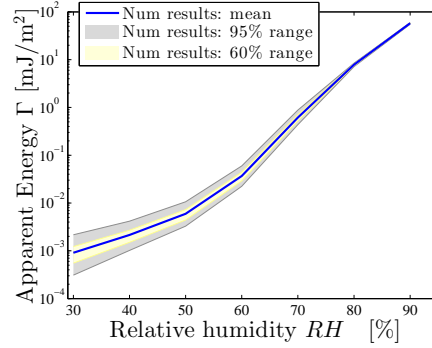


(f) Pair c: experimental data and numerical results for non-Gaussian surfaces with random geometries

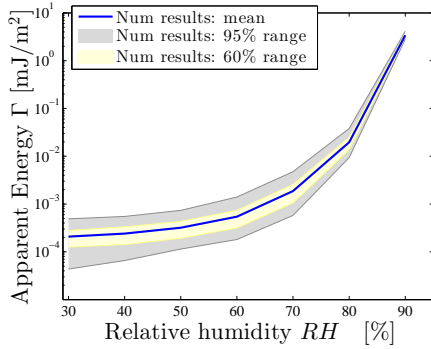
Figure 5.8: Comparison in terms of the upper-scale apparent adhesion energies between experimental (Exp) data and numerical (Num) results for pair a (first row), pair b (second row) and pair c (third row). The numerical results include three cases: (i) Gaussian contacting surfaces, (ii) non-Gaussian contacting surfaces (left column), and (iii) extension of case (ii) to account for the uncertainty in the geometrical dimensions (right column).



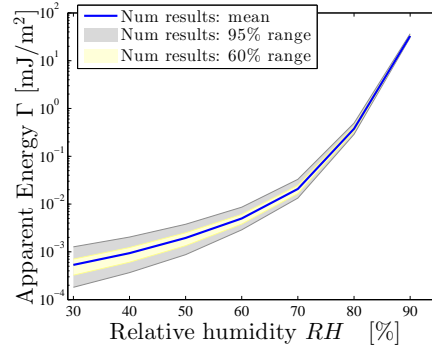
(a) Pair I: Gaussian surfaces



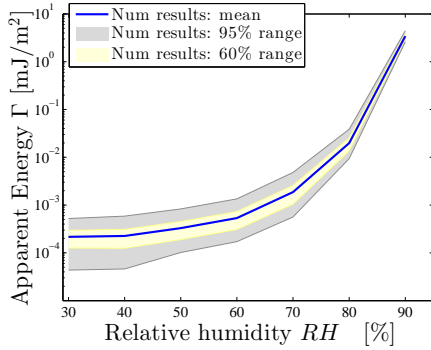
(b) Pair II: Gaussian surfaces



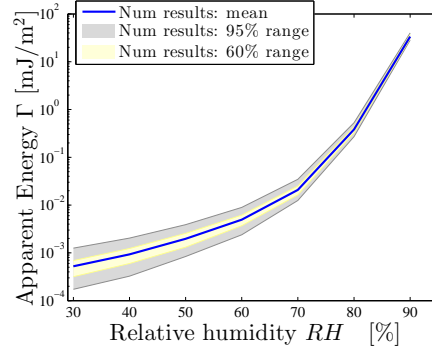
(c) Pair I: non-Gaussian surfaces



(d) Pair II: non-Gaussian surfaces



(e) Pair I: non-Gaussian surfaces with random geometries



(f) Pair II: non-Gaussian surfaces with random geometries

Figure 5.9: The upper-scale apparent adhesion energies for the cases of pair I (left column) and pair II (right column). The numerical results include three cases: Gaussian contacting surfaces (first row), non-Gaussian contacting surfaces (second row), and extension of cases in second row to account for the uncertainty in the geometrical dimensions (third row).

Table 5.1: The comparison of the crack lengths l_s in [μm] obtained from experiments (exps) [151] and from numerical models for pairs a, b, and c, at different humidity levels. Three numerical models are reported: models G and NG for which respectively Gaussian surfaces and non-Gaussian surfaces are considered, and model GEO which extends model NG with the random geometrical dimensions. The results are reported under the form: mean \pm standard deviation. The experimental data are obtained from the errorbar illustration of the upper-scale apparent adhesion energies reported in [151]. The bias errors reported are the differences of the means of crack lengths between the experimental results and numerical predictions evaluated from models NG (which is similar as for GEO).

Pair a							
RH	0.3	0.45	0.6	0.7	0.75	0.8	0.9
l_s (exps)		718 \pm 28	604 \pm 24	582 \pm 24	503 \pm 20	465 \pm 15	362 \pm 18
l_s (G)			940 \pm 19	787 \pm 13	661 \pm 9	480 \pm 4	373 \pm 3
l_s (NG)	853 \pm 15	716 \pm 9	569 \pm 6	494 \pm 4	448 \pm 3	420 \pm 3	353 \pm 3
l_s (GEO)	853 \pm 24	715 \pm 20	567 \pm 14	494 \pm 12	448 \pm 11	420 \pm 10	353 \pm 8
Bias error		0.4%	6%	15%	11%	10%	3%

Pair b							
RH	0.3	0.44	0.55	0.67	0.8	0.88	0.92
l_s (exps)		952 \pm 60	857 \pm 31	705 \pm 24	564 \pm 22	519 \pm 17	420 \pm 10
l_s (G)			1911 \pm 183	1472 \pm 101	870 \pm 44	484 \pm 77	434 \pm 50
l_s (NG)	1220 \pm 54	1031 \pm 38	878 \pm 26	710 \pm 16	538 \pm 8	434 \pm 4	391 \pm 3
l_s (GEO)	1220 \pm 62	1031 \pm 45	878 \pm 34	710 \pm 23	537 \pm 14	434 \pm 10	390 \pm 9
Bias error		8%	3%	0.7%	5%	16%	7%

Pair c							
RH	0.3	0.6	0.65	0.72	0.8	0.85	0.9
l_s (exps)		770 \pm 62	767 \pm 60	593 \pm 44	438 \pm 21	383 \pm 12	289 \pm 12
l_s (G)				2186 \pm 271	1563 \pm 204	994 \pm 3	472 \pm 3
l_s (NG)	1960 \pm 302	1200 \pm 131	1014 \pm 99	752 \pm 61	436 \pm 20	301 \pm 9	192 \pm 3
l_s (GEO)	1965 \pm 308	1201 \pm 131	1016 \pm 105	752 \pm 68	436 \pm 24	303 \pm 11	192 \pm 5
Bias error		56%	32%	27%	0.5%	21%	34%

Table 5.2: The comparison of the crack lengths l_s in [μm] obtained from numerical models for pairs I and II at different humidity levels. Three numerical models are reported: models G and NG for which respectively Gaussian surfaces and non-Gaussian surfaces are considered, and model GEO which extends model NG with the random geometrical dimensions. The results are reported under the form: mean \pm standard deviation.

Pair I							
RH	0.3	0.4	0.5	0.6	0.7	0.8	0.9
l_s (G)	3104 \pm 444	2989 \pm 371	2746 \pm 378	2484 \pm 311	1840 \pm 253	901 \pm 72	234 \pm 7
l_s (NG)	3150 \pm 452	3021 \pm 395	2801 \pm 340	2474 \pm 318	1801 \pm 246	989 \pm 92	267 \pm 7
l_s (GEO)	3136 \pm 468	3101 \pm 448	2801 \pm 382	2484 \pm 322	1822 \pm 247	986 \pm 92	267 \pm 9
Pair II							
RH	0.3	0.4	0.5	0.6	0.7	0.8	0.9
l_s (G)	2162 \pm 264	1718 \pm 153	1324 \pm 95	835 \pm 50	412 \pm 18	217 \pm 11	135 \pm 1
l_s (NG)	2472 \pm 294	2130 \pm 224	1764 \pm 174	1381 \pm 91	964 \pm 55	464 \pm 16	151 \pm 2
l_s (GEO)	2484 \pm 297	2138 \pm 239	1764 \pm 185	1390 \pm 103	965 \pm 60	464 \pm 20	151 \pm 3.5

Effect of non-Gaussian probability distribution of contacting surface heights. As it is observed from the first column of Fig. 5.8, the numerical results are significantly improved when accounting for the non-Gaussian effect. For the considered cases of pairs a, b, and c, the upper-scale apparent adhesion energies are increased and their uncertainties are decreased when accounting for non-Gaussian properties. Interestingly for the case of pair II, the trend is opposite the upper-scale apparent adhesion energies are reduced and their uncertainties are larger, see Fig. 5.9(b, d) and Tab. 5.2. For pair I, there is no significant difference between the Gaussian and non-Gaussian cases, see Fig. 5.9(a, c) and Tab. 5.2. This is explained by considering the values of the skewness and the kurtosis of the involved surfaces reported in Tabs. 2.2 and 2.3. The values of the skewness are negative for the surfaces involved in pairs a, b and c, while they are positive for the ones involved in pairs II. For pair I, the involved surface does not exhibit a significant non-Gaussian character. The asperities heights are more uniform when the skewness of the surface heights decreases, and in particular when it becomes negative, see analysis in Sec. 2.4. The observations at the structural behavior are thus consistent with the ones in the meso-scale apparent contact forces discussed in Sec. 3.5.

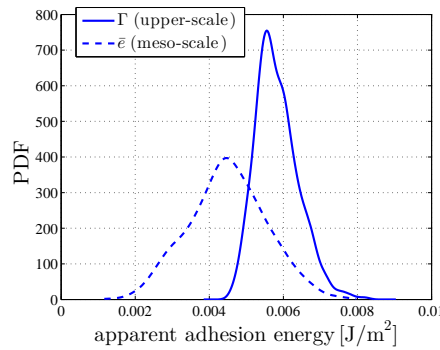


Figure 5.10: The distribution of the upper-scale apparent adhesion energies Γ and the meso-scale apparent adhesion energies \bar{e} . The case of pair b at $RH = 0.65$ with non-Gaussian surfaces is illustrated.

It is remarked that the distribution of the upper-scale apparent adhesion energies Γ is not identical to the one of the meso-scale apparent adhesion energies \bar{e} , see Fig. 5.10. Indeed, the uncertainty range is reduced at the upper-scale as the apparent contact area increases.

The evolution of the upper-scale apparent adhesion energies and of their uncertainty. From both the experimental results and the numerical results, it is observed that the upper-scale apparent adhesion energies increase with the humidity and decrease with the roughness, see Figs. 5.8 and 5.9. It is deduced that the contribution of the capillary interaction is dominant on the vdW one in this problem, and that the upper-scale apparent adhesion energies significantly depend on the topologies of the contacting surfaces as expected. In addition, because the interacting areas are smaller

for the lower adhesion energies, the lower the apparent adhesion energy the larger its uncertainty. Since at high humidity levels the menisci are larger and might be connected – the saturation effect –, the interaction area increases and the uncertainty of upper-scale apparent adhesion energies is reduced. Note that the apparent adhesion energy resulting from the capillary interaction reaches its maximum value, $(2\gamma_{LG})$, when the contacting gap is fully saturated. The reduction of uncertainties at high humidity levels is observed from both numerical results and experimental results for pairs b, c, I and II, see Figs. 5.8 and 5.9. For pair a, that trend is not significant. It is explained by the facts that: (i) the upper-scale apparent adhesion energies for the case of pair a are the largest ones compared to the other pairs in the same environmental condition, $\Gamma/(2\gamma_{LG}) \geq 10\%$ for $RH \geq 60\%$; and (ii) there are other uncertainty sources whose effects are independent from the adhesion energies, e.g. the uncertainty of the geometrical dimensions discussed in following.

Effect of the geometrical dimensions uncertainties As it is observed from Figs. 5.8 and 5.9, for the low apparent adhesion energies, e.g. $\Gamma/(2\gamma_{LG}) < 10\%$, the uncertainties resulting from the scatter in the geometrical dimensions are less important than the ones resulting from the rough surfaces, however they become dominant for the higher values of apparent energies, e.g. the case of pair a for $RH \geq 60\%$, since the effective contact areas increase.

Validation of the stochastic model-based multiscale method As it was discussed in Sec. 2.4.2, we do not have a direct access to the AFM measurements of the surfaces involved in the considered stiction tests. It turns out that there exist errors when estimating the PSD functions indirectly using the analytical formulation described in Eq. (2.36), see Tab. 2.3. As a result, the errors in the numerical predictions are unavoidable. From Chapter 2, particularly from the comparison reported in Tab. 2.3 between the experimental surfaces and the generated surfaces in terms of the average radius of the summits and of their density, the error is negligible for B2 and Sub1 (involved in pair b), moderate for B1 (involved in pair a), and significant for Sub2 (involved in pair c). Interestingly, the deviations between the experimental data and the numerical results have the same trend. The deviations are small for pairs a and b, i.e. the average values of the bias errors is 7% in terms of crack lengths, while they are significant for pair c, i.e. the average value of the considered bias errors is 26%, see Fig. 5.8 and Tab. 5.1. Let us consider the pair c. In comparison with the two other pairs, the reported experimental upper-scale apparent adhesion energies of the pair c are the lowest ones with values in the range $\Gamma \in [0.035, 2.7]$ mJ/m² for $RH \in [0.6, 0.9]$. Based on these values, the ratio between the interacting area and the apparent one is close to the ratio $\Gamma/(2\gamma_{LG}) \in [0.03\%, 1.9\%]$. With that very small part of the topology involved in the contact interaction, the sensitivity of the predicted upper-scale apparent adhesion energies with respect to the errors in the input data, including the probability distribution and the PSD function of surface heights, is significant. Therefore, the errors

produced by the indirect estimation of the PSD function discussed previously results in an important deviation of the numerical predictions which is observed in Tab. 5.1 for pair c.

A remark is raised from that comparison: when dealing with the contact problems in which the ratios of the interacting area to the apparent area are small, e.g. $< 2\%$ for the considered cases, a high accuracy is required when estimating the probability density function and the PSD function of random contacting surfaces. As discussed in Sec. 2.3.2, this could require an important effort on the whole process to reduce the involved errors including data errors resulting from the measurement process, and the modeling errors when using the spectral representation method.

5.5 Conclusion

In this chapter, a probabilistic multiscale FE model was developed to evaluate the probabilistic behaviors of micro devices subjected to adhesion contact. The adhesion contact at the lower-scale was represented in the upper-scale FE model using probabilistic meso-scale apparent adhesive contact forces. To solve the probabilistic multiscale FE model, two approaches were proposed: the direct MCS approach in which the required contact forces are explicitly evaluated, and the stochastic model-based approach in which the required contact forces are generated using the stochastic model developed in the previous Chapter 4. Applying the two methods for the micro cantilever beam stiction tests, it was observed that the numerical predictions of the second approach approximate with accuracy the ones of the direct MCS approach. Therefore, the stochastic model-based approach is numerically verified. Furthermore, the stochastic model-based approach is much more efficient compared to the direct MCS one. Indeed, the computational time was reduced by 97% when using the stochastic model-based approach.

The developed stochastic model-based multiscale method was then validated with the experimental data of cantilever beam stiction tests reported in the literature [151]. Although we did not have a direct access to the AFM measurements of the surfaces to implement accurately the characterization step as discussed in Sec. 2.4.2, the evaluation of the adhesion energies with their uncertainties in terms of roughness and humidity level were well predicted. Using the numerical model, the following observations are pointed out and verified by the experimental results.

- (i) As discussed in Chapter 2 and Chapter 3, since the contacting area is small in comparison with the apparent one, and since the contact involves only the highest asperities, the surface heights probability distribution plays a significant role in the adhesive contact. To improve the accuracy in modeling this distribution, especially further from the mean value, the non-Gaussian characteristics are required to be accounted for. By accounting for the non-Gaussianity of surface heights, the numerical predictions are significantly improved with respect to the experimental results.

- (ii) Because the interaction areas are smaller for the lower apparent adhesion energies, the smaller these energies the larger their uncertainties. The effect of random surfaces on the probabilistic adhesion behaviors is thus important for the low apparent adhesion energies, e.g. $<10\%$ of the theoretical one for the considered cases. However, they become negligible in comparison with the one due to the geometry dimensions uncertainty for the higher energies.
- (iii) The numerical investigation shows that the smaller the adhesion energies the higher the accuracy required when characterizing the random surfaces by their probability density function and PSD function.
- (iv) When the statistical properties of contacting surfaces are well approximated by the numerical surfaces, the differences between numerical predictions and the experimental data are small, i.e. $\sim 7\%$ in terms of the mean of crack lengths.

Chapter 6

General conclusions and perspectives

The objective of this work was to predict in a probabilistic way the behavior of micro devices subjected to adhesive contact between rough surfaces. Toward this end, we have developed a stochastic model-based multiscale method.

A surface generator was firstly developed. From AFM measurements, the probability density function and the PSD function of surface heights were evaluated. The probability distribution was characterized using the ME method for which the non-Gaussianity is accounted for. A non-Gaussian surface generator was then implemented using the obtained probability density function and PSD function as input data.

Secondly, a semi-analytical contact model was developed to evaluate the apparent contact forces between two random surfaces subjected to the adhesive capillary and vdW interactions. The contact model has the ability to account for the size effect, for the non-Gaussianity in the surface heights probability distribution, and for saturation phenomenon, while it remains efficient in terms of computational cost. Furthermore, the model overcomes the disadvantages of assuming asperities as local summits, used in the GW model and the BGT model, allowing the asperities radius to be evaluated independently with the sampling interval.

A stochastic model was then developed to efficiently represent the randomness of the apparent adhesive contact forces. The apparent adhesive contact forces were parameterized and represented by parameters vectors. The randomness of these parameters vectors is modeled using a truncated gPCE. The gPCE model was constructed by numerically projecting the Rosenblatt transformation on a system of orthogonal polynomials using a quadrature rule which requires a negligible computational cost. With the constructed stochastic model, samples of the apparent adhesive contact forces were generated efficiently.

Finally, a probabilistic multiscale FE model was developed to evaluate the probabilistic behaviors of micro structures subjected to adhesion. In that model, the apparent contact forces were integrated as the random contact laws at integral points. To evaluate the probabilistic behavior of micro structures, the direct MCS requires a large number

of explicitly evaluated apparent contact forces, and consequently becomes inefficient in terms of computational costs. By using the constructed stochastic model to generate the required forces and then performing MCS using these forces, the computation cost is significantly reduced, i.e. 97% in total for the studied cases. The numerical predictions obtained by the two methods, direct MCS approach and stochastic model-based approach, were shown to have negligible differences. Therefore the stochastic model-based approach was verified.

After being verified, the stochastic model-based multiscale method was applied to model stiction tests from literature. It was also applied to the experimental surfaces fabricated at IMT-Bucharest lab. The comparison between numerical predictions and experimental results shows that: the numerical results predict well the evolution of the adhesion energies and of their uncertainty in terms of roughness and humidity levels. Due to the lack of a direct access to the AFM measurements of contacting surfaces involved in the stiction tests, the PSD functions were estimated indirectly using some limited statistical properties. For the cases that these statistical properties are well approximated by the generated surfaces, the differences between numerical predictions and experimental data when predicting the stiction tests are small, i.e. $\sim 7\%$ in terms of the mean of crack lengths.

Using the model, the following physical aspects are observed. (i) Due to the small ratio between the interaction area and the apparent one, the surface heights probability distribution plays a significant role in the adhesive contact. To improve accuracy in modeling this probability distribution, especially when getting further from the mean value, the non-Gaussian characteristics are required to be accounted for. (ii) The smaller the adhesion energy, the larger its uncertainty. (iii) For the studied cases, the uncertainty in adhesion energy resulting from the randomness of contacting surfaces becomes negligible compared to the other sources, e.g. uncertain geometrical dimensions, when it is above 10% of the theoretical value – obtained for perfectly flat contacting surfaces.

In this work, the stochastic model-based multiscale framework is applied for the case of single cantilever beam structures. In the future, it can be applied to predict the stiction risk of multiple micro-beam structures, which are very popular in the context of MEMS, such as accelerometer or comb-driver. In addition, thanks to the flexibility of FE model at the structural scale, the developed model can be used to evaluate the performance of more complicated structures, e.g. the adhesion contact of micro-gears. Furthermore, the developed model can be applied in an optimization process of MEMS design. For instance, we can perform a shape optimization to identify the design with the smallest percentage of stiction failure under other design constraints.

In this work, the irreversible phenomena, e.g. plasticity, fatigue, and wear, were neglected. In practice, these phenomena become important for devices operating over a high number of contact cycles, e.g. contact-type radio frequency MEMS or micro-gears. In these cases, the contacting surface topology as well as the material properties can change during operation. This means that the adhesion behaviors change over time and can eventually lead to the stiction failure, even though the initial design is stiction free.

In the future, these phenomena should be investigated and might be involved in the developed model. The outcome of such a combination would be the ability to predict in a probabilistic way the life time, e.g. the maximum number of operating cycles, of MEMS devices.

In addition, to broaden the applicability, other uncertainty sources, e.g. the clamp stiffness uncertainty and the randomness of grain properties in the polycrystalline material such as polysilicon, can be integrated into the developed model.

Appendix A

Appendices to Chapter 2

A.1 Probability measure space and random variable

$(\Omega, \mathfrak{F}, P)$ is defined as a probability measure space where Ω is the space of outcomes, \mathfrak{F} is the σ -algebra of events – a collection of all the subsets of Ω , and $P : \mathfrak{F} \rightarrow [0, 1]$ is the probability measure satisfying: [17, 27]

- (i) $0 \leq P(\mathcal{F}) \leq 1$ for $\mathcal{F} \in \mathfrak{F}$,
- (ii) $P(\emptyset) = 0$, $P(\Omega) = 1$, and
- (iii) if $\mathcal{F}_1, \mathcal{F}_2, \dots$ is a disjoint sequence of \mathfrak{F} -sets and if $\bigcup_{k=1}^{\infty} \mathcal{F}_k \in \mathfrak{F}$ then

$$P\left(\bigcup_{k=1}^{\infty} \mathcal{F}_k\right) = \sum_{k=1}^{\infty} P(\mathcal{F}_k). \quad (\text{A.1})$$

Let $(\mathcal{V}, \mathfrak{B}_{\mathcal{V}})$ be a measurable space where \mathcal{V} is a finite or infinite dimensional space and $\mathfrak{B}_{\mathcal{V}}$ is a σ -algebra over \mathcal{V} . A random variable \mathbb{X} defined in $(\Omega, \mathfrak{F}, P)$ with values in \mathcal{V} is the result of a measurable mapping from (Ω, \mathfrak{F}) into $(\mathcal{V}, \mathfrak{B}_{\mathcal{V}})$ satisfying

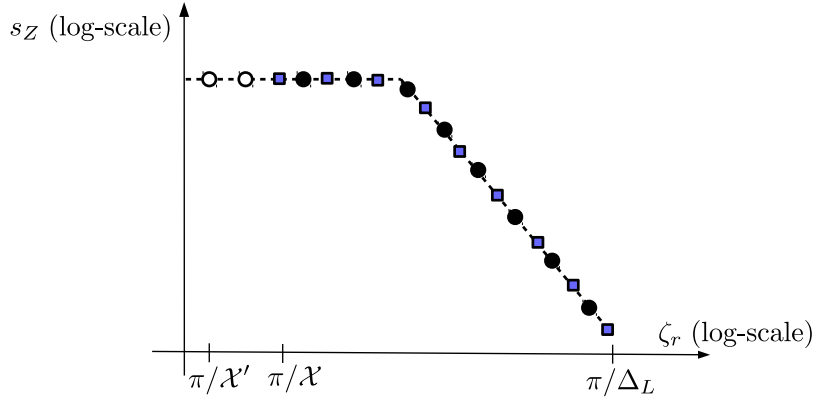
$$\forall B \in \mathfrak{B}_{\mathcal{V}} : \mathbb{X}^{-1}(B) \in \mathfrak{F}, \quad (\text{A.2})$$

where $\mathbb{X}^{-1}(B) = \{\theta \in \Omega \mid \mathbb{X}(\theta) \in B\}$. The probability of a random variable \mathbb{X} is defined as

$$P_{\mathbb{X}}(B) = P(\mathbb{X}^{-1}(B)). \quad (\text{A.3})$$

A.2 Dealing with the different sizes of generated and measured surfaces

In practice, the sizes of the generated surfaces and of the measurements are not the same. It is often that the size of the generated surfaces is larger than the measurement



- theoretical PSD function
- evaluated PSD function obtained from measurements
- additional wave numbers outside the measurable range
- additional wave numbers inside the measurable range

Figure A.1: An example of the evaluation of PSD function at the additional wave numbers required when generating surfaces whose size is larger than the measurement one. The theoretical PSD function is given by Eq. (2.36).

ones, i.e. $\mathcal{X}' > \mathcal{X}$. As a result, there exist additional sampling wave numbers at which the PSD function is required to be evaluated.

For the wave numbers outside the measurable range defined by Nyquist-Shannon, i.e. either ζ_{l_1} or ζ_{l_2} belongs to $\{[-\pi/\mathcal{X}, -\pi/\mathcal{X}'] \cup [\pi/\mathcal{X}', \pi/\mathcal{X}]\}$, the simple way is to set the PSD function to zero at these wave numbers. However, the obtained generated surfaces are periodic – a property that should be avoided when the size effects are required to be accounted for. Instead, the PSD function is evaluated at these wave numbers using the interpolation method from the measured values. As it was observed in [101], for many different experimental surfaces, the PSD functions are approximately constant at low wave numbers, see Fig. A.1. Therefore, the use of interpolation method for the wave numbers outside the measurable range – which are the low ones – is acceptable.

For the additional wave numbers inside the measurable range, the PSD function can be evaluated either using an interpolation method or using additional FFT calculations. To keep it simple, the interpolation technique is applied in this work, see Fig. A.1. For completeness, we report the latter technique in the following for the applications discussed in Sec. 2.4.1.

In Sec. 2.4.1, to obtain the PSD function, the input topology data are the surfaces $z(x_1^{(i)}, x_2^{(i)})$ with the sampling distance $\Delta x = 5$ nm and the size $\mathcal{X}^0 = 1.28$ μm . The sampling in the space domain of these surfaces is $\{(x_1^{(i)}, x_2^{(j)})\}$, $1 \leq i, j \leq n_s$ with $\{(x_1^{(i)}, x_2^{(j)}) = (-\mathcal{X}^0/2 + (i-1)\Delta x, -\mathcal{X}^0/2 + (j-1)\Delta x)\}$, $1 \leq i, j \leq n_s$, and $n_s = 256$. The sampling of their PSD function is $\{(\zeta_{l_1}, \zeta_{l_2}) = (-\zeta_L + (l_1-1)\Delta\zeta^0, -\zeta_L + (l_2-1)\Delta\zeta^0)\}$, $1 \leq l_1, l_2 \leq 256$, with $\Delta\zeta^0 = 2\zeta_L/256$ and $\zeta_L = \pi/5$ nm^{-1} . Let us now assume we want

to generate a $5.12 \times 5.12 \mu\text{m}^2$ surface with a sampling distance of 5 nm^{-1} . The sampling of the wave number domain requires a higher resolution as $\{(\zeta_{l'_1}, \zeta_{l'_2}) = (-\zeta_L + (l'_1 - 1)\Delta\zeta, -\zeta_L + (l'_2 - 1)\Delta\zeta), 1 \leq l'_1, l'_2 \leq 1024\}$, with $\Delta\zeta = 2\zeta_L/1024 (= \Delta\zeta^0/4)$. For the the additional points that are located inside the measurable range stated in Nyquist-Shannon theorem, $\{(\zeta_{l_1+k_1}, \zeta_{l_2+k_2}) = (-\zeta_L + (l_1+k_1-1)\Delta\zeta^0, -\zeta_L + (l_2+k_2-1)\Delta\zeta^0)$ with $k_1, k_2 \in \{0, -1/4, -1/2, -3/4\}$, the Fourier transform $\hat{z}(\zeta_{l_1+p}, \zeta_{l_2+q})$ can be estimated by the following equation

$$\begin{aligned} \hat{z}(\zeta_{l_1+k_1}, \zeta_{l_2+k_2}) = & \\ & \left[(\Delta x)^2 \exp \left(\sqrt{-1}(n_s/2 + 1) \frac{2\pi}{n_s} (l_1 + k_1 - 1) + \sqrt{-1}(n_s/2 + 1) \frac{2\pi}{n_s} (l_2 + k_2 - 1) \right) \right] \times \\ & \left[\sum_{i=1}^{n_s} \sum_{j=1}^{n_s} z(x_1^{(i)}, x_2^{(j)}) \exp \left(\sqrt{-1}\pi \left(i - n_s/2 - 1 - i \frac{2}{n_s} k_1 \right) + \sqrt{-1}\pi \left(j - n_s/2 - 1 - j \frac{2}{n_s} k_2 \right) \right) \right. \\ & \left. \times \exp \left(-\sqrt{-1}i \frac{2\pi}{n_s} (l_1 - 1) - \sqrt{-1}j \frac{2\pi}{n_s} (l_2 - 1) \right) \right], \end{aligned} \tag{A.4}$$

on which we can apply the FFT algorithm.

Appendix B

Appendices to Chapter 3

B.1 Analytical asperity contact models

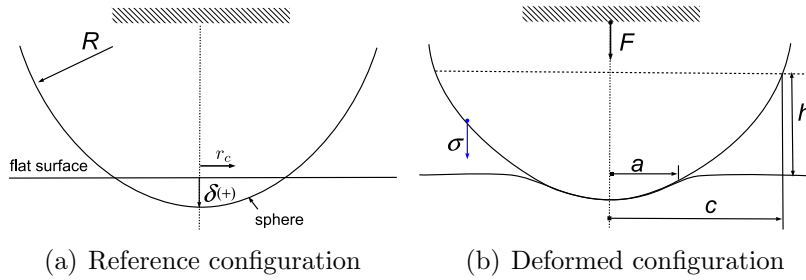


Figure B.1: The initial configuration (a) and the deformed configuration (b) of the problem of adhesive contact between a sphere and a flat surface. Depending on the considered physical problem, the adhesive interaction height h can be either the height of condensing water h_{water} or the range of the vdW adhesive pressure h_{vdW} , the adhesive interaction radius c can be either the water condensing radius c_{water} or the vdW adhesive radius c_{vdW} .

B.1.1 Hertz model

Considering the frictionless elastic non-adhesive contact problem between a sphere and a half plane, the Hertz stress distribution resulting from an applied force F is obtained by

$$\sigma_z(r_c) = \frac{3F}{2\pi a^2} \left(1 - \frac{r_c^2}{a^2}\right)^{1/2}, \quad (\text{B.1})$$

where $r_c \leq a$ is the projected distance from the contact area center to the considered point and a is the physical contact radius, see Fig. B.1. Based on this pressure distribution, Hertz has established his well-known relationships between the contact radius

a , the interference δ , and the contact load F , which are given by

$$a^3 = \frac{RF}{K}, \quad (\text{B.2})$$

$$\delta = \frac{a^2}{R}, \quad (\text{B.3})$$

where R is the radius of the sphere, $K = \frac{4}{3}[(1 - \nu_1^2)/E_1 + (1 - \nu_2^2)/E_2]^{-1}$ is the reduced elastic modulus with ν_1, ν_2 the Poisson ratios of the sphere and the half plane respectively, and with E_1, E_2 their two Young's modulus.

B.1.2 JKR model

Johnson, Kendall, and Roberts [57] have introduced their frictionless adhesive contact model, which deals with vdW adhesive forces, by assuming that the adhesive force acts only inside the physical contact area, i.e. for $r_c \leq a$ see Fig. B.1. This assumption is valid in case of soft materials and short-range adhesive forces. The JKR model is described by the two equations [57]

$$a^3 = \frac{R}{K}(F + 3\omega_{\text{vdW}}\pi R + \sqrt{6\omega_{\text{vdW}}\pi RF + (3\omega_{\text{vdW}}\pi R)^2}), \quad (\text{B.4})$$

$$\delta = \frac{a^2}{R} - \sqrt{\frac{8\omega_{\text{vdW}}\pi a}{3K}}, \quad (\text{B.5})$$

where ω_{vdW} is the adhesion energy (work of adhesion per unit area) of the vdW interaction. When the surface energy per unit contact area ω_{vdW} is equal to zero, this solution reduces to the Hertz solution.

B.1.3 DMT model

The DMT model [33] assumes that the adhesive forces act only outside of the physical contact area, i.e. for $r_c > a$, and that they do not have a significant effect on the deformation of the contacting bodies. This assumption is valid in the case of hard materials and long-range adhesive forces. Using this assumption, the repulsive forces and the adhesive forces can be evaluated separately. The repulsive forces are calculated from Hertz model, and the adhesive forces are obtained by integrating the adhesive pressure on the deformed bodies computed from Hertz solution. The original DMT model for vdW adhesive forces is given in terms of the adhesion energy ω_{vdW} of the vdW forces. Maugis et al. [91] have proved that this model can also be applied in the capillary adhesive cases by using the adhesion energy obtained from the capillary forces instead of ω_{vdW} . The DMT model is given by

$$a^3 = \frac{R}{K}(F + 2\omega\pi R), \quad (\text{B.6})$$

$$\delta = \frac{a^2}{R}, \quad (\text{B.7})$$

where the second equation results from Hertz model, see Eq. (B.2), and ω either holds for ω_{vdW} or for ω_{water} .

B.1.4 Maugis model and Kim extension

The Maugis model [90] was originally applied to the cases of vdW adhesive forces. In this model, the vdW adhesive pressure field is assumed to follow the Dugdale assumption, in which the vdW adhesive pressure σ_{vdW} is constant between the contact radius a and the vdW adhesive radius c_{vdW} . This adhesive radius c_{vdW} is defined as the radius at which the separation distance between the two surfaces is h_{vdW} and for which the vdW forces vanish, see Fig. B.1. The adhesive pressure σ_{vdW} is chosen as the highest adhesive pressure of the more realistic Lennard-Jones potential and the height h_{vdW} is calculated from the energy conservation condition $\omega_{\text{vdW}} = -\sigma_{\text{vdW}}h_{\text{vdW}}$. Owing to the similarity between the Dugdale assumption and the Laplace pressure field inside the condensing water, Maugis model is also applicable in the capillary adhesive cases [91]. In the following, the main results of Maugis model are presented, depending on the considered application. Maugis model is described by the set of equations

$$A^3 - \lambda A^2 \left(\sqrt{(c/a)^2 - 1} + (c/a)^2 \tan^{-1} \sqrt{(c/a)^2 - 1} \right) = \bar{F}, \quad (\text{B.8})$$

$$A^2 - \frac{4}{3} A \lambda \sqrt{(c/a)^2 - 1} = \Delta, \quad (\text{B.9})$$

$$\begin{aligned} & \frac{\lambda A}{2} \left[\sqrt{(c/a)^2 - 1} + ((c/a)^2 - 2) \tan^{-1} \sqrt{(c/a)^2 - 1} \right] + \\ & \frac{4\lambda^2 A}{3} \left[(\sqrt{(c/a)^2 - 1} \tan^{-1} \sqrt{(c/a)^2 - 1}) - (c/a) + 1 \right] = 1, \end{aligned} \quad (\text{B.10})$$

where λ is the transition parameter defined by

$$\lambda = \left| \frac{2\sigma}{(\pi\omega K^2/R)^{1/3}} \right|. \quad (\text{B.11})$$

where σ , ω either hold for σ_{vdW} , ω_{vdW} or for ΔP , ω_{water} , and A , Δ , \bar{F} are the dimensionless values of the contact area, interference, and external force, respectively. These dimensionless values are defined by

$$A = \frac{a}{(\pi\omega R^2/K)^{1/3}}, \quad (\text{B.12})$$

$$\bar{F} = \frac{F}{\pi\omega R}, \quad (\text{B.13})$$

$$\Delta = \frac{\delta}{(\pi^2\omega^2 R/K^2)^{1/3}}, \quad (\text{B.14})$$

where the interference δ is defined by

$$\delta = \frac{a^2}{R} + \frac{\sigma}{3K} \sqrt{c^2 - a^2}. \quad (\text{B.15})$$

Finally Kim et al. [63] have extended Maugis model to the non-contacting case in which the contact radius $a = 0$ and the radius $c > 0$. Details on the implementation of the Maugis model and Kim extension can be found in [147]. The system of equations in this case is given by [63]

$$1 = \frac{\pi}{4}C^2\lambda + \frac{2}{3}(\pi - 2)C\lambda^2 + \zeta, \quad (\text{B.16})$$

$$\bar{F}_n = -\frac{\pi}{2}C^2\lambda, \quad (\text{B.17})$$

$$\delta = -\frac{4}{3}C\lambda - \frac{2}{\pi}\frac{\zeta}{\lambda}, \quad (\text{B.18})$$

where $C = c/(\pi\omega R^2/K)^{1/3}$ is the dimensionless value of the radius c . This system simplifies into a second order equation in C

$$\frac{\pi}{4}\lambda C^2 - \frac{4}{3}\lambda^2 C - \frac{\pi}{2}\Delta\lambda - 1 = 0. \quad (\text{B.19})$$

By solving the above equations, the dimensionless adhesion contact radius C is obtained and the contact force is obtained using Eq. (B.19).

B.2 Identification and spherical fitting of the contacting asperities

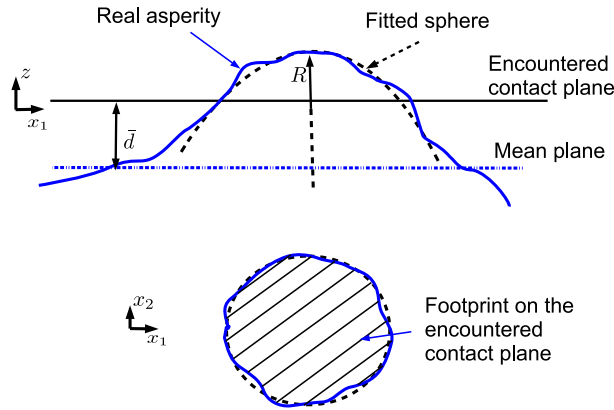


Figure B.2: Illustration of an identified contacting asperity with its fitting sphere.

B.2.1 Theory

Let us consider the topology $z(\mathbf{x})$ with $\mathbf{x} \in \mathfrak{D} \subset \mathfrak{R}^2$ of the contacting surface. The footprint of an identified contacting asperity i is the set $\mathbf{O}_i \subset \mathfrak{D}$ of *connected topology* such that $z(\mathbf{x}) \geq \bar{d}; \forall \mathbf{x} \in \mathbf{O}_i$, where \bar{d} is the contact distance from the mean surface

of $z(\mathbf{x})$ to the encountered surface which is considered as a plane, see illustration in Fig. B.2. The topology of the contacting asperity $\{z(\mathbf{x}), \text{ with } \mathbf{x} \in \mathbf{O}_i\}$ is fitted with a sphere using the following methodology. The topology of the sphere is given by

$$z_{\text{sphere}} = (\sqrt{R^2 - (x_1 - o_1)^2 - (x_2 - o_2)^2} + o_3), \quad (\text{B.20})$$

where R is the radius, and o_1, o_2, o_3 are the coordinates of the sphere center. To fit the identified topology, one can solve the optimization problem

$$(o_1, o_2, o_3, R) \in \arg \min_{(o_1, o_2, o_3, R)} \text{EF}_i = \frac{1}{A\{\mathbf{O}_i\}} \int_{\mathbf{O}_i} [z - z_{\text{sphere}}]^2 d\mathbf{x}, \quad (\text{B.21})$$

where the function EF_i is the mean integral square error between the fitting sphere profile and the real asperity profile of the i th asperity, and $A\{\mathbf{O}_i\}$ is the area of \mathbf{O}_i . To reduce the parameters to be identified, we add an additional constraint which imposes the matching of the footprint areas such that

$$A\{\mathbf{O}_i\} = \pi (R^2 - (\bar{d} - o_3)^2). \quad (\text{B.22})$$

This additional constraint has a physical base as the repulsive force is linearly proportional to the contacting area in the case of rough surfaces [42, 6]. The z_0 coordinate of the sphere center can be directly obtained by

$$o_3 = \bar{d} - \sqrt{R^2 - \frac{A\{\mathbf{O}_i\}}{\pi}}. \quad (\text{B.23})$$

The unknowns $\{o_1, o_2, R\}$ can be determined by solving Eq. (B.21) using a Newton Raphson algorithm. The two parameters, required to evaluate the asperity contact force using Hertz model, include the radius R and the height z_a given by

$$z_a = o_3 + R. \quad (\text{B.24})$$

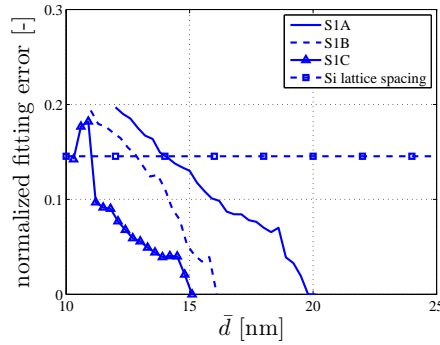
To quantify the error resulting from this asperity representation, we consider the normalized global fitting error relEF

$$\text{relEF} = \frac{1}{rms} \sqrt{\frac{\sum_{i=1}^{n_{\text{asp}}} \text{EF}_i^2 A\{\mathbf{O}_i\}}{\sum_{i=1}^{n_{\text{asp}}} A\{\mathbf{O}_i\}}} \quad (\text{B.25})$$

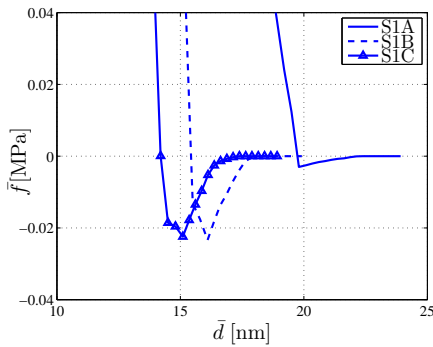
where rms is the root mean square of surface roughness, and n_{asp} is the total number of identified asperities above the contact distance \bar{d} . If this error is smaller or comparable with the lattice spacing (the crystal unit-cell size), the approximation is fully justified as the geometrical approximation is of the same order of the material structure. For the considered silicon material, it crystallizes in a diamond cubic crystal structure with the lattice spacing of 0.543 nm [97].

B.2.2 Illustration for the contact pair I of Sec. 3.5

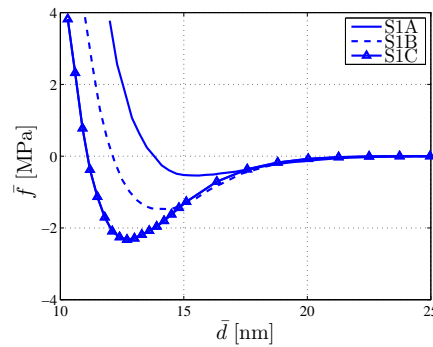
In this section, the developed method is applied for the case of pair I, see Tab. 3.4, with three AFM measurements S1A, S1B, S1C. An example of fitted asperity is illustrated in Fig. 3.5. The normalized fitting errors given by Eq. (B.25) are illustrated in Fig. B.3(a). The apparent adhesive contact forces evaluated using the semi-analytical contact model developed in Sec. 3.4 are also illustrated in Fig. B.3(b,c). As it is observed from Fig. B.3(a) that in the adhesive ranges in which the contact forces are negative, i.e. $\bar{d} > 10$ nm see Fig. B.3(b,c), the fitting errors are smaller or comparable with the lattice spacing.



(a) Normalized fitting error



(b)



(c)

Figure B.3: Fitting error. (a) The normalized fitting error $relEF$ given by Eq. (B.25) for the case of pair I with three samples S1A, S1B, S1C. (b, c) The apparent adhesive contact forces evaluated at $RH = 60\%$ (b), and $RH = 90\%$ (c), for these samples using semi-analytical method developed in Sec. 3.4.

B.3 Verification of the negligibility of plastic deformation

B.3.1 Theory

B.3.1.1 Limit of elasticity deformation using GW model

Asperity contact When considering the contact problem between a sphere of radius R and a flat surface, see Fig. B.1, the maximum stress is given by Hertz model, Eqs. (B.1, B.2, B.3), as

$$\sigma_{z,\max} = \sigma_z(r_c = 0) = \frac{2}{\pi} E' \sqrt{\frac{\delta}{R}}, \quad (\text{B.26})$$

where $E' = [(1 - \nu_1^2)/E_1 + (1 - \nu_2^2)/E_2]^{-1}$. From the work of Tabor [125], the onset of plastic or irreversible deformation occurs when $\sigma_{z,\max} > 0.6\sigma_H$ where σ_H is the material hardness. It turns out that the critical interference for plastic deformation is

$$\delta_P = \left(\frac{\pi}{2}\right)^2 R \left(\frac{0.6\sigma_H}{E'}\right)^2 \sim R \left(\frac{\sigma_H}{E'}\right)^2. \quad (\text{B.27})$$

When $\delta > \delta_P$, the plastic deformations occur.

Rough surfaces contact To assess the importance of plastic deformation in the rough surfaces contact problems, GW model examines the ratio A_p/A , where A is the total physical contact area of all contacting asperities, and A_p is the physical contact area of the asperities whose interference is larger than the critical one given by Eq. (B.27). Using GW model, the ratio A_p/A depends mainly only on the plasticity index which is given by

$$\Psi_P = \sqrt{\frac{\sigma_{\text{sum}}}{\delta_P}} = \frac{E'}{\sigma_H} \sqrt{\frac{\sigma_{\text{sum}}}{\bar{R}_{\text{sum}}}}, \quad (\text{B.28})$$

where $\bar{R}_{\text{sum}} = [1/\bar{R}_{\text{sum}}^{(1)} + 1/\bar{R}_{\text{sum}}^{(2)}]^{-1}$, with $\bar{R}_{\text{sum}}^{(1)}$, $\bar{R}_{\text{sum}}^{(2)}$ the summits mean radii of the two contacting rough surfaces, and $\sigma_{\text{sum}} = [(\sigma_{\text{sum}}^{(1)})^2 + (\sigma_{\text{sum}}^{(2)})^2]^{1/2}$ with $\sigma_{\text{sum}}^{(1)}$, $\sigma_{\text{sum}}^{(2)}$ the standard deviations of the summit heights of these two surfaces. When $\Psi_P < 0.6$, the plasticity deformation is negligible, i.e. $A_p/A < 0.02$, while for $\Psi_P > 1$, the plasticity deformation becomes dominant, i.e. $A_p/A > 0.5$.

In this work, GW model is not applied due to the disadvantages described in Chapter 3. Instead, we have developed the semi-analytical contact model, see Chapter 3. The plasticity criterion developed using this model is described in the following.

Table B.1: The values of plasticity index given by GW model, see Eq. (B.28).

pair	I	II	a	b	c
R_{sum} [nm]	90	93	370	656	93
σ_{sum} [nm]	3.6	1.7	1.5	3.0	3.7
Ψ_P [-]	1.4	0.9	0.4	0.5	1.3

B.3.1.2 Limit of elasticity deformation using the semi-analytical contact model

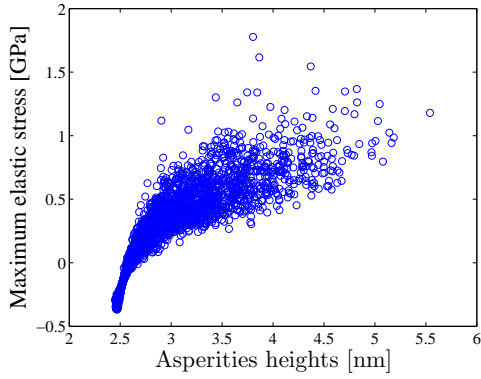
Similarly to the approach applied in GW model, we consider the ratio A_p/A , where the areas are evaluated numerically as

$$\begin{aligned}
 A(\bar{d}) &= \sum_{i=1}^{n_{asp}} A^{(i)} \\
 A_P(\bar{d}) &= \sum_{i=1}^{n_{asp}} \mathbb{1}_{>0}(\sigma_{z,max}^{(i)} - 0.6\sigma_H) A^{(i)}
 \end{aligned}
 \tag{B.29}$$

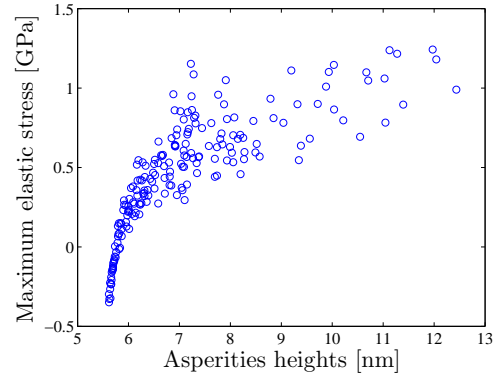
where n_{asp} is the number of asperities identified, see Appendix B.2, $A^{(i)}$ is the physical contact area of i -th asperity evaluated using Hertz model, $\sigma_{z,max}^{(i)}$ is the maximum normal stress of i -th asperity given by Eq. (B.26), and $\mathbb{1}_{>0}(\sigma_{z,max}^{(i)} - 0.6\sigma_H) = 1$ if $\sigma_{z,max}^{(i)} > 0.6\sigma_H$ and zero otherwise. When $A_p/A < 0.02$ the plasticity is negligible.

B.3.2 Application to the considered surfaces

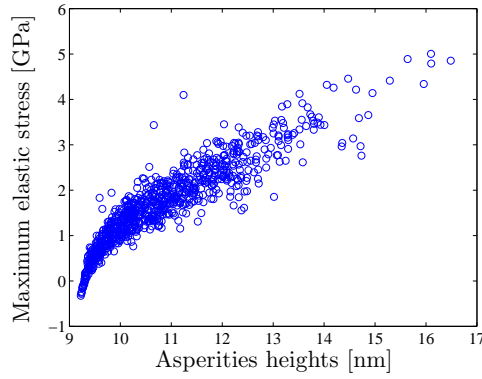
The equivalent surfaces of pairs I, II, a, b, and c, see Tab. 3.4 are considered here. The maximum stress for each identified asperity for these cases are illustrated in Fig B.4. Note that for each pair the contact distances at which the adhesion behaviors are important are beyond the chosen contact distance to study the contribution of plastic deformation, see Figs. 3.7, 3.8, and 3.10. Because the larger the contact distance the smaller the asperity interference, and the smaller the maximum stress, see Eq. (B.26), the maximum stress illustrated are considered as the worst cases. The hardness of the considered material (poly)silicon is $\sigma_H = 12.8$ GPa. As it is observed from Fig B.4, in all the cases, the maximum stresses are smaller than $0.6\sigma_H = 7.7$ GPa. In other words, the areas A_p are zero. Therefore, the negligibility of the irreversible deformation is confirmed. When using the GW model, the plasticity index is reported in Tab. B.1. Following GW model, the plasticity deformation in the cases of pairs I, II, and c is not negligible. However, it is not the case when using the semi-analytical contact model. It is explained by the disadvantages of the GW model, e.g. the radii of contacting asperities are underestimated when being approximated by the local summit radii, and consequently, the maximum stress given by Eq. (B.26) is overestimated.



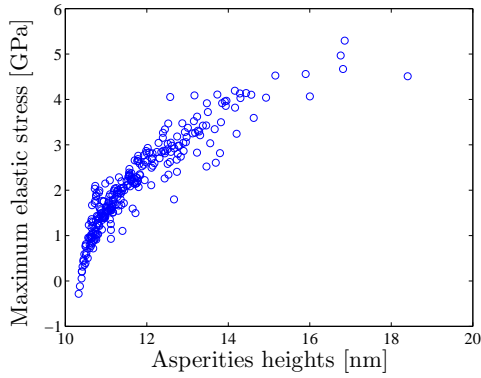
(a) Pair a, generated surfaces



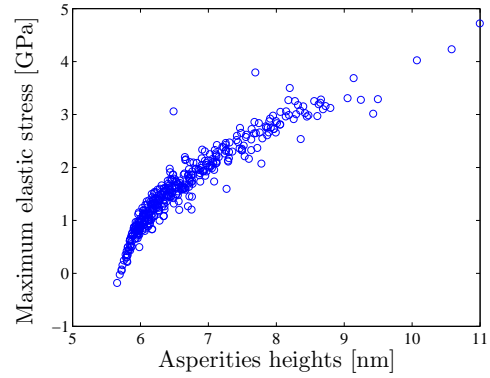
(b) Pair b, generated surfaces



(c) Pair c, generated surfaces



(d) Pair I, S1A vs flat surface



(e) Pair II, S2A vs flat surface

Figure B.4: The maximum elastic stress evaluated by Eq. (B.26) for the identified contacting asperities in the cases: (a) pair a with contact distance $\bar{d}=2.2$ nm; (b) pair b with contact distance $\bar{d}=5.7$ nm; (c) pair c with contact distance $\bar{d}=9$ nm; (d) pair I with contact distance $\bar{d}=10.2$ nm; and (e) pair II with contact distance $\bar{d}=5.7$ nm.

Appendix C

Appendices to Chapter 4

C.1 Legendre polynomials

Let $P^{(n)}$ be the n -order Legendre polynomials in one dimension. These polynomials are given by the Bonnet recursion formula as

$$P^{(0)}(x) = 1, \quad P^{(1)}(x) = x, \quad \text{with } x \in [-1, 1], \quad (\text{C.1})$$

$$(n+1)P^{(n+1)}(x) = (2n+1)xP^{(n)}(x) - nP^{(n-1)}(x), \quad \text{with } x \in [-1, 1]. \quad (\text{C.2})$$

These functions obey the orthogonality property

$$\int_{-1}^1 P^{(n)}(x)P^{(m)}(x)dx = \frac{2}{2n+1}\delta_{nm} \quad (\text{C.3})$$

In our case, the definition set is $\xi \in [0, 1]$ instead of $[-1, 1]$, and the polynomials must be normalized. The polynomials $\Psi^{(n)}$ are thus given from $P^{(n)}$ by

$$\Psi^{(n)}(\xi) = P^{(n)}(2\xi - 1)\sqrt{2n+1}. \quad (\text{C.4})$$

These polynomials, illustrated in Fig. 4.3, satisfy the normalized orthogonality condition, i.e.

$$\int_0^1 \Psi^{(n)}(\xi)\Psi^{(m)}(\xi)d\xi = \delta_{nm}. \quad (\text{C.5})$$

In the multidimensional case, i.e. $\boldsymbol{\xi} \in [0, 1]^{N_g}$, the Legendre polynomials are defined by

$$\Psi^{(n_1, n_2, \dots, n_{N_g})}(\boldsymbol{\xi}) = \Psi^{(n_1)}(\xi_1) \times \Psi^{(n_2)}(\xi_2) \times \dots \times \Psi^{(n_{N_g})}(\xi_{N_g}). \quad (\text{C.6})$$

The Legendre polynomials Ψ_α used in the truncated N_d -order gPCE described in Eq. (4.16) are given by

$$\Psi_\alpha \in \left\{ \Psi^{(n_1, n_2, \dots, n_{N_g})} : \sum_1^{N_g} n_i \leq N_d \right\}. \quad (\text{C.7})$$

The number of polynomials Ψ_α is $\binom{N_d + N_g}{N_g} = (N_d + N_g)!/N_d!/N_g!$.

C.2 Multivariate kernel density estimation

C.2.1 Evaluation of the probability density function

From the m explicitly evaluated vectors $\{\mathbf{q}^{(1)}, \dots, \mathbf{q}^{(m)}\}$, m full dimension vector samples $\{\boldsymbol{\eta}^{(1)}, \dots, \boldsymbol{\eta}^{(m)}\}$ and their corresponding reduced dimension vector samples $\{\tilde{\boldsymbol{\eta}}^{(1)}, \dots, \tilde{\boldsymbol{\eta}}^{(m)}\}$ are evaluated using Eqs. (4.12, 4.13). Using m samples $\{\tilde{\boldsymbol{\eta}}^{(1)}, \dots, \tilde{\boldsymbol{\eta}}^{(m)}\}$, the probability density function $p_{\tilde{\mathbf{H}}}$ of the random vector $\tilde{\mathbf{H}}$ can be approximated by $\hat{p}_{\tilde{\mathbf{H}}}$ evaluated using the MKDE method [112] as

$$p_{\tilde{\mathbf{H}}}(\tilde{\boldsymbol{\eta}}) \approx \hat{p}_{\tilde{\mathbf{H}}}(\tilde{\boldsymbol{\eta}}) = \frac{1}{m} \sum_{k=1}^m \mathbb{K}_{[B]}(\tilde{\boldsymbol{\eta}} - \tilde{\boldsymbol{\eta}}^{(k)}), \quad (\text{C.8})$$

where \mathbb{K} is the kernel function and $[B]$ is the $N_g \times N_g$ bandwidth matrix. A convenient choice for the kernel function is the multivariate normal distribution function $\mathcal{N}(\mathbf{0}, [B])$ with $[B]$ its covariance matrix,

$$\mathbb{K}_{[B]}(\tilde{\boldsymbol{\eta}} - \tilde{\boldsymbol{\eta}}^{(k)}) = \frac{1}{(2\pi)^{N_g/2} \sqrt{|[B]|}} \exp\left(-\frac{1}{2}(\tilde{\boldsymbol{\eta}} - \tilde{\boldsymbol{\eta}}^{(k)})^T [B]^{-1} (\tilde{\boldsymbol{\eta}} - \tilde{\boldsymbol{\eta}}^{(k)})\right), \quad (\text{C.9})$$

where $|[B]|$ is the determinant of the bandwidth matrix $[B]$. To define the bandwidth matrix, one can use the thumb-up rule proposed by Scott [112] for which the bandwidth matrix $[B]$ is a diagonal matrix given by

$$[B] = m \frac{-2}{N_g + 4} [C_{\tilde{\mathbf{H}}}] = m \frac{-2}{N_g + 4} I_{N_g}, \quad (\text{C.10})$$

where $[C_{\tilde{\mathbf{H}}}] = I_{N_g}$, and N_g is the dimension of the vector $\tilde{\boldsymbol{\eta}}$. With this choice of the kernel function, Eq. (C.8) is rewritten as

$$p_{\tilde{\mathbf{H}}}(\tilde{\boldsymbol{\eta}}) \approx \hat{p}_{\tilde{\mathbf{H}}}(\tilde{\boldsymbol{\eta}}) = \frac{1}{m} \sum_{k=1}^m \frac{1}{(2\pi)^{N_g/2} m^{-N_g/(N_g+4)}} \exp\left(-\frac{1}{2} \times \frac{\|\tilde{\boldsymbol{\eta}} - \tilde{\boldsymbol{\eta}}^{(k)}\|^2}{m^{-2/(N_g+4)}}\right). \quad (\text{C.11})$$

It can be proved that $\hat{p}_{\tilde{\mathbf{H}}}(\tilde{\boldsymbol{\eta}}) \xrightarrow{m \rightarrow +\infty} p_{\tilde{\mathbf{H}}}$ [112].

The conditional probability density functions are defined by

$$p_{\tilde{\mathbf{H}}}(\eta_k | \eta_{k-1}, \dots, \eta_1) = \frac{p_{\tilde{\mathbf{H}}}(\eta_1, \eta_2, \dots, \eta_k)}{\int_{\mathfrak{R}} p_{\tilde{\mathbf{H}}}(\eta_1, \eta_2, \dots, \eta_k) d\eta_k}, \quad \text{with } 1 \leq k \leq N_g. \quad (\text{C.12})$$

Using MKDE method, these conditional probability density functions are approximated as

$$\hat{p}_{\tilde{\mathbf{H}}}(\eta_k | \eta_{k-1}, \dots, \eta_1) = \frac{\hat{p}_{\tilde{\mathbf{H}}}(\eta_1, \eta_2, \dots, \eta_k)}{\int_{\mathfrak{R}} \hat{p}_{\tilde{\mathbf{H}}}(\eta_1, \eta_2, \dots, \eta_k) d\eta_k}, \quad \text{with } 1 \leq k \leq N_g. \quad (\text{C.13})$$

C.2.2 Evaluation of the inverse CDFs

The CDFs are evaluated as

$$\widehat{\mathbb{C}}_{\tilde{\mathbf{H}}}(\eta_k | \eta_{k-1}, \dots, \eta_1) = \int_{-\infty}^{\eta_k} \hat{\mathbb{P}}_{\tilde{\mathbf{H}}}(\eta_k = x | \eta_{k-1}, \dots, \eta_1) dx, \quad \text{with } 1 \leq k \leq N_g, \quad (\text{C.14})$$

where $\hat{\mathbb{P}}_{\tilde{\mathbf{H}}}(\eta_k | \eta_{k-1}, \dots, \eta_1)$ is obtained using Eq. (C.13). To evaluate the inverse CDFs, the linear interpolation technique is applied. Using Eq. (C.14), the CDFs are evaluated at a finite number of discrete points as

$$y_i \equiv \widehat{\mathbb{C}}_{\tilde{\mathbf{H}}}(\eta_k^{(i)} | \eta_{k-1}, \dots, \eta_1), \quad (\text{C.15})$$

where $\eta_k^{(i)} = \eta_k^{(0)} + i\Delta_\eta$ with $\{i = 0, \dots, \kappa\}$ and Δ_η is a positive interval. Owing to the properties of the CDF, we have $0 < y_0 < \dots < y_\kappa < 1$. The inverse CDFs are evaluated as

$$\widehat{\mathbb{C}}_{\tilde{\mathbf{H}}}^{-1}(\xi_k | \eta_{k-1}, \dots, \eta_1) = \eta_k^{(i)} + (\xi_k - y_i) \frac{\eta_k^{(i+1)} - \eta_k^{(i)}}{y_{i+1} - y_i}, \quad \text{with } i : y_i \leq \xi_k \leq y_{i+1}. \quad (\text{C.16})$$

The illustration of the Eq. (C.16) is shown in Fig. C.1.

The integration involved in Eqs. (C.13, C.14) are performed using the rectangle rule as

$$\begin{aligned} \int_{\mathfrak{R}} \hat{\mathbb{P}}_{\tilde{\mathbf{H}}}(\eta_1, \eta_2, \dots, \eta_k) d\eta_k &\simeq \sum_{i=1}^{\kappa} \hat{\mathbb{P}}_{\tilde{\mathbf{H}}}(\eta_1, \eta_2, \dots, \eta_k^{(i)}) \Delta_\eta \\ \int_{-\infty}^{\eta_k^{(i)}} \hat{\mathbb{P}}_{\tilde{\mathbf{H}}}(\eta_k = x | \eta_{k-1}, \dots, \eta_1) dx &\simeq \sum_{j=1}^i \hat{\mathbb{P}}_{\tilde{\mathbf{H}}}(\eta_k^{(j)} | \eta_{k-1}, \dots, \eta_1) \Delta_\eta, \end{aligned} \quad (\text{C.17})$$

where $\hat{\mathbb{P}}_{\tilde{\mathbf{H}}}(\eta_1, \eta_2, \dots, \eta_k^{(i)})$ is computed from Eq. (C.13).

Note that the inverse CDFs are only required to be evaluated at the Gauss quadrature integral points when evaluating the coefficients of the gPCE, see Eq. (4.29).

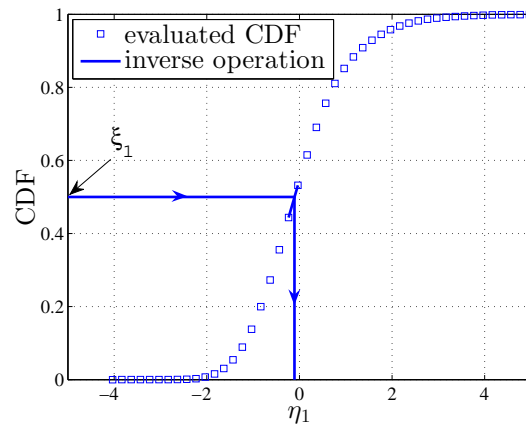


Figure C.1: The inverse process applied on CDFs using Eq. (C.16). The case of $\mathbb{C}_{\tilde{\mathbf{H}}}(\eta_1)$ for pair b at $RH = 65\%$ is illustrated.

Appendix D

Appendices to Chapter 5

D.1 Euler-Bernoulli beam theory and its 1D FE model

D.1.1 Theory

The Euler-Bernoulli beam theory implies that the cross section remains planar and normal to the neutral fiber after deformation, see Fig. D.1. In other words, the transverse shear and transverse normal effects are neglected. The theory results in the kinematic equations [107]

$$\begin{aligned}u_1(x_1, x_3) &= -x_3 \frac{\partial u_3}{\partial x_1}, \\u_3(x_1, x_3) &= u_3(x_1, 0),\end{aligned}\tag{D.1}$$

where u_1 , u_3 are the displacements of the beam neutral fiber along two directions x_1 and x_3 , the x_1 -, x_2 - and x_3 -coordinates are taken along the length of the beam, its width, and its thickness respectively, see Fig. D.1. Note that the displacement of the beam along the direction x_2 is assumed to be zero.

The strain and stress derived from the displacement field given by Eq. (D.1) is stated as

$$\epsilon_{11} = \frac{\partial u_1}{\partial x_1} = -x_3 \frac{\partial^2 u_3}{\partial x_1^2}, \quad \sigma_{11} = E\epsilon_{11}.\tag{D.2}$$

The balance of the momentum derived from the displacement field Eq. (D.1) is stated as

$$M(x_1) = \int_A \sigma_{11} x_3 dA = -EI \frac{\partial^2 u_3}{\partial x_1^2}; \quad Q(x_1) = \frac{\partial M}{\partial x_1}; \quad \frac{\partial Q}{\partial x_1} = -f;\tag{D.3}$$

where $I = \int_A x_3^2 dA$ is the moment area of the beam, A is the beam cross section, and f is the normal external forces. For the case of a rectangular beam cross section considered in this work, $I = \frac{1}{12}wt^3$. The balance of momentum results in the following governing

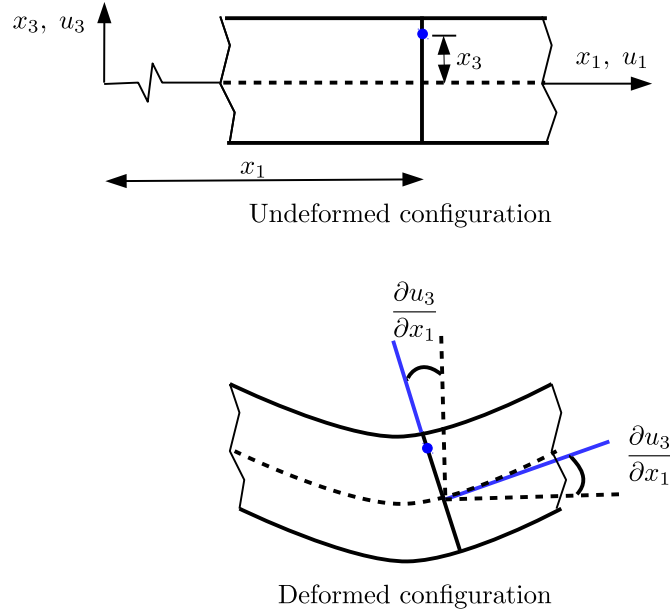


Figure D.1: Undeformed beam configuration and deformed beam configuration following the Euler-Bernoulli beam theory.

equation

$$EI \frac{\partial^4 u_3}{\partial x_1^4} = f. \quad (\text{D.4})$$

D.1.2 Development of the FE formulation

In this section we summarize the development of the FE formulation, for the particular case of Euler-Bernoulli beam theory. Let us consider a 1D beam element bounded by $[x_1^{(0)}, x_1^{(end)}]$ where $x_1^{(0)}, x_1^{(end)}$ are the coordinates of the beginning and ending nodes of the element. The governing equation given by Eq. (D.4) suggests that the lowest order approximation of the displacement field u_3 is the Hermite cubic interpolation such that

$$u_3(x_1) \approx u_3^h(x_1) = \sum_{i=1}^4 \Psi^{\text{FE},i}(x_1) u^{e,i}, \quad (\text{D.5})$$

where $u^{e,i}$ are the nodal displacements and rotations given as

$$u^{e,1} = u_3(x_1^{(0)}), \quad u^{e,2} = \frac{\partial u_3}{\partial x_1}(x_1^{(0)}), \quad u^{e,3} = u_3(x_1^{(end)}), \quad u^{e,4} = \frac{\partial u_3}{\partial x_1}(x_1^{(end)}), \quad (\text{D.6})$$

and $\Psi^{\text{FE},i}$ are the Hermitian cubic shape functions given by

$$\begin{aligned}\Psi^{\text{FE},1} &= (1 - 3\xi^2 + 2\xi^3), \\ \Psi^{\text{FE},2} &= l_e \xi (1 - \xi)^2, \\ \Psi^{\text{FE},3} &= \xi^2 (3 - 2\xi), \\ \Psi^{\text{FE},4} &= l_e \xi^2 (1 - \xi),\end{aligned}\tag{D.7}$$

where $l_e = x_1^{(\text{end})} - x_1^{(0)}$ is the element length, and $\xi = (x_1 - x_1^{(0)})/l_e$. Applying the variational technique on the governing Eq. (D.4) and using the FE approximation of the displacement field given by Eq. (D.5), the FE formulation in terms of the nodal displacements and rotations is obtained following [107] as

$$[K^e]\{\mathbf{u}^e\} = \{\mathbf{f}^e\},\tag{D.8}$$

where $\{\mathbf{u}^e\} = \{u^{e,1}, u^{e,2}, u^{e,3}, u^{e,4}\}$ is the nodal displacements and rotations vector, $\{\mathbf{f}^e\} = \{f^{e,1}, f^{e,2}, f^{e,3}, f^{e,4}\}$ is the equivalent nodal forces vector evaluated by

$$f^{e,i} = \int_{x_1^{(0)}}^{x_1^{(\text{end})}} f(x_1) \Psi^{\text{FE},i} dx_1,\tag{D.9}$$

and $[K^e]$ is the stiffness matrix given by

$$[K^e] = \frac{2EI}{l_e^3} \begin{bmatrix} 6 & 3l_e & -6 & 3l_e \\ 3l_e & 2l_e^2 & -3l_e & l_e^2 \\ -6 & -3l_e & 6 & -3l_e \\ 3l_e & l_e^2 & -3l_e & 2l_e^2 \end{bmatrix}.\tag{D.10}$$

D.2 Deterministic analysis of adhered cantilever beam

In this section, we report the relation between the crack length of an adhered cantilever beam, see Fig. 1.3(a), and the apparent adhesion energy, deduced in [87]. The deterministic problem is considered, i.e. the contact law is deterministic with a constant apparent adhesion energy \bar{e} , see Eq. (3.16). In [87], Mastragelo and Hsu assumed that the adhesive forces apply only in the range $l_s \leq x_1 \leq l$. Since there is no external force in the range $0 \leq x_1 \leq l_s$, the displacement of the beam neutral fiber is governed by

$$EI \frac{\partial^4 u_3}{\partial x_1^4} = 0, \quad \text{for } 0 \leq x_1 \leq l_s,\tag{D.11}$$

For S-shape beam, the boundary conditions are given by

$$\left. \frac{\partial u_3}{\partial x_1} \right|_0 = \left. \frac{\partial u_3}{\partial x_1} \right|_{x_1 \geq l_s} = 0, \quad u_3(0) = 0, \quad u_3(x_1 \geq l_s) = h,\tag{D.12}$$

where h is the gap between the beam and the substrate and l_s is the crack length. In this case, the Eq. (D.11) has the solution

$$u_3 = h \left(\frac{x_1}{l_s} \right)^2 \left(3 - 2 \frac{x_1}{l_s} \right), \quad \text{for } x_1 \leq l_s. \quad (\text{D.13})$$

The elastic energy stored in the beam is

$$\begin{aligned} U_E &= \frac{1}{2} \int_0^{l_s} \int_{-w/2}^{w/2} \int_{-t/2}^{t/2} \sigma_{11} \epsilon_{11} dx_3 dx_2 dx_1 \\ &= \frac{EI}{2} \int_0^{l_s} \left(\frac{\partial^2 u_3}{\partial x_1^2} \right)^2 dx_1 = \frac{6EIh^2}{l_s^3}. \end{aligned} \quad (\text{D.14})$$

Since the adhesive forces apply only in the range $l_s \leq x_1 \leq l$, the total adhesion energy is evaluated as

$$U_S = -\bar{e}w(l - l_s). \quad (\text{D.15})$$

The total energy is given by

$$U_T = U_E + U_S = \frac{6EIh^2}{l_s^3} - \bar{e}w(l - l_s). \quad (\text{D.16})$$

At the equilibrium configuration, $dU_T/dl_s = 0$, one gets

$$\bar{e} = 18 \frac{EIh^2}{wl_s^4} = \frac{3}{2} \frac{Et^3h^2}{l_s^4}. \quad (\text{D.17})$$

For an arc-shape configuration, with a similar process, the relation between the apparent adhesion energy and the crack length is obtained as [87]

$$\bar{e} = \frac{3}{8} \frac{Et^3h^2}{l_s^4}. \quad (\text{D.18})$$

Equations (D.17) and (D.18) are only applicable for deterministic problems. However, they are still useful in the non-deterministic cases to deduce the upper-scale apparent adhesive energies Γ , see Eqs. (5.13), (5.14).

D.2.1 Comparison between analytical and numerical solutions

Let us consider the deterministic problem for which the adhesive behavior between the beam bottom surface and the substrate is uniform. The adhesive behavior is modeled using one realization, illustrated in Fig. D.2(a), of the random apparent contact forces. The FE method developed in Chapter 5 is applied to evaluate the crack length and the apparent adhesion energy Γ given by Eq (5.13). As the problem is deterministic, the apparent adhesion energy Γ is the adhesion energy \bar{e} of the apparent adhesive contact force, see Fig. 4.1. The convergence analysis is achieved by comparing the FE prediction with the adhesion energy \bar{e} , as illustrated in Fig. D.2(b). With the element length $l_e = 7.5 \mu\text{m}$ and the meso-scale length $l_{\text{meso}} = 1.5 \mu\text{m}$, the numerical result predicts well the analytical one with a difference of 2.5%.

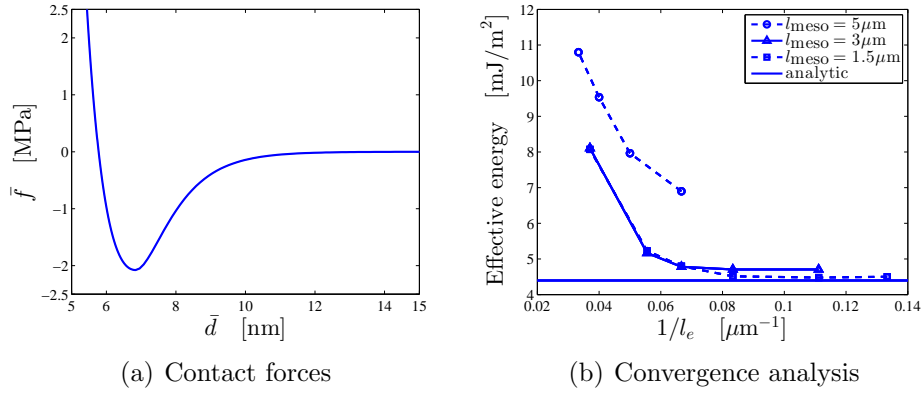


Figure D.2: Comparison between FE model results and analytical one. (a) The deterministic contact law extracted from the evaluated apparent contact forces of pair b at $RH = 0.65$, see Fig. 3.10(d). (b) The convergence analysis in terms of l_e and l_{meso} of the apparent adhesion energy for the cantilever beam.

Bibliography

- [1] ABRAMOWITZ, M., AND STEGUN, I. A. *Handbook of mathematical functions: with formulas, graphs, and mathematical tables*, vol. 55. Courier Corporation, 1964.
- [2] ADAMSON, A. W., AND GAST, A. P. *Physical chemistry of surfaces*. Interscience New York, 1967.
- [3] ADLER, R. J. *Random Fields and Geometry*. Springer New York, New York, NY, 2007.
- [4] ADLER, R. J. *The geometry of random fields*. SIAM, 2010.
- [5] AGMON, N., ALHASSID, Y., AND LEVINE, R. D. An algorithm for finding the distribution of maximal entropy. *Journal of Computational Physics* 30, 2 (1979), 250–258.
- [6] ARCHARD, J. F. Elastic deformation and the laws of friction. *Proceedings of the Royal Society of London. Series A. Mathematical and Physical Sciences* 243, 1233 (1957), 190–205.
- [7] ARDITO, R., BALDASARRE, L., CORIGLIANO, A., DE MASI, B., FRANGI, A., AND MAGAGNIN, L. Experimental evaluation and numerical modeling of adhesion phenomena in polysilicon mems. *Meccanica* 48, 8 (Oct 2013), 1835–1844.
- [8] ARDITO, R., CORIGLIANO, A., AND FRANGI, A. Modelling of spontaneous adhesion phenomena in micro-electro-mechanical systems. *European Journal of Mechanics - A/Solids* 39, 0 (2013), 144 – 152.
- [9] ARDITO, R., CORIGLIANO, A., FRANGI, A., AND RIZZINI, F. Advanced models for the calculation of capillary attraction in axisymmetric configurations. *European Journal of Mechanics - A/Solids* 47, 0 (2014), 298 – 308.
- [10] ARNST, M., GHANEM, R., AND SOIZE, C. Identification of bayesian posteriors for coefficients of chaos expansions. *Journal of Computational Physics* 229, 9 (2010), 3134–3154.

- [11] ASAY, D. B., AND KIM, S. H. Evolution of the adsorbed water layer structure on silicon oxide at room temperature. *The Journal of Physical Chemistry B* 109, 35 (2005), 16760–16763.
- [12] AUTUMN, K., SITTI, M., LIANG, Y. A., PEATTIE, A. M., HANSEN, W. R., SPONBERG, S., KENNY, T. W., FEARING, R., ISRAELACHVILI, J. N., AND FULL, R. J. Evidence for van der Waals adhesion in gecko setae. *Proceedings of the National Academy of Sciences* 99, 19 (2002), 12252–12256.
- [13] BERRY, M., AND LEWIS, Z. On the Weierstrass-Mandelbrot fractal function. In *Proceedings of the Royal Society of London A: Mathematical, Physical and Engineering Sciences* (1980), vol. 370, The Royal Society, pp. 459–484.
- [14] BHUSHAN, B. Adhesion and stiction: mechanisms, measurement techniques, and methods for reduction. *Journal of Vacuum Science & Technology B* 21, 6 (2003), 2262–2296.
- [15] BHUSHAN, B., ISRAELACHVILI, J. N., AND LANDMAN, U. Nanotribology: friction, wear and lubrication at the atomic scale. *Nature* 374 (1995), 13.
- [16] BHUSHAN, B., AND JUNG, Y. C. Wetting, adhesion and friction of superhydrophobic and hydrophilic leaves and fabricated micro/nanopatterned surfaces. *Journal of Physics: Condensed Matter* 20, 22 (2008), 225010.
- [17] BILLINGSLEY, P. *Probability and measure*. John Wiley & Sons, 2008.
- [18] BRYZEK, J. Impact of mems technology on society. *Sensors and Actuators A: Physical* 56, 1 (1996), 1 – 9.
- [19] BURTON, Z., AND BHUSHAN, B. Hydrophobicity, adhesion, and friction properties of nanopatterned polymers and scale dependence for micro-and nanoelectromechanical systems. *Nano letters* 5, 8 (2005), 1607–1613.
- [20] BUSH, A., GIBSON, R., AND THOMAS, T. The elastic contact of a rough surface. *Wear* 35, 1 (1975), 87 – 111.
- [21] CAI, S., AND BHUSHAN, B. Meniscus and viscous forces during separation of hydrophilic and hydrophobic surfaces with liquid-mediated contacts. *Materials Science and Engineering: R: Reports* 61, 1 (2008), 78–106.
- [22] CAPPELLA, B., AND DIETLER, G. Force-distance curves by atomic force microscopy. *Surface science reports* 34, 1 (1999), 1–104.
- [23] CHA, P.-R., SROLOVITZ, D. J., AND KYLE VANDERLICK, T. Molecular dynamics simulation of single asperity contact. *Acta Materialia* 52, 13 (2004), 3983 – 3996.

- [24] CHILAMAKURI, S., AND BHUSHAN, B. Contact analysis of non-Gaussian random surfaces. *Proceedings of the Institution of Mechanical Engineers, Part J: Journal of Engineering Tribology* 212, 1 (1998), 19–32.
- [25] CLÉMENT, A., SOIZE, C., AND YVONNET, J. Computational nonlinear stochastic homogenization using a nonconcurrent multiscale approach for hyperelastic heterogeneous microstructures analysis. *International Journal for Numerical Methods in Engineering* 91, 8 (2012), 799–824.
- [26] CLÉMENT, A., SOIZE, C., AND YVONNET, J. Uncertainty quantification in computational stochastic multiscale analysis of nonlinear elastic materials. *Computer Methods in Applied Mechanics and Engineering* 254 (2013), 61–82.
- [27] DA PRATO, G., AND ZABCZYK, J. *Stochastic equations in infinite dimensions*. Cambridge university press, 2014.
- [28] DAS, S., GHANEM, R., AND FINETTE, S. Polynomial chaos representation of spatio-temporal random fields from experimental measurements. *Journal of Computational Physics* 228, 23 (2009), 8726 – 8751.
- [29] DE BOER, M. Capillary adhesion between elastically hard rough surfaces. *Experimental Mechanics* 47 (2007), 171–183.
- [30] DE BOER, M., AND DE BOER, P. Thermodynamics of capillary adhesion between rough surfaces. *Journal of Colloid and Interface Science* 311, 1 (2007), 171 – 185.
- [31] DE BOER, M. P., AND MICHALSKE, T. A. Accurate method for determining adhesion of cantilever beams. *Journal of Applied Physics* 86, 2 (1999), 817.
- [32] DELRIO, F. W., DUNN, M. L., AND DE BOER, M. P. Van der Waals and capillary adhesion of polycrystalline silicon micromachined surfaces. In *Scanning Probe Microscopy in Nanoscience and Nanotechnology 3*, B. Bhushan, Ed., NanoScience and Technology. Springer Berlin Heidelberg, 2013, pp. 363–393.
- [33] DERJAGUIN, B., MULLER, V., AND TOPOROV, Y. Effect of contact deformations on the adhesion of particles. *Journal of Colloid and Interface Science* 53, 2 (1975), 314 – 326.
- [34] DESCELIERS, C., GHANEM, R., AND SOIZE, C. Maximum likelihood estimation of stochastic chaos representations from experimental data. *International Journal for Numerical Methods in Engineering* 66, 6 (2006), 978–1001.
- [35] DZIALOSHINSKII, I. E., LIFSHITZ, E., AND PITAEVSKII, L. P. General theory of van der Waals’ forces. *Soviet Physics Uspekhi* 4, 2 (1961), 153–176.
- [36] FEYNMAN, R. P. There’s plenty of room at the bottom. *Engineering and science* 23, 5 (1960), 22–36.

- [37] FODOR, I. K. A survey of dimension reduction techniques, 2002.
- [38] GEERS, M., KOUZNETSOVA, V., AND BREKELMANS, W. Multi-scale computational homogenization: Trends and challenges. *Journal of Computational and Applied Mathematics* 234, 7 (2010), 2175 – 2182. Fourth International Conference on Advanced COmputational Methods in ENgineering (ACOMEN 2008).
- [39] GHANEM, R. G., AND SPANOS, P. D. *Stochastic finite elements: a spectral approach*. Courier Corporation, 2003.
- [40] GOLDBERG, D. E., AND HOLLAND, J. H. Genetic algorithms and machine learning. *Machine learning* 3, 2 (1988), 95–99.
- [41] GREENWOOD, J., AND WU, J. Surface roughness and contact: An apology. *Meccanica* 36, 6 (2001), 617–630.
- [42] GREENWOOD, J. A., AND WILLIAMSON, J. B. P. Contact of nominally flat surfaces. *Proceedings of the Royal Society of London. Series A. Mathematical and Physical Sciences* 295, 1442 (1966), 300–319.
- [43] GRIGORIU, M. *Stochastic calculus: applications in science and engineering*. Springer Science & Business Media, 2013.
- [44] GRIMMETT, G., AND STIRZAKER, D. *Probability and random processes*. Oxford university press, 2001.
- [45] GUILLEMINOT, J., AND SOIZE, C. Non-Gaussian positive-definite matrix-valued random fields with constrained eigenvalues: Application to random elasticity tensors with uncertain material symmetries. *International Journal for Numerical Methods in Engineering* 88, 11 (2011), 1128–1151.
- [46] HAMAKER, H. The London–van der Waals attraction between spherical particles. *Physica* 4, 10 (1937), 1058–1072.
- [47] HARIRI, A., ZU, J., AND MRAD, R. B. Modeling of wet stiction in microelectromechanical systems (mems). *Journal of microelectromechanical systems* 16, 5 (2007), 1276–1285.
- [48] HERTZ, H. Ueber die berührung fester elastischer körper. *Journal für die reine und angewandte Mathematik* 92 (1882), 156–171.
- [49] HILL, R. Elastic properties of reinforced solids: some theoretical principles. *Journal of the Mechanics and Physics of Solids* 11, 5 (1963), 357–372.
- [50] HOANG, T.-V. Capillary effects on stiction in mems (master thesis). Master’s thesis, Université de Liège, 2013.

- [51] HOWE, R. T., AND MULLER, R. S. Resonant-microbridge vapor sensor. *IEEE Transactions on Electron Devices* 33, 4 (1986), 499–506.
- [52] ISRAELACHVILI, J. N. *Intermolecular and surface forces*. Academic press, 2011.
- [53] JACKSON, J. E. *A user's guide to principal components*, vol. 587. John Wiley & Sons, 2005.
- [54] JAYNES, E. T. Information theory and statistical mechanics. *Physical review* 106, 4 (1957), 620–630.
- [55] JENSEN, B. D., DE BOER, M., MASTERS, N., BITSIE, F., AND LAVAN, D. A. Interferometry of actuated microcantilevers to determine material properties and test structure nonidealities in mems. *Microelectromechanical Systems, Journal of* 10, 3 (Sep 2001), 336–346.
- [56] JOHNSON, K. L., AND JOHNSON, K. L. *Contact mechanics*. Cambridge university press, 1987.
- [57] JOHNSON, K. L., KENDALL, K., AND ROBERTS, A. D. Surface energy and the contact of elastic solids. *Proceedings of the Royal Society of London. A. Mathematical and Physical Sciences* 324, 1558 (1971), 301–313.
- [58] JOLLIFFE, I. *Principal component analysis*. Wiley Online Library, 2002.
- [59] JUDY, J. W. Microelectromechanical systems (mems): fabrication, design and applications. *Smart materials and Structures* 10, 6 (2001), 1115.
- [60] JUNG, Y. C., AND BHUSHAN, B. Contact angle, adhesion and friction properties of micro-and nanopatterned polymers for superhydrophobicity. *Nanotechnology* 17, 19 (2006), 4970.
- [61] KAC, M., AND SIEGERT, A. An explicit representation of a stationary Gaussian process. *The Annals of Mathematical Statistics* 18, 3 (1947), 438–442.
- [62] KARHUNEN, K. *Ueber lineare Methoden in der Wahrscheinlichkeitsrechnung*. Annales Academiae scientiarum Fennicae. Series A. 1, Mathematica-physica. 1947.
- [63] KIM, K.-S., McMEEKING, R., AND JOHNSON, K. Adhesion, slip, cohesive zones and energy fluxes for elastic spheres in contact. *Journal of the Mechanics and Physics of Solids* 46, 2 (1998), 243 – 266.
- [64] KIRKPATRICK, S., GELATT, C. D., VECCHI, M. P., ET AL. Optimization by simulated annealing. *science* 220, 4598 (1983), 671–680.
- [65] KNAPP, J. A., AND DE BOER, M. P. Mechanics of microcantilever beams subject to combined electrostatic and adhesive forces. *Journal of Microelectromechanical Systems* 11, 6 (2002), 754–764.

- [66] KOGUT, L., AND ETSION, I. Elastic-plastic contact analysis of a sphere and a rigid flat. *Journal of applied Mechanics* 69, 5 (2002), 657–662.
- [67] KOGUT, L., AND ETSION, I. Adhesion in elastic–plastic spherical microcontact. *Journal of Colloid and Interface Science* 261, 2 (2003), 372–378.
- [68] LE MAÎTRE, O., AND KNIO, O. M. *Spectral methods for uncertainty quantification: with applications to computational fluid dynamics*. Springer Science & Business Media, 2010.
- [69] LEVINE, R. D., AND TRIBUS, M. Maximum entropy formalism. In *Maximum Entropy Formalism Conference (1978: Massachusetts Institute of Technology)* (1979), Mit Press.
- [70] LIEBSCHER, A., PROPPE, C., REDENBACH, C., AND SCHWARZER, D. Uncertainty quantification for metal foam structures by means of image analysis. *Probabilistic Engineering Mechanics* 28 (2012), 143–151.
- [71] LIU, J. S. *Monte Carlo strategies in scientific computing*. Springer Science & Business Media, 2008.
- [72] LOEVE, M. *Fonctions aléatoires du second ordre*. In: *Lvy, P. (ed.) Processus Stochastique et Mouvement Brownien*. Gauthier Villars, Paris, 1965.
- [73] LOÈVE, M. Elementary probability theory. In *Probability Theory I*. Springer, 1977, pp. 1–52.
- [74] LUAN, B., AND ROBBINS, M. O. Contact of single asperities with varying adhesion: comparing continuum mechanics to atomistic simulations. *Physical Review E* 74, 2 (2006), 026111.
- [75] LUCAS, V., GOLINVAL, J.-C., PAQUAY, S., NGUYEN, V.-D., NOELS, L., AND WU, L. A stochastic computational multiscale approach; application to mems resonators. *Computer Methods in Applied Mechanics and Engineering* 294 (2015), 141–167.
- [76] LUCAS, V., GOLINVAL, J.-C., VOICU, R., DANILA, M., GAVRILA, R., MÜLLER, R., DINESCU, A., NOELS, L., AND WU, L. Propagation of material and surface profile uncertainties on mems micro-resonators using a stochastic second-order computational multi-scale approach. *International Journal for Numerical Methods in Engineering* (2017).
- [77] MA, J., SAHRAEE, S., WRIGGERS, P., AND DE LORENZIS, L. Stochastic multiscale homogenization analysis of heterogeneous materials under finite deformations with full uncertainty in the microstructure. *Computational Mechanics* 55, 5 (2015), 819–835.

- [78] MABOUDIAN, R. Surface processes in mems technology. *Surface Science Reports* 30, 6 (1998), 207 – 269.
- [79] MAJUMDAR, A., AND BHUSHAN, B. Role of fractal geometry in roughness characterization and contact mechanics of surfaces. *ASME J. Tribol* 112, 2 (1990), 205–216.
- [80] MAJUMDAR, A., AND TIEN, C. Fractal characterization and simulation of rough surfaces. *Wear* 136, 2 (1990), 313–327.
- [81] MALUF, N., AND WILLIAMS, K. *Introduction to microelectromechanical systems engineering*. Artech House, 2004.
- [82] MANDELBROT, B. B. *The fractal geometry of nature*. WH freeman New York, 1982.
- [83] MARIANI, S., GHISI, A., CORIGLIANO, A., MARTINI, R., AND SIMONI, B. Two-scale simulation of drop-induced failure of polysilicon mems sensors. *Sensors* 11, 5 (2011), 4972–4989.
- [84] MARIANI, S., GHISI, A., CORIGLIANO, A., AND ZERBINI, S. Multi-scale analysis of mems sensors subject to drop impacts. *Sensors* 7, 9 (2007), 1817–1833.
- [85] MARIANI, S., MARTINI, R., GHISI, A., CORIGLIANO, A., AND BEGHI, M. Overall elastic properties of polysilicon films: A statistical investigation of the effects of polycrystal morphology. *International Journal for Multiscale Computational Engineering* 9, 3 (2011).
- [86] MARIANI, S., MARTINI, R., GHISI, A., CORIGLIANO, A., AND SIMONI, B. Monte carlo simulation of micro-cracking in polysilicon mems exposed to shocks. *International Journal of Fracture* 167, 1 (2011), 83–101.
- [87] MASTRANGELO, C., AND HSU, C. A simple experimental technique for the measurement of the work of adhesion of microstructures. In *Solid-State Sensor and Actuator Workshop, 1992. 5th Technical Digest., IEEE* (June 1992), pp. 208–212.
- [88] MASTRANGELO, C., AND HSU, C. Mechanical stability and adhesion of microstructures under capillary forces. i. basic theory. *Journal of Microelectromechanical systems* 2, 1 (1993), 33–43.
- [89] MASTRANGELO, C. H., AND HSU, C. Mechanical stability and adhesion of microstructures under capillary forces. ii. experiments. *Journal of Microelectromechanical Systems* 2, 1 (1993), 44–55.
- [90] MAUGIS, D. Adhesion of spheres: The JKR-DMT transition using a dugdale model. *Journal of Colloid and Interface Science* 150, 1 (1992), 243 – 269.

- [91] MAUGIS, D., AND GAUTHIER-MANUEL, B. JKR-DMT transition in the presence of a liquid meniscus. *Journal of Adhesion Science and Technology* 8, 11 (1994), 1311–1322.
- [92] MCKAY, M. D., BECKMAN, R. J., AND CONOVER, W. J. A comparison of three methods for selecting values of input variables in the analysis of output from a computer code. *Technometrics* 42, 1 (2000), 55–61.
- [93] MULAY, S. S., BECKER, G., VAYRETTE, R., RASKIN, J.-P., PARDOEN, T., GALCERAN, M., GODET, S., AND NOELS, L. Multiscale modelling framework for the fracture of thin brittle polycrystalline films: application to polysilicon. *Computational Mechanics* 55, 1 (2015), 73–91.
- [94] NAYAK, P. R. Random process model of rough surfaces. *Journal of Tribology* 93, 3 (1971), 398–407.
- [95] NEWLAND, D. E. *An introduction to random vibrations, spectral & wavelet analysis*. Courier Corporation, 2012.
- [96] NYQUIST, H. Certain topics in telegraph transmission theory. *Transactions of the American Institute of Electrical Engineers* 47, 2 (1928), 617–644.
- [97] O'MARA, W., HERRING, R. B., AND HUNT, L. P. *Handbook of semiconductor silicon technology*. Crest Publishing House, 2007.
- [98] PARSEGHIAN, V. A. *Van der Waals forces: a handbook for biologists, chemists, engineers, and physicists*. Cambridge University Press, 2005.
- [99] PEARSON, K. Contributions to the mathematical theory of evolution. *Philosophical Transactions of the Royal Society of London. A* 185 (1894), 71–110.
- [100] PEI, L., HYUN, S., MOLINARI, J., AND ROBBINS, M. O. Finite element modeling of elasto-plastic contact between rough surfaces. *Journal of the Mechanics and Physics of Solids* 53, 11 (2005), 2385 – 2409.
- [101] PERSSON, B. Contact mechanics for randomly rough surfaces. *Surface Science Reports* 61, 4 (2006), 201 – 227.
- [102] PERSSON, B., ALBOHR, O., TARTAGLINO, U., VOLOKITIN, A., AND TOSATTI, E. On the nature of surface roughness with application to contact mechanics, sealing, rubber friction and adhesion. *Journal of Physics: Condensed Matter* 17, 1 (2004), R1.
- [103] POIRION, F., AND SOIZE, C. Numerical methods and mathematical aspects for simulation of homogeneous and non homogeneous Gaussian vector fields. In *Probabilistic Methods in Applied Physics*, P. Krée and W. Wedig, Eds., vol. 451 of *Lecture Notes in Physics*. Springer Berlin Heidelberg, 1995, pp. 17–53.

-
- [104] POPESCU, R., DEODATIS, G., AND PREVOST, J. H. Simulation of homogeneous nonGaussian stochastic vector fields. *Probabilistic Engineering Mechanics* 13, 1 (1998), 1–13.
- [105] PUIG, B., POIRION, F., AND SOIZE, C. Non-Gaussian simulation using hermite polynomial expansion: convergences and algorithms. *Probabilistic Engineering Mechanics* 17, 3 (2002), 253–264.
- [106] RAPAPORT, D. C., BLUMBERG, R. L., MCKAY, S. R., CHRISTIAN, W., ET AL. The art of molecular dynamics simulation. *Computers in Physics* 10, 5 (1996), 456–456.
- [107] REDDY, J. On locking-free shear deformable beam finite elements. *Computer Methods in Applied Mechanics and Engineering* 149, 14 (1997), 113 – 132. Containing papers presented at the Symposium on Advances in Computational Mechanics.
- [108] ROCKINGER, M., AND JONDEAU, E. Entropy densities with an application to autoregressive conditional skewness and kurtosis. *Journal of Econometrics* 106, 1 (2002), 119–142.
- [109] ROGERS, J. W., MACKIN, T. J., AND PHINNEY, L. M. A thermomechanical model for adhesion reduction of mems cantilevers. *Journal of Microelectromechanical Systems* 11, 5 (2002), 512–520.
- [110] ROSENBLATT, M. Remarks on a multivariate transformation. *The annals of mathematical statistics* (1952), 470–472.
- [111] SAVVAS, D., STEFANOY, G., AND PAPADRAKAKIS, M. Determination of rve size for random composites with local volume fraction variation. *Computer Methods in Applied Mechanics and Engineering* 305 (2016), 340–358.
- [112] SCOTT, D. W. *Multivariate density estimation: theory, practice, and visualization*. John Wiley & Sons, 2015.
- [113] SHANNON, C. E. A mathematical theory of communication. *Bell System Technical Journal* 27, 4 (1948), 623–656.
- [114] SHANNON, C. E. Communication in the presence of noise. *Proceedings of the IRE* 37, 1 (1949), 10–21.
- [115] SHINOZUKA, M. Simulation of multivariate and multidimensional random processes. *The Journal of the Acoustical Society of America* 49, 1B (1971), 357–368.
- [116] SOIZE, C. Non-Gaussian positive-definite matrix-valued random fields for elliptic stochastic partial differential operators. *Computer methods in applied mechanics and engineering* 195, 1 (2006), 26–64.

- [117] SOIZE, C. Tensor-valued random fields for meso-scale stochastic model of anisotropic elastic microstructure and probabilistic analysis of representative volume element size. *Probabilistic Engineering Mechanics* 23, 2 (2008), 307–323.
- [118] SOIZE, C. *Stochastic Models of Uncertainties in Computational Mechanics*. Lecture Notes in Mechanics. American Society of Civil Engineers, 2012.
- [119] SOIZE, C., AND GHANEM, R. Physical systems with random uncertainties: chaos representations with arbitrary probability measure. *SIAM Journal on Scientific Computing* 26, 2 (2004), 395–410.
- [120] SOYLEMEZ, E., AND DE BOER, M. P. Capillary-induced crack healing between surfaces of nanoscale roughness. *Langmuir* 30, 39 (2014), 11625–11633.
- [121] SOYLEMEZ, E., AND DE BOER, M. P. Crack healing between rough polycrystalline silicon hydrophilic surfaces in n-pentanol and water vapors. *Tribology Letters* 59, 1 (2015), 1–12.
- [122] SOYLEMEZ, E., AND DE BOER, M. P. van der Waals force-induced crack healing in dry rough interfaces. *Journal of Physics D: Applied Physics* 49, 7 (2016), 075303.
- [123] STEFANOY, G., SAVVAS, D., AND PAPADRAKAKIS, M. Stochastic finite element analysis of composite structures based on material microstructure. *Composite Structures* 132 (2015), 384–392.
- [124] SUH, A. Y., AND POLYCARPOU, A. A. Digital filtering methodology used to reduce scale of measurement effects in roughness parameters for magnetic storage supersmooth hard disks. *Wear* 260, 4 (2006), 538–548.
- [125] TABOR, D. *The hardness of metals*. Oxford university press, 2000.
- [126] TAS, N., SONNENBERG, T., JANSEN, H., LEGTENBERG, R., AND ELWEN-SPOEK, M. Stiction in surface micromachining. *Journal of Micromechanics and Microengineering* 6, 4 (1996), 385.
- [127] TEMIZER, İ., AND WRIGGERS, P. A multiscale contact homogenization technique for the modeling of third bodies in the contact interface. *Computer Methods in Applied Mechanics and Engineering* 198, 34 (2008), 377 – 396.
- [128] THOMAS, T., AND ROSÉN, B.-G. Determination of the optimum sampling interval for rough contact mechanics. *Tribology international* 33, 9 (2000), 601–610.
- [129] TIMPE, S. J., AND KOMVOPOULOS, K. An experimental study of sidewall adhesion in microelectromechanical systems. *Journal of microelectromechanical systems* 14, 6 (2005), 1356–1363.

- [130] TROVALUSCI, P., DE BELLIS, M. L., OSTOJA-STARZEWSKI, M., AND MURRALI, A. Particulate random composites homogenized as micropolar materials. *Meccanica* 49, 11 (2014), 2719–2727.
- [131] TROVALUSCI, P., OSTOJA-STARZEWSKI, M., DE BELLIS, M. L., AND MURRALI, A. Scale-dependent homogenization of random composites as micropolar continua. *European Journal of Mechanics-A/Solids* 49 (2015), 396–407.
- [132] UNSER, M. Sampling-50 years after shannon. *Proceedings of the IEEE* 88, 4 (2000), 569–587.
- [133] VAN SPENGEN, W. M. Mems reliability from a failure mechanisms perspective. *Microelectronics Reliability* 43, 7 (2003), 1049–1060.
- [134] VAN SPENGEN, W. M. A physical model to describe the distribution of adhesion strength in mems, or why one mems device sticks and another identical one does not. *Journal of Micromechanics and Microengineering* 25, 12 (2015), 125012.
- [135] VAN SPENGEN, W. M., PUERS, R., AND DE WOLF, I. A physical model to predict stiction in mems. *Journal of Micromechanics and Microengineering* 12, 5 (2002), 702.
- [136] VAN SPENGEN, W. M., PUERS, R., AND DE WOLF, I. On the physics of stiction and its impact on the reliability of microstructures. *Journal of Adhesion Science and Technology* 17, 4 (2003), 563–582.
- [137] WANG, W., AND SOPER, S. A. *Bio-MEMS: technologies and applications*. CRC press, 2006.
- [138] WHITEHOUSE, D. J., AND ARCHARD, J. F. The properties of random surfaces of significance in their contact. *Proceedings of the Royal Society of London A: Mathematical, Physical and Engineering Sciences* 316, 1524 (1970), 97–121.
- [139] WIENER, N. The homogeneous chaos. *American Journal of Mathematics* 60, 4 (1938), 897–936.
- [140] WILKS, S. S. The large-sample distribution of the likelihood ratio for testing composite hypotheses. *The Annals of Mathematical Statistics* 9, 1 (1938), 60–62.
- [141] WRIGGERS, P. Finite element algorithms for contact problems. *Archives of Computational Methods in Engineering* 2, 4 (1995), 1–49.
- [142] WRIGGERS, P., AND LAURSEN, T. A. *Computational contact mechanics*. Springer, 2006.
- [143] WRIGGERS, P., VAN, T. V., AND STEIN, E. Finite element formulation of large deformation impact-contact problems with friction. *Computers & Structures* 37, 3 (1990), 319 – 331.

- [144] WU, L., GOLINVAL, J.-C., AND NOELS, L. A micro-model for elasto-plastic adhesive contact in micro-switches: Application to cyclic loading. *Tribology International* 57, 0 (2013), 137 – 146.
- [145] WU, L., LUCAS, V., NGUYEN, V.-D., GOLINVAL, J.-C., PAQUAY, S., AND NOELS, L. A stochastic multi-scale approach for the modeling of thermo-elastic damping in micro-resonators. *Computer Methods in Applied Mechanics and Engineering* 310 (2016), 802–839.
- [146] WU, L., NOELS, L., ROCHUS, V., PUSTAN, M., AND GOLINVAL, J.-C. A micro - macro approach to predict stiction due to surface contact in micro electro-mechanical systems. *Journal of Microelectromechanical Systems* 20, 4 (2011), 976 –990.
- [147] WU, L., ROCHUS, V., NOELS, L., AND GOLINVAL, J. C. Influence of adhesive rough surface contact on microswitches. *Journal of Applied Physics* 106, 11 (2009), 113502.
- [148] XIU, D. *Numerical methods for stochastic computations: a spectral method approach*. Princeton University Press, 2010.
- [149] XIU, D., AND KARNIADAKIS, G. E. The Wiener–Askey polynomial chaos for stochastic differential equations. *SIAM journal on scientific computing* 24, 2 (2002), 619–644.
- [150] XUE, X., PHINNEY, L. M., AND POLYCARPOU, A. A. Asymmetric surface roughness measurements and meniscus modeling of polysilicon surface micromachined flaps. *Microsystem Technologies* 14, 1 (2008), 17.
- [151] XUE, X., POLYCARPOU, A. A., AND PHINNEY, L. M. Measurement and modeling of adhesion energy between two rough microelectromechanical system (mems) surfaces. *Journal of Adhesion Science and Technology* 22, 5-6 (2008), 429–455.
- [152] YAMAZAKI, F., AND SHINOZUKA, M. Digital generation of non-Gaussian stochastic fields. *Journal of Engineering Mechanics* 114, 7 (1988), 1183–1197.
- [153] YASTREBOV, V. A., DURAND, J., PROUDHON, H., AND CAILLETAUD, G. Rough surface contact analysis by means of the finite element method and of a new reduced model. *Comptes Rendus Mécanique* 339, 78 (2011), 473 – 490. Surface mechanics : facts and numerical models.
- [154] YIN, X., CHEN, W., TO, A., MCVEIGH, C., AND LIU, W. K. Statistical volume element method for predicting microstructure–constitutive property relations. *Computer methods in applied mechanics and engineering* 197, 43 (2008), 3516–3529.

-
- [155] YIN, X., LEE, S., CHEN, W., LIU, W. K., AND HORSTEMEYER, M. Efficient random field uncertainty propagation in design using multiscale analysis. *Journal of Mechanical Design* 131, 2 (2009), 021006.
- [156] YU, N., AND POLYCARPOU, A. A. Contact of rough surfaces with asymmetric distribution of asperity heights. *Transactions of the ASME-F-Journal of Tribology* 124, 2 (2002), 367–376.
- [157] YU, N., AND POLYCARPOU, A. A. Adhesive contact based on the Lennard–Jones potential: a correction to the value of the equilibrium distance as used in the potential. *Journal of Colloid and Interface Science* 278, 2 (2004), 428 – 435.
- [158] ZIENKIEWICZ, O. C., TAYLOR, R. L., AND TAYLOR, R. L. *The finite element method*, vol. 3. McGraw-hill London, 1977.